JETP Letters, Vol. 73, No. 10, 2001, pp. 505–509. From Pis'ma v Zhurnal Éksperimental'noĭ i Teoreticheskoĭ Fiziki, Vol. 73, No. 10, 2001, pp. 573–577.

Original English Text Copyright © 2001 by Bulgakov, Sadreev.

Spin Polarization in Quantum Dots by Radiation Field with Circular Polarization[1]

E. N. Bulgakov[1] and A. F. Sadreev[1,2]
[1] *Institute of Physics, Russian Academy of Sciences, Krasnoyarsk, 660036 Russia*
[2] *Department of Physics and Measurement Technology, Linköping University, S-581 83 Linköping, Sweden*
e-mail: almsa@ifm.liu.se
e-mail: almas@tnp.krasn.ru

Received March 11, 2001

For circular quantum dot (QD), taking into account the Razhba spin–orbit interaction (SOI), an exact energy spectrum is obtained. For a small SOI constant, the eigenfunctions of the QD are found. It is shown that the application of a radiation field with circular polarization removes the Kramers degeneracy of the QD eigenstates. Effective spin polarization of electrons transmitted through the QD owing to a radiation field with circular polarization is demonstrated. © *2001 MAIK "Nauka/Interperiodica".*

PACS numbers: 73.21.La; 71.70.Ej

The spin dependence of the electronic properties of artificial nanostructures is one of today's leading problems in the physics of electronic devices. Of interest are both the improvement of actual devices, like the GaAs polarized electron source (GaAs-PES) [1], and a search for new devices like spin transistors [2]. The effects of the spin degree of freedom on the electron transport properties of semiconductor heterostructures in the presence of inhomogeneous magnetic fields have been intensively studied experimentally [3, 4]. Experiments focusing on fundamental issues used inhomogeneous magnetic fields created either by vortices in superconductors [5, 6] or by ferromagnetic layers [7–9]. Theoretically, the spin-dependent resonant tunneling through magnetic barriers was calculated [10, 11] and the dependence of the spin polarization of transmitted electrons

$$P = \sum_{\sigma}\sigma T_{\sigma}/\sum_{\sigma}T_{\sigma} \tag{1}$$

on the magnetic configuration, applied bias, and incident electron energy was found [12].

The spin dependence of the electron transport across nonmagnetic semiconductor heterostructures at zero applied magnetic field arises due to the spin–orbit interaction (SOI). Basically, this phenomenon originates from the well-known phenomenon that the SOI has a polarizing effect on the particle scattering processes [13]; it was considered for different microdevices [14–17].

In this letter, we consider a possibility of resonant spin polarization of transmitted electrons by radiation field with circular polarization. It is well known in atomic spectroscopy that circularly polarized radiation field can transmit an electron from a multiplet state with a half-integer total angular momentum to a continuum with a definite spin polarization [18]. In this article, we consider similar phenomenon for the electron ballistic transport in quantum dots and in microelectronic devices with bound states.

At first stage, we consider a circular quantum dot with hard walls fabricated by metallic gates with applied negative electric potential. Because the standard technique of fabrication of microelectronic devices with depletion of 2DEG is based on the semiconductor GaAs/Al$_x$Ga$_{1-x}$As, the SOI in the Razhba form [19]

$$V_{SL} = \hbar K[\sigma_x p_y - \sigma_y p_x] \tag{2}$$

is important, where σ_x and σ_y are the Pauli spin matrices. The parameter of spin–orbit coupling K depends on the confining potential profile along the z direction, and, e.g., estimation for InAs structure with effective mass $m^* = 0.023m_0$ gives $\hbar^2K \sim 6 \times 10^{-3}$ eV nm [20] and $\hbar^2K \sim 10^{-3}$ eV nm for GaAs structure.

Using the natural energy scale of the QD $E_0 = \hbar^2/2m^*R^2$, where R is the QD radius, and the complex coordinates $z = x + iy$, we rewrite SOI (2) as

$$V_{SL} = 2\beta\begin{pmatrix} 0 & -\partial/\partial z \\ \partial/\partial z^* & 0 \end{pmatrix}, \tag{3}$$

where the space variables x, y, z are normalized to the QD radius R, and

$$\beta = 2m^*KR. \tag{4}$$

---

[1] This article was submitted by the authors in English.

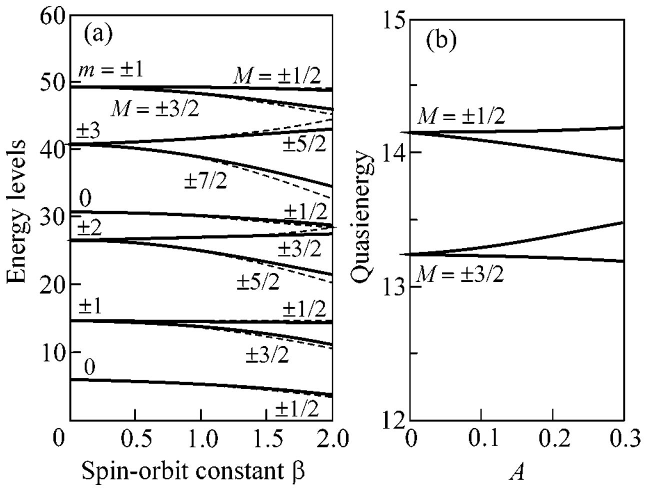

Fig. 1. (a) Energy levels of the QD with the SOI versus the spin–orbit constant β. The exact spectrum (17) is shown by dashed lines, while the approximated energy levels (18) are shown by solid lines. (b) The quasienergy levels of the QD effected by the radiation field with circular polarization versus the amplitude A of the radiation field for the spin–orbit coupling constant $\beta = 1$. In both cases, the QD radius equals unity.

The total Hamiltonian of the QD

$$H = -\nabla^2 + V(r) + V_{SL} \tag{5}$$

commutes with the z projection of the total angular momentum

$$\hat{J}_z = L_z + \frac{1}{2}\sigma_z \tag{6}$$

and with operator of time reversal

$$\hat{K} = -i\sigma_y C, \tag{7}$$

where C is the complex conjugation operator. The first integral of motion (6) allows one to represent eigenstates of Eq. (5) as

$$\psi_m = \begin{pmatrix} u(r)e^{im\phi} \\ v(r)e^{i(m+1)\phi} \end{pmatrix}, \tag{8}$$

because $\hat{J}_z\psi_m = (m + 1/2)\psi_m$.

Substituting Eq. (2) into equation $H\psi_m = \epsilon\psi_m$, one can obtain the following systems of radial equations:

$$\begin{gathered} r^2u'' + ru' + (\epsilon r^2 - m^2)u \\ + \beta r^2\left(\frac{d}{dr} + \frac{(m+1)}{r}\right)v = 0, \\ r^2v'' + rv' + (\epsilon r^2 - (m+1)^2)v \\ - \beta r^2\left(\frac{d}{dr} - \frac{m}{r}\right)u = 0. \end{gathered} \tag{9}$$

Taking

$$u = aJ_m(\mu r), \quad v = bJ_{m+1}(\mu r)$$

and using properties of Bessel functions, we have from Eq. (9)

$$\begin{gathered} \left[r^2\frac{d^2}{dr^2} + r\frac{d}{dr} + \left(\epsilon + \beta\mu\frac{b}{a}\right)r^2 - m^2\right]J_m(\mu r) = 0, \\ \left[r^2\frac{d^2}{dr^2} + r\frac{d}{dr} + \left(\epsilon + \beta\mu\frac{a}{b}\right)r^2 - (m+1)^2\right]J_{m+1}(\mu r) = 0. \end{gathered} \tag{10}$$

This equations are compatible only if

$$\mu = (\epsilon + b\beta\mu/a)^{1/2}, \tag{11}$$

$$\mu = (\epsilon + a\beta\mu/b)^{1/2}. \tag{12}$$

Correspondingly, we obtain $a = b$ with

$$\mu_{1\pm} = \beta/2 \pm \sqrt{\epsilon + (\beta/2)^2} \tag{13}$$

or $a = -b$ with

$$\mu_{2\pm} = -\beta/2 \pm \sqrt{\epsilon + (\beta/2)^2}. \tag{14}$$

As a result, we obtain two pairs of linearly independent solutions for Eq. (2). The first one is

$$\Phi^{\pm}_{1,m}(r,\phi) = \begin{pmatrix} J_m(\mu_{1\pm}r)e^{im\phi} \\ J_{m+q}(\mu_{1\pm}r)e^{i(m+1)\phi} \end{pmatrix}. \tag{15}$$

In a similar way, the next pair can be written.

We imply the Dirichlet boundary condition at $r = R$ for a linear combination of solutions (15)

$$C\Phi^{+}_{1,m}(R,\phi) + D\Phi^{-}_{1,m}(R,\phi) = 0. \tag{16}$$

It gives us the following exact equation for the energy spectrum of the QD with the SOI:

$$\begin{gathered} J_m(\mu_{1+}R)J_{m+1}(\mu_{1-}R) \\ -J_m(\mu_{1-}R)J_{m+1}(\mu_{1+}R) = 0. \end{gathered} \tag{17}$$

A few lowest energy levels of the QD versus the SOI constant β are shown in Fig. 1a. It is easy to see that the next pair of equations leads to the same equation as Eq. (17).

Equation (17) can be solved approximately for small constant of the SOI $\beta \le \sqrt{\epsilon}$. If we substitute Eq. (4) into this inequality, we obtain for the GaAs dot that the approximation of small β is valid for $R < 10^{-4}$ cm and low eigenenergies. Expanding Eq. (13) and the Bessel functions over small β, one can obtain after lengthy but elementary calculations the following expressions for approximate energy levels:

$$\epsilon_{mn,1} \approx \frac{x_{nm}^2}{R^2} + \frac{\beta^2}{4}\left[-1 + \frac{2x_{nm}J'_{m+1}(x_{nm})}{J_{m+1}(x_{nm})} - \frac{x_{nm}J''_m(x_{nm})}{J'_m(x_{nm})}\right],$$
$$\epsilon_{mn,2} \approx \frac{x_{nm}^2}{R^2} + \frac{\beta^2}{4}\left[-1 + \frac{2x_{nm}J'_{m-1}(x_{nm})}{J_{m-1}(x_{nm})} - \frac{x_{nm}J''_m(x_{nm})}{J'_m(x_{nm})}\right], \tag{18}$$

where x_{nm} is the nth zero of the Bessel function $J_m(x)$. The approximated spectrum of energy levels (18) is shown in Fig. 1a by dashed lines as a function of the SOI constant β. One can see that for the lowest eigenenergies the approximation is valid even for β exceeding unity.

It is easy to obtain that the SOI gives rise to splitting of degenerate energy levels of the QD with $M = m \pm 1/2$, expect the level with $m = 0$, with value of splitting as

$$\Delta_{mn} = \epsilon_{mn,2} - \epsilon_{mn,1} = \frac{\beta^2}{2}x_{nm}\left[\frac{J'_{m-1}(x_{nm})}{J_{m-1}(x_{nm})} - \frac{J'_{m+1}(x_{nm})}{J_{m+1}(x_{nm})}\right]. \tag{19}$$

Again using smallness of the SOI constant β, one can obtain from Eq. (16)

$$C = 1, \quad D = (-1)^m\left[1 + \beta R\frac{J'_{m+1}(x_{nm})}{J_{m+1}(x_{nm})}\right] \tag{20}$$

and from Eq. (15) the eigenstates

$$\Psi_{M=m+1/2} = \begin{pmatrix} J_m(x_{nm}r/R)e^{im\phi} \\ \frac{\beta}{2}e^{i(m+1)\phi}\left(rJ'_{m+1}(x_{nm}r/R) - RJ'_{m+1}(x_{nm})\frac{J_{m+1}(x_{nm}r/R)}{J_{m+1}(x_{nm})}\right) \end{pmatrix},$$
$$\Psi_{M=m-1/2} = \begin{pmatrix} \frac{\beta}{2}e^{i(m-1)\phi}\left(rJ'_{m-1}(x_{nm}r/R) - RJ'_{m-1}(x_{nm})\frac{J_{m-1}(x_{nm}r/R)}{J_{m-1}(x_{nm})}\right) \\ J_m(x_{nm}r/R)e^{im\phi} \end{pmatrix}. \tag{21}$$

The next pair of degenerate states with $M = -(m \pm 1/2)$ can easily be obtained by applying the Kramers operator (7) to states (21).

Next consider application of the radiation field with circular polarization

$$\mathbf{A}(t) = A(\sin\omega t, \cos\omega t, 0). \tag{22}$$

Note that below we are using the dimensionless radiation field amplitude $A \longrightarrow edA/c\hbar$ [21], where d is the width of leads, attachment of which will be considered below. Similar to the two-level system, an effect of this radiation field can be considered exactly by transformation to the rotating coordinate system by the unitary operator $\exp(i\omega t\hat{J}_z)$ to give rise to the following effective Hamiltonian:

$$\tilde{H} = H - \omega\hat{J}_z + 2iA\left(\frac{\partial}{\partial z} + \frac{\partial}{\partial z^*}\right), \tag{23}$$

where H is given by Eq. (5). Since

$$\frac{\partial}{\partial z}J_m(\mu r)e^{im\phi} = \frac{\mu}{2}J_{m-1}(\mu r)e^{i(m-1)\phi},$$
$$\frac{\partial}{\partial z^*}J_m(\mu r)e^{im\phi} = -\frac{\mu}{2}J_{m+1}(\mu r)e^{i(m+1)\phi}, \tag{24}$$

it obviously follows that the perturbation V can mix only states M and M' differing by $\Delta M = \pm 1$. One can see from Eq. (23) that the radiation field with circular polarization effects the QD like an external magnetic field, i.e., lifts the Kramers degeneracy. This phenomenon firstly was considered by Ritus for an atom affected by the radiation field with circular polarization [22]. Because of $[J_z, V] \neq 0$, we can not present exact eigenstates of the Hamiltonian (23). However, it is clear that the splitting of degenerated quasienergy states $\pm M$ can be found in the second order of perturbation theory to give rise to $\Delta E \sim A^2$. In fact, numerical calculation of eigenvalues of the effective Hamiltonian (23) clearly demonstrates the quadratic behavior of the quasienergy levels versus the amplitude of the radiation field, as is shown in Fig. 1b. Moreover the eigen states $\tilde{\psi}$ of the Hamiltonian (23) are spin polarized ones. In particular, we calculated numerically the spin polarization $\langle S_z \rangle = \langle \tilde{\psi}|\hat{S}_z|\tilde{\psi}\rangle$ for a few lowest states of the QD and found that $\langle S_z \rangle \approx \pm 0.9$ for the first doublet and very slightly depends on A.

Now let us attach leads with a width d to the QD and consider a transmission of electrons unpolarized by the spin through the QD. If coupling of leads with the QD is weak, we have resonant transmission of electrons.

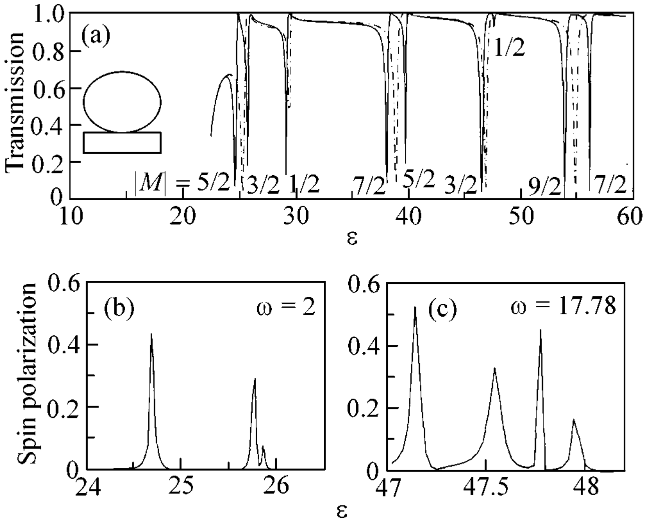

Fig. 2. (a) The transmission probability through the QD without (dashed line) and with the spin–orbit interaction ($\beta = 0.75$, solid line). The radiation field is turned off. (b) The spin polarization versus the energy of incident electrons for the case when the radiation field is not resonant ($\beta = 0.75$). (c) The spin polarization versus the energy of incident electrons for the case of the frequency resonant to transition between the state $|M| = 3/2$ and $|M| = 1/2$ ($\beta = 0.75$).

Because of strong spin polarization of the eigenstates of the QD effected by the radiation field, we can expect the resonant transmission with corresponding spin state while electrons with opposite spin state are reflecting. The aforesaid establishes the basic principle of the spin polarization via the resonant transmission through the QD effected by the radiation field with the circular polarization.

Here, we consider a case with tangential attachment as is shown in the inset of Fig. 2a. This case was considered in [23] and gives rise to resonant dips of the transmission probability. The computer calculations show that such kind of geometry is more effective for the spin polarization in comparison with the standard case of symmetrical attachment of leads to the QD. The only difference is that the electrons with the spin state coincided with that of the eigenstate of the QD are resonantly reflecting, while electrons with the opposite spin are transmitted, giving rise to the spin polarization of outgoing electron beam. Since tangential attachment of leads violates symmetry of the QD relative up to down, there should be spin polarization of transmitted electrons even without the radiation field [14–17]. However, this effect is very negligible in comparison with effect of the radiation field.

The process of electron transmission through the QD with application of a radiation field is complicated because of the appearance of new satellite channels in electron transmission specified by quasi energies [24] $E_n = E_F + n\hbar\omega$, $n = \pm1, \pm2, \ldots$, where

$$E_F = \hbar^2/2m^*d^2[k^2 + (\pi p/d)^2], \quad p = 1, 2, 3, \ldots . \tag{25}$$

A detailed computational procedure of the electron transmission with application of the radiation field is described in [21]. Here, we present only results of the computation shown in Fig. 2. Since Eq. (1) is obtained for the spin state of an incident electron up and down relative the z axis, it follows that $P = \langle S_z \rangle$. Therefore, it necessary to apply operator $\exp(i\hat{S}\theta)$ to the incident spin state in order to obtain the spin polarization along the x and y axes. As a result, one can obtain the total spin polarization described by a value $P_{\text{tot}} = (S_x^2 + S_y^2 + S_z^2)^{1/2}$ which is shown in Figs. 2b and 2c.

Figure 2b clearly demonstrates that for arbitrary frequency of the radiation field but *nonresonant* to transition between the eigenenergies E_M of the QD shown in Fig. 1a we have the resonant spin polarization for $E_F \approx E_M$. Moreover one can see that the energy dependence of the spin polarization is split in accordance with Fig. 1b with a value of the splitting of order A^2. Because of smallness of the radiation field amplitude, the first resonant peak of the spin polarization in Fig. 2b is not resolved.

However, if $\hbar\omega \approx E_{M'} - E_M$, a picture of the resonant spin polarization of the transmitted electrons changes crucially, as is shown in Fig. 2c. As a result, we have enhanced spin polarization for the case $E_F \approx E_M$, for the frequency of the radiation field is tuned to transition between the states $M = 1/2$, $m = 0$, $\epsilon_{1/2} = 29.33$ and $M = 3/2$, $m = 1$, $\epsilon_{3/2} = 47.12$ for the spin-orbit constant $\beta = 0.75$. Moreover, since the frequency of the radiation field is resonant to transition between the QD eigenstates, we observe strong splitting of peaks of the spin polarization because of the Raby splitting. The last is linear to the radiation field amplitude.

This work was supported partially by the RFBR, grant no. 01-02-16077, and the Royal Swedish Academy of Sciences.

REFERENCES

1. F. Meier and B. P. Zakharchenya, *Modern Problems in Condensed Matter Sciences* (Elsever, New York, 1984), Vol. 8.
2. D. J. Monsma, R. Vlutters, and J. C. Lodder, Science **281**, 407 (1998).
3. A. Majumdar, Phys. Rev. B **54**, 11911 (1996).
4. M. Sharma, Shan X. Wang, and J. H. Nickel, Phys. Rev. Lett. **82**, 616 (1999).
5. A. K. Geim, S. J. Bending, I. V. Grigorieva, and M. G. Blamire, Phys. Rev. B **49**, 5749 (1994).
6. A. Smith, R. Taboryski, L. T. Hansen, *et al.*, Phys. Rev. B **50**, 14726 (1994).

7. F. B. Mancoff, L. J. Zielinski, C. M. Marcus, *et al.*, Phys. Rev. B **53**, R7599 (1996).
8. T. Vancura, I. Ihn, S. Broderick, and K. Ensslin, Phys. Rev. B **62**, 5074 (2000).
9. R. Knobel, N. Samarth, S. A. Crooker, and D. D. Awschalom, Physica E (Amsterdam) **6**, 786 (2000).
10. Y. Guo, B.-L. Gu, and Yu Shang, Phys. Rev. B **55**, 9314 (1997).
11. V. N. Dobrovolsky, D. I. Sheka, and B. V. Chernyachuk, Surf. Sci. **397**, 333 (1998).
12. Y. Guo and B.-L. Gu, Phys. Rev. B **62**, 2635 (2000).
13. A. S. Davydov, in *Quantum Mechanics* (Pergamon, Oxford, 1965), Chap. XI.
14. A. Voskoboynikov, S. S. Liu, and C. P. Lee, Phys. Rev. B **58**, 15397 (1998); **59**, 12514 (1999).
15. E. A. de Andrada e Silva and G. C. La Rocca, Phys. Rev. B **59**, R15583 (1999).
16. E. N. Bulgakov, K. N. Pichugin, A. F. Sadreev, *et al.*, Phys. Rev. Lett. **83**, 376 (1999).
17. K. N. Pichugin, P. Streda, P. Seba, and A. F. Sadreev, Physica E (Amsterdam) **6**, 727 (2000).
18. N. E. Delone and M. E. Fedorov, Usp. Fiz. Nauk **127**, 651 (1979) [Sov. Phys. Usp. **22**, 252 (1979)].
19. Yu. A. Bychkov and E. I. Rashba, Pis’ma Zh. Éksp. Teor. Fiz. **39**, 66 (1984) [JETP Lett. **39**, 78 (1984)].
20. A. G. Aronov and Y. B. Lyanda-Geller, Phys. Rev. Lett. **70**, 343 (1993).
21. E. N. Bulgakov and A. F. Sadreev, Zh. Éksp. Teor. Fiz. **114**, 1954 (1998) [JETP **87**, 1058 (1998)].
22. V. N. Ritus, Zh. Éksp. Teor. Fiz. **51**, 1544 (1966) [Sov. Phys. JETP **24**, 1041 (1967)].
23. P. Exner, P. Seba, A. F. Sadreev, *et al.*, Phys. Rev. Lett. **80**, 1710 (1988).
24. M. Büttiker, Phys. Rev. Lett. **57**, 1761 (1986).

JETP Letters, Vol. 73, No. 10, 2001, pp. 510–513. Translated from Pis'ma v Zhurnal Éksperimental'noĭ i Teoreticheskoĭ Fiziki, Vol. 73, No. 10, 2001, pp. 578–582.
Original Russian Text Copyright © 2001 by Zakharchenko, Karavanskiĭ, Kotkovskiĭ, Kuznetsov, Chistyakov.

Resonant Radiationless Excitation Transfer to I_2 Molecules Sorbed in Pores of Porous Silicon

K. V. Zakharchenko[1], V. A. Karavanskiĭ[2], G. E. Kotkovskiĭ[1],
M. B. Kuznetsov[1], and A. A. Chistyakov[1],*
[1] *Moscow Institute of Engineering Physics, Kashirskoe sh. 31, Moscow, 115409 Russia*
** e-mail: chistaa@mail.ru*
[2] *Institute of General Physics, Russian Academy of Sciences, ul. Vavilova 38, Moscow, 117942 Russia*
Received February 9, 2001; in final form, March 21, 2001

Resonant radiationless electronic excitation transfer to I_2 molecules sorbed in pores of porous silicon was observed. The mass-spectrometry technique was used to show that iodine excitation through the resonant transfer results in the desorption of sorbed I_2 molecules with relatively high kinetic energies (1–3 eV). © *2001 MAIK "Nauka/Interperiodica".*

PACS numbers: 78.55.Hx; 78.55.Mb

Carrier radiationless recombination plays the key role in the electronic excitation relaxation processes in porous silicon [1]. Indeed, the radiative recombination [photoluminescence (PL)] quantum yield in porous silicon does not exceed 3% [2]. Porous silicon differs from bulk silicon primarily in that its specific surface area is very large. As a result, the role of the surface radiationless recombination processes sizably increases. Among these processes, the surface Si dangling-bond recombination [1] and the carrier capture to the surface states or by the traps in surface SiO layer [3] are the most efficient. The spatial electronic excitation transfer through tunneling between nanocrystals is also possible [4, 5]. At a high excitation level, three-particle Auger recombination processes also make a noticeable contribution to the excited-carrier recombination [6].

The influence of pore-sorbed molecules on the processes of radiative and radiationless recombination in porous silicon was investigated, e.g., in [3]. In particular, the influence of polarizability of physisorbed molecules on the luminescence of porous silicon was studied in detail within the framework of the excitonic model. The role of chemisorbed molecules in the processes of surface passivation accompanied by luminescence excitation in porous silicon was examined, and the role of Coulomb centers of adsorption complexes in the PL quenching was revealed. The adsorption states at the surface of porous silicon were also studied. However, no attention has been given so far to the important problem of relaxation through the resonant electronic excitation transfer between nanocrystals and sorbed molecules. In this case, an efficient indirect excitation of the sorbed molecules becomes possible through this relaxation mechanism. This opens up new possibilities of using porous silicon and other nanoporous materials in lasing, in stimulation of photoprocesses, and in the design of transducers, sensors, and biological tags.

The purpose of this work is to investigate the resonant electronic excitation transfer between the silicon nanocrystals and molecules sorbed in the pores of porous silicon.

Experimental method and samples. To solve the problem, a simple model iodine molecule was chosen as a sorbate, because, first, an analysis of the results of studies [6–10], where the luminescence properties of iodine adsorbed on various, including nanoporous, surfaces were studied, has shown that the spectrum of physisorbed iodine submonolayers is markedly broadened and shifted to the short-wavelength region, as compared to the spectrum of a molecular iodine crystal. For example, the absorption maximum of iodine molecules physisorbed on the surface of nanoporous quartz is positioned at 520 nm (i.e., its maximum virtually coincides with the absorption maximum of gaseous iodine) and the width at half maximum is ~150 nm. For this reason, one can expect that the absorption spectrum of the iodine sorbed on the surface of nanoporous silicon strongly overlaps with the luminescence spectrum of porous silicon in the range from ~400 to ~650 nm [6–10]. Second, I_2 does not absorb near λ = 266 nm (fourth harmonic of a neodymium laser) [7, 8]. Based on the results of studies [6–10], one can confidently assume that the spectrum of iodine submonolayers physisorbed on the nanoporous surface cannot be shifted and broadened to the extent that it occurs in the range of 266 nm, because in this case the term shift of molecular iodine would be equal to ~2 eV. At the same time, the absorption coefficient of nanoporous silicon is high at this wavelength. This allows the use of a radiation with λ = 266 nm for the selective excitation of porous silicon. And, finally, the intrinsic dipole moment of the iodine molecule is zero, which must minimize the influence of iodine sorbed in the pores of nanoporous silicon on the PL of the latter [3]. Moreover, the studies of electronic relaxation of the iodine molecules sorbed on various surfaces have shown that, owing to the enhanced role of radiationless recombination, the luminescence quantum yield of the sorbed iodine layers decreases and can be as low as 10^{-4}–10^{-5} [7, 8], which is three orders of magnitude lower than the quantum yield of porous silicon (~3%) [2]. Because of this, the luminescence of excited iodine can be ignored in the background of the luminescence of porous silicon.

The experimental methods included laser-induced luminescence [6, 10] and laser desorption mass spectrometry [7–9]. To excite porous silicon, the fourth harmonic (λ = 266 nm) of a YAG:Nd^{3+} laser was used in both methods. Pulse duration was 6 ns.

The luminescence method allowed the examination of both the luminescence spectra and the temporal characteristics of the samples. The number of laser pulses necessary for the recording and statistical processing of the PL kinetics was ~10^2.

In studying the laser-induced desorption, a sample was placed in the vacuum chamber of a mass spectrometer. The time-of-flight base L = 31 cm allowed one to record the time-of-flight spectra, i.e., the dependence of the mass-peak amplitude on the time of product direct flight to the ion source of the mass spectrometer [7–9]. The working vacuum was equal to 10^{-8} torr.

In our studies, porous silicon samples were prepared by anodizing commercially available silicon substrates KDB-10 in an HF(49%)–C_2H_5OH electrolyte (current density was in the range 10–150 mA/cm^2; etching duration ranged from 3 s to 10 min; for the details of preparing porous silicon, see, e.g., [6, 10]). Immediately after the preparation, the porous silicon samples were placed in the vacuum chamber of a mass spectrometer or in a chamber for iodine sorption. It should be noted that the sorption states of the samples were monitored by laser mass spectrometry [7], which showed that no air-sorbed compounds were present at the surface and in the pores of porous silicon.

In the mass-spectrometric experiments, iodine was sorbed for 3–5 min from a vacuum (pressure ~5×10^{-7} torr) with sample cooling to 77 K. The sorbed layer size was monitored by the luminescence of nanoporous silicon and by the mass-spectrometric method. The sorption of iodine molecules for the luminescence studies was carried out for 20–30 h under ambient conditions in a closed volume containing saturated iodine vapor. This allowed one to obtain submonolayer iodine coatings at the surface [7]. Special mass-spectrometric studies showed that the sorbed coatings in both cases were qualitatively and quantitatively identical [7] and that the surface molecular concentration was equal to ~0.1 monolayer.

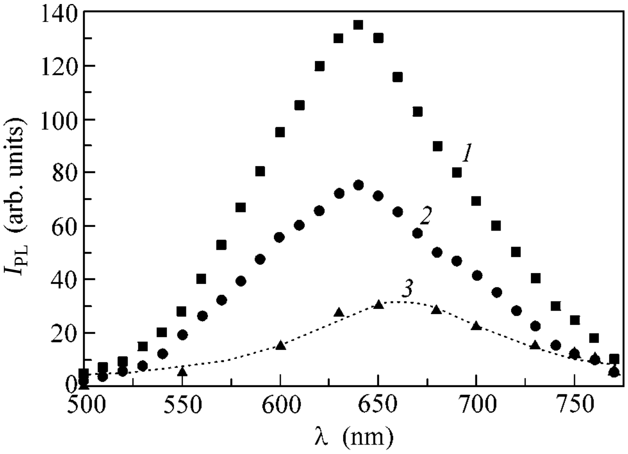

Fig. 1. PL spectra of porous silicon excited by the radiation at λ = 266 nm: (*1*) before the sorption of iodine and two days after the sorption; (*2*) 4 h after the sorption; and (*3*) 20 min after the sorption.

Experimental results and discussion. As a result of iodine sorption, the PL spectrum of porous silicon and the time dependence of its PL suffered substantial changes. The PL spectra of porous silicon before and after the sorption in the atmosphere of saturated I_2 vapor for 20 h are shown in Fig. 1. One can see that the spectrum is shifted to the long-wavelength region and its intensity decreased by several times. The time (t) decay curves for the PL intensity (I_{PL}) recorded at λ = 600 nm are shown in Fig. 2. For the laser output $q < 10^4$ W/cm^2, the experimental $I_{PL}(t)$ curves are well fitted by exponentials of the form $I_{PL}(t) = I_{PL}(0)\exp(-t/\tau)$. At $q > 10^4$ W/cm^2, the Auger recombination makes a considerable contribution to the recombination processes [11], and the experimental curves cease to be single-exponential. After the iodine sorption, the characteristic decay time τ (λ = 600 nm) decreased from 8.5 to ~1 μs. After the completion of sorption, the spectrum and the luminescence temporal characteristics were restored with time due to the natural desorption of iodine molecules. These characteristics were completely restored to the initial values within ~1–2 days. This suggested that molecular iodine was physisorbed at the surface and that the presence of I_2 in pores only caused reversible changes in the PL properties of porous silicon.

The fact that the PL-decay time for porous silicon decreases as a result of iodine sorption is clear evidence of the presence of resonant radiationless excitation transfer from nanocrystals to I_2 [12, 13], because the iodine absorption spectrum strongly overlaps with the luminescence spectrum of porous silicon in the range from ~400 to ~650 nm [6–10].

The luminescence decay is likely caused by a decrease in its quantum yield because of an increase in the radiationless recombination rate. It is also not improbable that the luminescence of porous silicon is reabsorbed by the iodine, which seems to be natural in

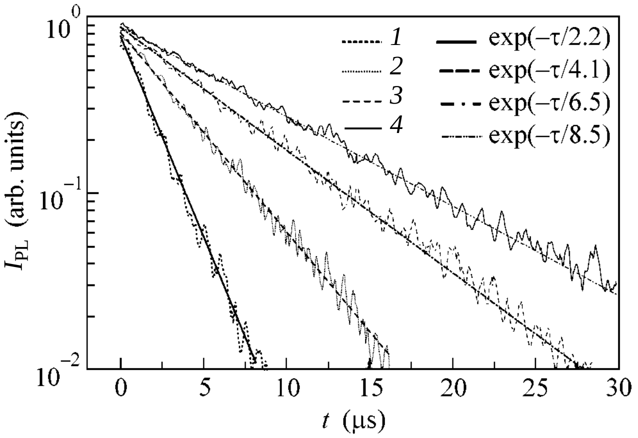

Fig. 2. Time dependences of the porous silicon PL intensity (excitation wavelength $\lambda = 266$ nm and $q = 6 \times 10^3$ W/cm^2) at the wavelength $\lambda = 600$ nm: (*1*) iodine-unsaturated sample and (*2–4*) 3, 7, and 90 min after the iodine sorption. Standard deviations of the fitting curves from the experiment: (*1*) 0.00119, (*2*) 0.00048, (*3*) 0.00021, and (*4*) 0.00025.

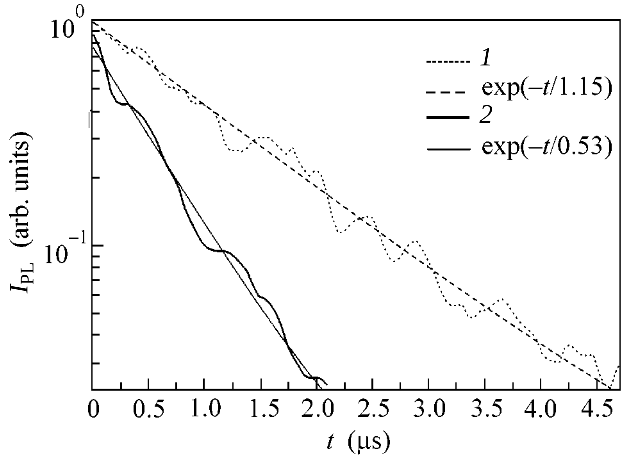

Fig. 3. Time dependences of the PL intensity of iodine-saturated porous silicon (excitation wavelength $\lambda = 266$ nm and $q = 6 \times 10^3$ W/cm^2): (*1*) sample irradiated with 6000 laser pulses and (*2*) nonirradiated sample. Record wavelength $\lambda_{PL} = 600$ nm. Standard deviations of the fitting curves from the experiment: (*1*) 0.0004 and (*2*) 0.0010.

the presence of the above-mentioned spectral overlap. However, the probability of excitation through the reabsorption is considerably (by two orders of magnitude) smaller than the probability of excitation through the transfer mechanism, because the PL quantum yield of porous silicon does not exceed 3% [3].

The resonant transfer must result in the electronic excitation of I_2 and lead to both iodine luminescence and iodine desorption from the surface of porous silicon [7–9]. However, since the luminescence quantum yield of I_2 is very low (10^{-4}–10^{-5} [7, 8]) in comparison with that of porous silicon, the I_2 luminescence is difficult to observe. Because of this, the excitation transfer to I_2 was directly proved by the observation of I_2 desorption from the surface of porous silicon as a result of the resonant excitation. The following experiment was carried out. Two parts of the same sample of porous silicon (whose PL-decay time was equal to 7 μs at $\lambda = 600$ nm in the absence of iodine) were exposed to the I_2 atmosphere for a day. After that, one of these parts was irradiated by the laser in a frequency-periodic mode ($q \sim 6 \times 10^3$ W/cm^2, $\lambda = 266$ nm, $\nu = 24$ Hz) and the number of laser pulses was ~6000. The PL kinetics was then recorded for both parts of the sample (Fig. 3). The corresponding PL-decay times were 1.2 and 0.5 μs; i.e., the decay time for the irradiated part of the sample was doubled compared to the untreated part. The experimental results showed that the action on the iodine-saturated sample of porous silicon by the laser pulses in an amount required for recording and statistical processing of luminescence kinetics did not change the luminescence decay time within the experimental error. An increase in the decay time upon prolonged laser radiation gives evidence for the iodine desorption. Consequently, the laser radiation resulted in a more efficient desorption of I_2 from the surface of porous silicon. Since I_2 does not directly absorb the radiation at $\lambda = 266$ nm, it is natural to assume that the desorption is a result of iodine excitation through the resonant transfer mechanism.

To directly observe and study in detail the desorption, mass-spectrometric studies were carried out. Molecular iodine was sorbed on the surface of a sample of porous silicon cooled to 77 K and placed in the vacuum chamber of a mass spectrometer. The coating was equivalent to the coating under usual sorption conditions (in the saturated iodine vapor). The treatment regime, namely, the laser output, was chosen in such a way that the photodesorption of hydrogen and silicon did not occur [6, 10], while, at the same time, the iodine desorption did occur. This regime was achieved at $q \leq 2 \times 10^4$ W/cm^2. Note that this laser output did not lead to a noticeable heating of the irradiated area. Moreover, it was shown in [6] that the contribution of short-wavelength luminescence of porous silicon markedly increased at $q = 2 \times 10^4$ W/cm^2, so that the blue region of the luminescence spectrum occurred near 400 nm (~3 eV). The time-of-flight desorption spectrum is shown in Fig. 4. The kinetic energy of the desorbed I_2 molecules proved to be anomalously high (1–3 eV). Therefore, the desorption of iodine molecules caused by the resonant electronic excitation transfer from the nanocrystals to the sorbed I_2 molecules was observed directly.

The desorption mechanism is similar to that described in [7, 8, 14], where the I_2 molecules sorbed on the surface of nanoporous quartz were excited by the resonant laser radiation at $\lambda = 532$, 575, and 640 nm. The kinetic energy of the desorbed particles was also anomalous high (compared to photon energy) and different at different excitation wavelengths [7, 8, 14]. In

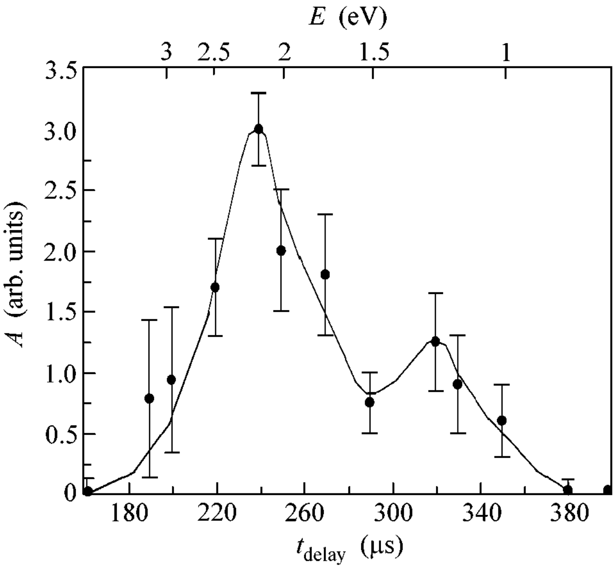

Fig. 4. Time-of-flight spectrum of I_2 desorption from the surface of nanoporous silicon upon the excitation of silicon by the radiation with $\lambda = 266$ nm and $q = 2 \times 10^4$ W/cm^2. The curves are guides to the eye and not the results of fitting procedure.

our case, the excitation by resonant radiationless transfer from porous silicon is possible in a wide range covering energies from ~3 to ~1.6 eV (and corresponding to the overlap between the PL of porous silicon and the absorption spectrum of I_2). In this case, the time-of-flight desorption spectrum becomes broader than the time-of-flight spectra for the resonant monochromatic excitation of I_2 [7, 8, 14]. A comparison of our results with the results of the indicated studies allows the conclusion to be drawn that the iodine desorption from the surface of porous silicon upon indirect excitation is adequately described by the model suggested in [7, 8, 14], where the iodine $\pi_g \longrightarrow \sigma_u$ excitation in a bounded nanopore volume is accompanied by the Franck–Condon transition of the molecule–surface complex to the state with higher potential energy followed by the release of an excess of this energy in the form of kinetic energy, i.e., by the desorption.

The estimates of the characteristic resonant-transfer distance (distance between the donor and acceptor) [12] gave a value of ~2 nm. This value is comparable with the characteristic size of the nanocrystals and nanopores.

In summary, this work reports the observation of the resonant radiationless excitation transfer between porous silicon nanocrystals and iodine molecules sorbed in pores. The mechanism of excitation transfer is satisfactorily described by the Förster model. A high-energy photodesorption of the iodine molecules from the surface of nanoporous silicon was experimentally observed (upon the excitation of only nanoporous silicon). The desorption was caused by the resonant radiationless transfer between the nanocrystals of porous silicon and the iodine molecules.

This work was supported by the Ministry of Science and Technologies of the Russian Federation (project nos. 08-02-48 and 97-10-73) and the program of Higher Education and Fundamental Science Integration (project no. A0103).

REFERENCES

1. A. G. Cullis, L. T. Canham, and P. D. J. Calcott, J. Appl. Phys. **82**, 909 (1997).
2. J. C. Vial, A. Bsiesy, F. Gaspard, *et al.*, Phys. Rev. B **45**, 14171 (1992).
3. P. K. Kashkarov, E. A. Konstantinova, and V. Yu. Timoshenko, Fiz. Tekh. Poluprovodn. (St. Petersburg) **30**, 1479 (1996) [Semiconductors **30**, 778 (1996)].
4. M. S. Bresler and I. N. Yassievich, Fiz. Tekh. Poluprovodn. (St. Petersburg) **27**, 871 (1993) [Semiconductors **27**, 475 (1993)].
5. E. F. Venger, É. B. Kopanovich, S. I. Kirillova, *et al.*, Fiz. Tekh. Poluprovodn. (St. Petersburg) **33**, 1330 (1999) [Semiconductors **33**, 1202 (1999)].
6. Yu. A. Bykovskiĭ, V. A. Karavanskiĭ, G. E. Kotkovskiĭ, *et al.*, Zh. Éksp. Teor. Fiz. **117**, 136 (2000) [JETP **90**, 121 (2000)].
7. G. E. Kotkovskiĭ, *Laser Desorption and Photodissociation of Iodine Molecules at the Surfaces of Bulk and Nanoporous Quartz*, Candidate's Dissertation in Mathematical Physics (MIFI, Moscow, 1999).
8. Yu. A. Bykovskii, A. A. Chistyakov, M. B. Kuznetsov, *et al.*, Laser Phys. **7**, 1063 (1997).
9. Yu. A. Bykovskiĭ, G. E. Kotkovskiĭ, M. B. Kuznetsov, *et al.*, Zh. Éksp. Teor. Fiz. **114**, 114 (1998) [JETP **87**, 64 (1998)].
10. Yu. A. Bykovskii, A. A. Chistyakov, V. A. Karavanskii, *et al.*, Laser Phys. **9**, 687 (1999).
11. I. Mihalcescu, J. S. Vial, A. Bsiesy, *et al.*, Phys. Rev. B **51**, 17605 (1995).
12. N. J. Turro, *Molecular Photochemistry* (Benjamin, New York, 1965; Mir, Moscow, 1967).
13. V. M. Agranovich and M. D. Galanin, *Electronic Excitation Energy Transfer in Condensed Matter* (Nauka, Moscow, 1978; North-Holland, Amsterdam, 1982).
14. Yu. A. Bykovskiĭ, G. E. Kotkovskiĭ, A. A. Chistyakov, *et al.*, Pis'ma Zh. Éksp. Teor. Fiz. **62**, 389 (1995) [JETP Lett. **62**, 400 (1995)].

Translated by V. Sakun

JETP Letters, Vol. 73, No. 10, 2001, pp. 514–518. Translated from Pis'ma v Zhurnal Éksperimental'noĭ i Teoreticheskoĭ Fiziki, Vol. 73, No. 10, 2001, pp. 583–587.

Original Russian Text Copyright © 2001 by Boldarev, Gasilov, Blasco, Stenz, Dorchies, Salin, Faenov, Pikuz, Magunov, Skobelev.

Modeling Cluster Jets as Targets for High-Power Ultrashort Laser Pulses

A. S. Boldarev[1,*], V. A. Gasilov[1], F. Blasco[2], C. Stenz[2], F. Dorchies[2], F. Salin[2], A. Ya. Faenov[3], T. A. Pikuz[3], A. I. Magunov[3], and I. Yu. Skobelev[3]

[1] *Institute of Mathematical Modeling, Russian Academy of Sciences, Moscow, 125047 Russia*

[2] *CELIA, Universite Bordeaux 1, 33405 Talence, France*

[3] *All-Russia Research Institute of Physical and Radio Engineering Measurements, State Scientific Center, Mendeleevo, Moscow region, 141570 Russia*

** e-mail: boldar@imamod.ru*

Received March 30, 2001

A hydrodynamic model is formulated that describes the formation of clusters in atomic gas jets expanding into vacuum, which are used as laser plasma targets. Detailed model calculations performed for an argon gas jet describe spatial distributions of the density of gas and cluster phases formed in the Laval nozzle at room temperature in a broad range of entrance gas pressures. The cluster density distribution is significantly inhomogeneous. The cluster distribution features revealed by the model calculations were qualitatively confirmed by the X-ray spectroscopic measurements of the spatial distribution of emission from the plasma created in the jet targets by high-power ultrashort laser pulses. © *2001 MAIK "Nauka/Interperiodica".*

PACS numbers: 52.50.Jm; 52.25.Os; 32.30.Rj

INTRODUCTION

The interaction of high-power ultrashort laser pulses with gas jet targets is now extensively studied by theoretical and experimental methods. Of special interest is the case of gas jets containing clusters (liquid droplets or solid particles) with the corresponding density of substance. In this case, the efficiency of laser action upon the target jet at a critical electron density significantly increases and the resulting plasma is heated to much greater temperatures. A high density of the laser-generated plasma in cluster-containing jets implies a greater role of collision processes, which leads to an increase in the degree of plasma ionization. For example, the interaction of ultrashort laser pulses at an energy flux density of 10^{17}–10^{18} W/cm^2 with cluster targets was accompanied by X-ray emission in the Ar XVII and Kr XXVII multicharged ion lines [1–3]. The formation of these ions by tunneling ionization in the laser field takes place at higher intensity levels as follows, for example, from the formula of Ammosov *et al.* [4].

Description of the interaction of ultrashort laser pulses with cluster jets presents a more complicated problem as compared to the case of solid or gas targets, since, in particular, even the initial state of the target (which can be spatially inhomogeneous) is unknown. By now, a number of papers are available reporting on the study of the interaction of laser radiation with clusters (see, e.g., [5–12]). In these experiments, the main attention was paid to the evolution of clusters under the action of laser radiation pulses, while the cluster formation process was outside the scope of investigation. The parameters of clusters in the jets were evaluated with the aid of a multiparametric empirical formula [13–15] or based on analysis of the Rayleigh scattering of a probing laser radiation in the jet [6].

These methods allow only the average cluster size and density to be estimated, thus characterizing the gas jet studied as a whole. However, knowledge of the spatial distribution and time variation of the cluster target parameters can be necessary both for a correct numerical modeling of the process of laser-induced heating and for some important applications requiring plasma homogeneity in one direction over a sufficiently large region (e.g., for the creation of X-ray lasers). Such data can be obtained by modeling the hydrodynamic processes with an allowance for the phase transitions taking place in the gas jet. To our knowledge, no attempts at such a description of the jet targets have been reported so far.

Below, we demonstrate that data on the spatial distributions of all parameters necessary for the correct calculation of the cluster jet heating by short laser pulses can be provided by detailed investigations of the gasdynamic processes in a nozzle forming a two-phase jet. The results of our calculations conducted for a nozzle of the Laval type operating at various initial gas pressures showed that a gas–cluster jet virtually homogeneous in the cross section can be formed under certain conditions. In other cases, the spatial distribution of clusters is inhomogeneous and even nonmonotonic. The results of model calculations were confirmed by the data of space-resolved X-ray spectroscopic measurements showing the spatial distribution of linear and continuous emission from plasma created in a cluster target by high-power femtosecond laser pulses.

MODEL CALCULATIONS

The process of cluster formation was described within the framework of a model based on the so-called method of moments, which was developed and used predominantly for the investigation of wet steam in nozzles and turbine shafts. Phase transitions in nozzle flows were extensively studied (see, e.g., [16, 17] and references therein). Although special attention was paid to steam, since steam flows are most widely employed in power plants, the model approaches developed are applicable to the flow of any gas provided the corresponding physical conditions are taken into account. For the experimental conditions of interest, we will consider the gas efflux at the initial room temperature, which implies that the flow contains no ions. Thus, a condensed phase (we will consider only a liquid phase) nucleates as result of fluctuations in a supercooled gas (i.e., by spontaneous condensation).

A detailed presentation of the theory of spontaneous condensation can be found, for example, in [18]. Owing to the surface effects, a small liquid droplet may occur in equilibrium or evaporate even in a supercooled gas. The surface tension creates an additional potential barrier for a molecule attaching to the droplet. Therefore, there is a certain critical droplet radius r_{cr} depending on the particular gas parameters. The critical droplet occurs in equilibrium with the supercooled vapor, whereas smaller particles evaporate and disappear, and only droplets possessing radii greater than r_{cr} can grow. Our calculations employed a relationship

$$r_{cr} = \frac{2\sigma}{\rho_l RT\ln(P/P_s)}, \qquad (1)$$

where σ is the coefficient of surface tension; ρ_l is the liquid density; $R = R_0/\mu$ is the gas constant; μ is the molar mass; T and P are the gas temperature and pressure, respectively; and $P_s(T)$ is the temperature-dependent saturation pressure.

Thus, for the appearance of a condensation nucleus capable of growing continuously, a fluctuation must take place leading to the formation of a droplet with the radius $r > r_{cr}$. The frequency of such fluctuations, which can be determined based on the theory of heterophase fluctuations (see, e.g., [19]), is given by the expression

$$I = \frac{1}{\rho_l}\sqrt{\frac{2\sigma\mu}{\pi N_A}}\left(\frac{P}{kT}\right)^2\exp\left(-\frac{4\pi\sigma r_{cr}^2}{3kT}\right), \qquad (2)$$

where N_A is Avogadro's number and k is the Boltzmann constant. The I value can be interpreted as the number of condensation nuclei formed in a unit volume per unit time.

The growth rate of the supercritical condensation nuclei was calculated by the formula

$$\dot{r} = \frac{P}{\rho_l\sqrt{2\pi RT}}\left(1-\sqrt{\frac{T}{T_l}}\right), \qquad (3)$$

where T_l is the liquid droplet temperature. Formula (3) is valid provided that the growth proceeds in a free molecular regime and is not limited by the rate of heat removal. The droplet temperature T_l is assumed to be independent of its radius and equal to the saturation temperature $T_s(P)$. Strictly speaking, this last assumption (necessary for the further model development) is not valid and contradicts the above definition of the critical droplet radius (according to which the critical droplet is characterized by $\dot{r} = 0$).

We have employed a two-phase flow model based on the following assumptions: (i) the velocity of droplets is equal to that of the gas jet; (ii) the droplet temperature is equal to the saturation temperature; (iii) the effects of droplet splitting and merging, viscosity, thermal conductivity, and turbulence are negligibly small; and (iv) the possibility of droplet freezing and the formation of crystal nuclei can be ignored. The model can be described by the following system of differential equations:

$$\partial\rho/\partial t + \mathrm{div}(\rho\mathbf{v}) = 0, \qquad (4)$$

$$\partial\rho\mathbf{v}/\partial t + \mathrm{div}(\rho\mathbf{v}\otimes\mathbf{v}) = -\mathrm{grad}P, \qquad (5)$$

$$\frac{\partial}{\partial t}\left(\rho e + \rho\frac{\mathbf{v}^2}{2}\right) + \mathrm{div}\left(\rho\mathbf{v}\left(e + \frac{\mathbf{v}^2}{2}\right)\right) = -\mathrm{div}P\mathbf{v}, \qquad (6)$$

$$\partial\rho\Omega_0/\partial t + \mathrm{div}(\rho\mathbf{v}\Omega_0) = I, \qquad (7)$$

$$\begin{gathered}\partial\rho\Omega_n/\partial t + \mathrm{div}(\rho\mathbf{v}\Omega_n) = Ir_{cr}^n + n\dot{r}\rho\Omega_{n-1},\\ (n = 1, 2),\end{gathered} \qquad (8)$$

$$\frac{\partial\rho\beta}{\partial t} + \mathrm{div}(\rho\mathbf{v}\beta) = -\frac{4}{3}\pi\rho_l I r_{cr}^3 - 4\pi\rho\rho_l\dot{r}\Omega_2, \qquad (9)$$

$$P = P(\rho, e, \beta) = \frac{e + (1-\beta)L_s}{\gamma/(\beta(\gamma-1)) - 1}, \quad T = \frac{P}{\beta Z\rho R}. \qquad (10)$$

Here, ρ is the overall density of the two-phase medium; $\mathbf{v}$ is the gas jet velocity; e is the specific internal energy; β is the relative "dryness" (i.e., the mass fraction of the gas phase in the mixture); and Ω_i ($i = 0, 1, 2$) are the moments of the droplet radius distribution function. In the equations of state (10), L_s is the specific heat of vaporization, $\gamma = c_P/c_V$ is the adiabatic exponent, and Z is the compressibility coefficient.

The system of equations (4)–(9), closed by the relationships (1)–(3) and (10) and supplemented with the corresponding boundary and initial conditions, was numerically solved in the region including the internal volume of the nozzle and part of the open space behind the nozzle exit (in a two-dimensional variant). The noz-

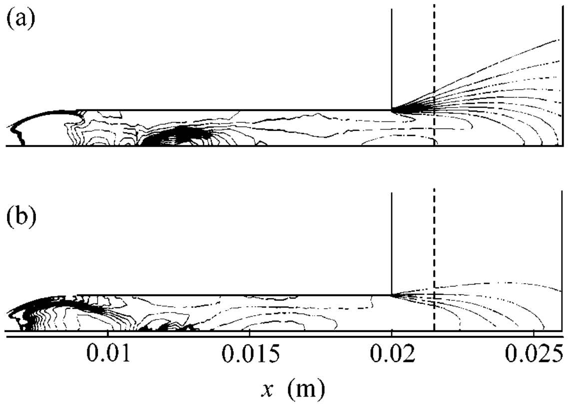

Fig. 1. A schematic diagram of the Laval nozzle showing isolines of (a) the cluster density $n_{\rm drop}$ and (b) the mass fraction $\langle N\rangle n_{\rm drop}$ of the cluster phase in the argon jet.

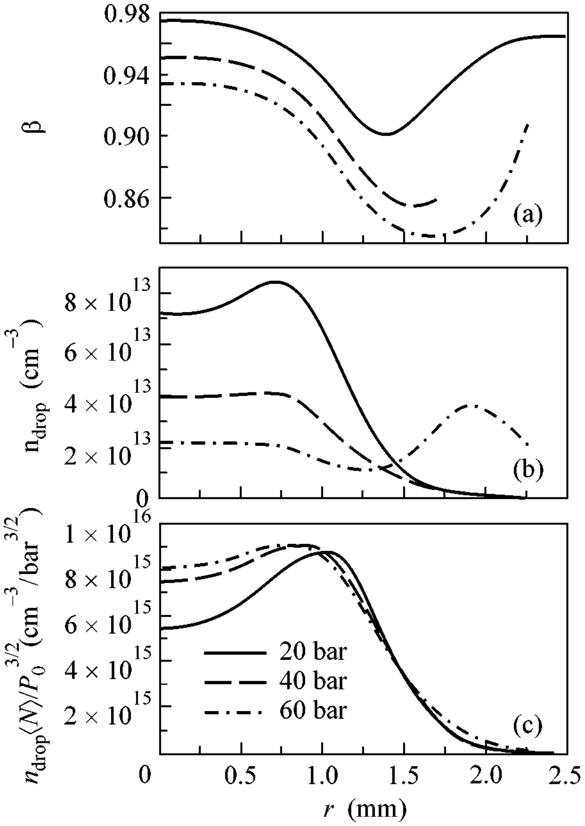

Fig. 2. Diagrams illustrating distributions of the jet parameters in a cross section situated 1.5 mm away from the Laval nozzle exit (calculated for the argon pressure P_0 = 20, 40, and 60 bar at the nozzle entrance): (a) "dryness" β; (b) cluster density $n_{\rm drop}$; (c) average density of clustered atoms $n_{\rm drop}\langle N\rangle$.

zle shape corresponded to that used in the experiments described below. The calculations were performed for argon with the initial parameters P_0 = 20–60 bar, T_0 = 293 K.

The results of the model calculations presented here refer to a time instant when the flow has virtually attained a stationary state. Figure 1 shows isolines of the cluster (liquid droplet) density $n_{\rm drop}$ and the cluster mass fraction in the mixture $\langle N\rangle n_{\rm drop}$ ($\langle N\rangle$ being the average number of atoms in clusters) calculated for the gas pressure at the nozzle entrance P_0 = 40 bar. The isolines are drawn for the cluster densities ranging from 0 to 6×10^{13} cm^{-3} at a step of 0.429×10^{13} cm^{-3} and for the $\langle N\rangle n_{\rm drop}$ value 0 to 3×10^{18} cm^{-3} at a step of 0.214×10^{18} cm^{-3}. As is seen, the two-dimensional distribution of clusters is significantly inhomogeneous inside the nozzle and at the exit. The dashed line in Fig. 1 indicates the cross section situated at a distance of 1.5 mm away from the nozzle exit. The results of calculations showed that a considerable proportion of the liquid (cluster) phase is formed at the periphery of the flow, whereas the region at the jet axis features a "drier" gas phase (which is especially pronounced at the nozzle exit). This conclusion is illustrated in Fig. 2 showing the gas and cluster phase distributions in the jet cross section 1.5 mm away from the nozzle exit. As is seen, the maximum cluster density takes place at a distance of approximately 1 mm from the axis (Fig. 2b). As the gas pressure at the nozzle entrance grows, the distribution of the mass fraction of the cluster phase becomes more homogeneous (Fig. 2c).

The main result of our calculations consists in that the region at the jet axis features a "dry" gas with smaller cluster density. This theoretical result qualitatively agrees with the experimental data presented below, according to which two regions of extensive absorption of the laser radiation are observed on both sides from the jet axis.

EXPERIMENTAL RESULTS

The experiments were performed on a laser setup at Bordeaux University (France) described in detail elsewhere [2]. The pulsed laser radiation parameters were as follows: energy, 15 mJ; wavelength, 790 nm; pulse duration, 35 fs; repetition frequency, 1 kHz. The laser beam was focused with the aid of an off-axis parabolic mirror into a spot with a diameter of 6 μm, which corresponds to a maximum beam power density at the target of 4×10^{17} W/cm^2. The targets were pulsed gas jets (Kr and CO_2) expanding from a nozzle of the Laval type into a vacuum chamber at a velocity corresponding to the Mach number 2.5. The internal diameter of the cylindrical region was 2.5 mm. The maximum pressure in the valve was 20–40 atm. The laser pulse was focused within the gas jet in the cross section 1.5 mm away from the nozzle exit.

The spatial characteristics of the X-ray emission from the laser-generated plasma were studied with the aid of focusing spherical crystal (R = 150 mm) position-sensitive spectrographs [20]. The emission from plasma was measured at a right angle with respect to

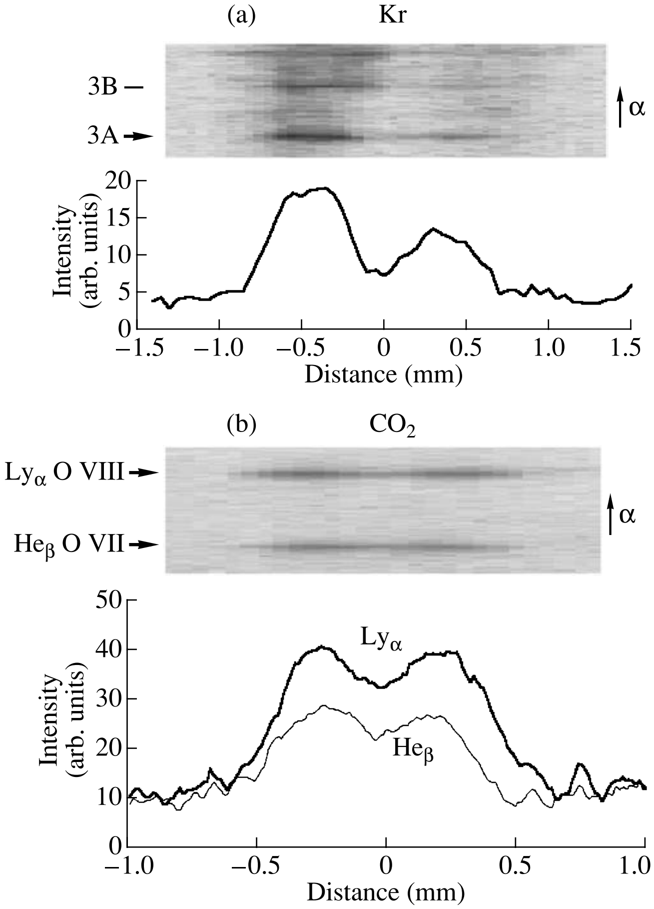

Fig. 3. Space-resolved X-ray spectrograms of laser-generated plasma in gas jet targets and spatial profiles of the time-averaged emission intensity in various spectral lines measured in the direction across the (a) Kr and (b) CO_2 jet at a distance of 1.5 mm from the Laval nozzle exit.

the laser beam direction, which allowed the emission intensity distribution to be studied at a high spatial resolution (up to 20 μm) along this and perpendicular directions. The X-ray spectrum was registered on a RAR-2492 film through a filter comprising two 1-μm-thick polypropylene films coated on both sides with an 0.1-μm-thick aluminum layer.

Figure 3a shows a space-resolved spectrogram of the X-ray emission from a Kr jet target plasma recorded in the laser beam direction (the image is compressed in the direction of spectral resolution). As is seen, the intensity profile of emission in the 3 A resonance line of a Ne-like ion Kr XXVII in the jet cross section exhibits two clear maxima spaced ≈1 mm from one another. The intensity of the second maximum amounts to approximately half that of the first one. Approximately the same spatial distribution was observed in the continuous (bremsstrahlung and photorecombination) emission from plasma measured with the aid of the spectrograph, as well as in the lines of H- and He-like ions O VIII and VII (Fig. 3b) registered in a CO_2 jet target featuring crystalline clusters. These results indicate that the nonmonotonic emission intensity distribution reflects the distribution of "robust" plasma parameters (temperature and density) rather than some features of the level population kinetics in individual ions.

The pattern of plasma luminosity qualitatively agrees with the initial distribution of clusters in the gas jet according to the gas-dynamic calculations (cf. Figs. 2 and 3). It should be emphasized that no complete quantitative coincidence in the spatial distribution of these values has to be expected since the luminosity depends not only on the density of plasma but on the temperature as well. The spatial distribution of temperature in the plasma is determined both by the spatial variation of the laser beam power density and by the efficiency of energy absorption in the target. The efficiency of laser-induced plasma heating is related predominantly to the cluster density and size, whereas the spatial distribution of the laser beam power density is determined by the focusing system and by the nonlinear refraction of laser radiation in the ionized gas. We may expect that the laser power density is maximal in the focusing plane (i.e., on the jet axis) and decreases on both sides. This should be manifested by a shift of the emission intensity toward the jet axis, which is actually observed in experiment (Fig. 3). A distance between the emission intensity peaks is ≈1 mm for Kr jet and ≈0.5 mm for CO_2 jet, whereas the cluster density maxima (calculated for argon) are spaced by ≈2 mm. In analogous experiments with a different Laval nozzle, the presence of two emission intensity maxima was observed for CO_2 and Ar jet targets [1].

CONCLUSION

Thus, we have proposed a two-dimensional hydrodynamic model describing the spatial distribution of parameters in clustered gas jet targets for laser plasma experiments. The gas jet features effective van der Waals cluster formation by the mechanism of spontaneous condensation of liquid droplets. The results of model calculations conducted for a nozzle of the Laval type revealed inhomogeneous cluster density distribution across the jet. The inhomogeneity, the degree of which increases with decreasing gas pressure at the nozzle entrance, is manifested by the appearance of a cluster density maximum displaced from the jet axis. This effect is confirmed by inhomogeneity observed in the spatial distribution of the X-ray emission from plasma generated by femtosecond laser pulses in both atomic and molecular gas jet targets.

The above results present an attempt at providing a detailed description of the parameters of two-phase gas jets. The proposed approach may indicate an optimum way to develop the gas jet sources. In particular, the results of the model calculation show that targets possessing more homogeneous cluster distributions in the jet cross section are obtained by increasing the entrance gas pressure. This circumstance is important, for example, from the standpoint of developing X-ray lasers.

This study was partly supported by the Fond Europeen de Developement Economique Regional, Conseil Regional d'Aquitaine, and (in the part of mathematical modeling) by the Russian Foundation for Basic Research (project no. 00-01-00562).

REFERENCES

1. S. Dobosz, M. Schmidt, M. Perdrix, *et al.*, Pis'ma Zh. Éksp. Teor. Fiz. **68**, 454 (1998) [JETP Lett. **68**, 485 (1998)].
2. C. Stenz, V. Bagnoud, F. Blasco, *et al.*, Kvantovaya Élektron. (Moscow) **30**, 721 (2000).
3. T. Auguste, P. D'Oliveira, S. Hulin, *et al.*, Pis'ma Zh. Éksp. Teor. Fiz. **72**, 54 (2000) [JETP Lett. **72**, 38 (2000)].
4. M. V. Ammosov, N. B. Delone, and V. P. Kraĭnov, Zh. Éksp. Teor. Fiz. **91**, 2008 (1986) [Sov. Phys. JETP **64**, 1191 (1986)].
5. A. McPherson, T. S. Luk, B. D. Thompson, *et al.*, Phys. Rev. Lett. **72**, 1810 (1994).
6. T. Ditmire, T. Donnelly, A. M. Rubenchik, *et al.*, Phys. Rev. A **53**, 3379 (1996).
7. T. Ditmire, J. W. G. Tisch, E. Springate, *et al.*, Phys. Rev. Lett. **78**, 2732 (1997).
8. M. Lezius, S. Dobosz, D. Normand, and M. Schmidt, Phys. Rev. Lett. **80**, 261 (1998).
9. T. Ditmire, E. T. Gumbrell, R. A. Smith, *et al.*, Phys. Rev. Lett. **80**, 720 (1998).
10. J. Larsson and A. Sjogren, Rev. Sci. Instrum. **70**, 2253 (1999).
11. T. Ditmire, J. Zweiback, V. P. Yanovsky, *et al.*, Nature **398**, 489 (1999).
12. V. P. Kraĭnov and M. B. Smirnov, Usp. Fiz. Nauk **170**, 969 (2000).
13. O. F. Hagena and W. Obert, J. Chem. Phys. **56**, 1793 (1972).
14. O. F. Hagena, Surf. Sci. **106**, 101 (1981).
15. O. F. Hagena, Rev. Sci. Instrum. **63**, 2374 (1992).
16. M. E. Deĭch and G. A. Filippov, *Gas Dynamics of Two-Phase Media* (Énergoizdat, Moscow, 1981).
17. G. A. Saltanov, *Nonequilibrium and Nonstationary Processes in Gas Dynamics* (Nauka, Moscow, 1979).
18. L. E. Sternin, *Foundations of Gas Dynamics of Two-Phase Jets in Nozzles* (Mashinostroenie, Moscow, 1974).
19. Ya. I. Frenkel', *Kinetic Theory of Liquids* (Nauka, Leningrad, 1975).
20. I. Yu. Skobelev, A. Ya. Faenov, B. A. Bryunetkin, *et al.*, Zh. Éksp. Teor. Fiz. **108**, 1263 (1995) [JETP **81**, 692 (1995)].

Translated by P. Pozdeev

JETP Letters, Vol. 73, No. 10, 2001, pp. 519–523. Translated from Pis'ma v Zhurnal Éksperimental'noĭ i Teoreticheskoĭ Fiziki, Vol. 73, No. 10, 2001, pp. 588–592.
Original Russian Text Copyright © 2001 by Afanas'ev, Chuev, Hesse.

Shift of Relaxation-Stimulated Resonances in Mössbauer Absortion Spectra in a Static Magnetic Field

A. M. Afanas'ev[1], M. A. Chuev[1,*], and J. Hesse[2]

[1] *Institute of Physics and Technology, Russian Academy of Sciences, Nakhimovskiĭ pr. 36, Moscow, 117218 Russia*

** e-mail: chuev@ftian.oivta.ru*

[2] *Institute of Metal and Nuclear Physics, Technical University of Braunschweig, D-38106 Braunschweig, Germany*

Received April 6, 2001

New features are obtained for previously predicted relaxation-stimulated resonances in Mössbauer spectra of nanomagnets exposed to an external rf field: the resonances should undergo low-frequency shift upon applying a weak static magnetic field. Analytic expressions for the resonance frequencies as functions of the static field are obtained within a simplified relaxation model. This effect extends the possibilities for experimental observation of the predicted effects, because tuning to the resonance may be accomplished not only by changing frequency of the rf field but also by varying the amplitude of the alternating field and the strength of the static field. *© 2001 MAIK "Nauka/Interperiodica".*

PACS numbers: 75.75.+a; 76.80.+y; 75.60.-d

The external rf field acting on nanomagnets changes magnetic moments of both individual particles and the sample as a whole. In most cases, the temporal trajectories of magnetic moments of individual particles are determinate in an external rf field; i.e., the magnitude and direction of the magnetic moment are strictly determined at every instant. In Mössbauer spectra, this is manifested as a collapse of the magnetic hyperfine structure (hfs) and appearance of rf sidebands [1]. As was shown in [2–4], the trajectories of magnetic moments undergo qualitative change at certain rf amplitudes; the trajectories cease to be determinate and become stochastic; i.e., the magnitude and direction of the magnetic moment of a particle are no longer strictly specified and are described by certain probability characteristics. For this case, qualitatively new types of resonance phenomena were predicted in the Mössbauer absorption spectra at rf frequencies related to the frequencies of magnetic hfs components via the parametric resonance conditions [3, 4]. This effect is expected to manifest itself as a sharp resonance narrowing of certain hfs components whose frequencies coincide with the frequency of the rf field:

$$\omega_{\mathrm{rf}} = \frac{|M\omega_e - m\omega_g|}{n}, \qquad (1)$$

where n is an integer; m and M are the nuclear spin projections onto the direction of hyperfine field; and ω_g and ω_e are the NMR frequencies in the ground and excited states, respectively.

The nontrivial character of this phenomenon is caused by the fact that the nuclear excited state lies energetically higher than the ground state by a value exceeding the splitting of nuclear levels by more than ten orders of magnitude and, nevertheless, the external rf field coherently couples the nuclear ground- and excited-state hyperfine sublevels only through the relaxation processes. The resonances of type (1) were named relaxation-stimulated resonances, because they can be observed only in the case where the relaxation processes play the important role in the magnetization reversal of the sample.

The relaxation effects manifest themselves mainly at those trajectory time domains where the field reaches its maximum, i.e., twice during the period of the rf field. A strong effect of the rf field with an amplitude of about 10 Oe on the shape of Mössbauer spectra was clearly observed in experiments (see [5] and references therein). If, in addition to the rf field, a weak static magnetic field is applied whose strength is comparable to the amplitude of the rf field, then the situation can be realized where the stochastic behavior of the temporal trajectories of the magnetic moment will occur once in the period rather than twice. In this case, it is natural to expect that new features will appear in the previously predicted resonance effects. The above-mentioned situations with the stochastic behavior of single nanoparticles are of interest not only for Mössbauer spectroscopy but also for the theory of magnetism on the whole. In this situation, unusual phenomena should appear in the magnetic properties of a system; namely, hysteresis loops should acquire a nonstandard shape of the type depicted in Fig. 1. Such an anomalous behavior of the magnetic system of Stoner–Wohlfarth particles was

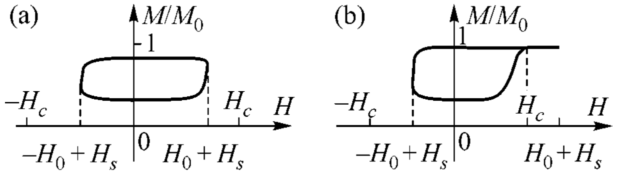

Fig. 1. Magnetization curves for the Stoner–Wohlfarth particles in an rf field with amplitude H_0 and a static magnetic field H_s: (a) $H_s + H_0 \le H_c$ and (b) $H_s + H_0 > H_c$.

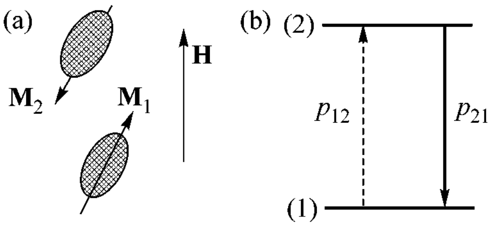

Fig. 2. (a) Equilibrium states of a particle with different orientations of magnetic moment **M** in an external magnetic field **H** and (b) scheme of relaxational transitions between these states in the OWLR model.

pointed out in [2]. Recently, interest in this problem has quickened because analogous features were predicted for classical ferromagnets with domain structure (see [6] and references therein).

Let us consider a sample as an ensemble of single-domain ferromagnetic particles with magnetization $\mathbf{M}_0$ and axially symmetric magnetic anisotropy whose energy E_{an} is assumed to be high enough (the so-called Stoner–Wohlfarth model [7]). In the absence of an external magnetic field, each particle may be only in two states of the same energy and magnetic moments oppositely directed along the easy magnetic axis (Fig. 2a). In the external magnetic field, the local energy minima undergo a shift and, after the field exceeds a certain critical value H_c, only one absolute energy minimum is retained, so that the direction of the magnetic moment becomes strictly determined.

The states in the local minima are coupled via the relaxation processes that are described by the transition rates p_{12} and p_{21} (Fig. 2b) strongly affecting the shape of the Mössbauer spectrum [2]. In the case that the deviations of the magnetic moment from the easy magnetic axis can be neglected, while the hyperfine field $\mathbf{H}_{hf}$ at the nucleus can only reverse its direction in the course of relaxation, the cross section for gamma-ray quantum absorption under the action of the rf field is given by

$$\sigma(\omega) = \frac{\sigma_a\Gamma_0^2}{4}\sum_{\alpha}|C_\alpha|^2\varphi_\alpha(\omega), \qquad (2)$$

where $\alpha = (M, m)$; the coefficients C_α specify the intensities of the corresponding hyperfine transitions; σ_a is the effective thickness of absorber; Γ_0 is the width of the excited nuclear level; and

$$\varphi_\alpha(\omega) = \frac{1}{\Gamma_0 T_{\rm rf}} \times \int_0^{T_{\rm rf}} dt \int_t^{\infty} dt' \langle W(t)|e^{i\tilde{\omega}(t'-t)}\hat{G}_\alpha(t, t')|1\rangle + \text{c.c.} \qquad (3)$$

Here, $\tilde{\omega} = \omega + i\Gamma_0/2$; $T_{\rm rf} = 2\pi/\omega_{\rm rf}$; and

$$\hat{G}_\alpha(t, t') = \hat{T}\exp\left[\int_t^{t'} dt''(-i\hat{\omega}_\alpha - \hat{P}(t''))\right], \qquad (4)$$

$$i\hat{\omega}_\alpha + \hat{P}(t) = \begin{pmatrix} i\omega_\alpha + p_{12}(t) & -p_{12}(t) \\ -p_{21}(t) & -i\omega_\alpha + p_{21}(t) \end{pmatrix}, \qquad (5)$$

where $\hat{T}$ is the chronological ordering operator; $\omega_\alpha = M\omega_e - m\omega_g$; $\omega_{e,g} = g_{e,g}\mu_N H_{hf}$; μ_N is the nuclear magneton; $g_{e,g}$ are the nuclear g factors in the excited and ground state, respectively; and the state-population vector $\langle W(t)|$ is fully determined by the relaxation process:

$$\frac{d\langle W(t)|}{dt} = -\langle W(t)|\hat{P}(t). \qquad (6)$$

The detailed derivation of Eqs. (2)–(6) can be found in [2].

Equation (3) can be recast in the following simple form:

$$\varphi_\alpha(\omega) = \frac{1}{\Gamma_0 T_{\rm rf}}\left(\langle A_\alpha(\omega)|\frac{1}{\hat{1} - e^{i\tilde{\omega}T_{\rm rf}}\hat{G}_\alpha(0, T_{\rm rf})} \times |B_\alpha(\omega)\rangle + \Delta\varphi_\alpha(\omega)\right) + \text{c.c.}, \qquad (7)$$

where

$$\langle A_\alpha(\omega)| = \int_0^{T_{\rm rf}} dt\langle W(t)|e^{i\tilde{\omega}(T_{\rm rf}-t)}\hat{G}_\alpha(t, T_{\rm rf}), \qquad (8)$$

$$|B_\alpha(\omega)\rangle = \int_0^{T_{\rm rf}} dt e^{i\tilde{\omega}t}\hat{G}_\alpha(0, t)|1\rangle, \qquad (9)$$

$$\Delta\varphi_\alpha(\omega) = \int_0^{T_{\rm rf}} dt \int_t^{T_{\rm rf}} dt'\langle W(t)|e^{i\tilde{\omega}(t'-t)}\hat{G}_\alpha(t, t')|1\rangle. \qquad (10)$$

To calculate the absorption spectrum, it is necessary to specify the dynamics of the magnetic system, i.e., the time dependence of the relaxation parameters $p_{12}(t)$ and

$p_{21}(t)$. In the Stoner–Wohlfarth model, these functions are determined from the equation

$$p_{12}(t) = p_0 \exp(-U_{12}(t)/k_B T), \tag{11}$$

where $U_{12}(t)$ is the energy barrier to the transition from state 1 to state 2, p_0 is a constant, and T is temperature. An analogous formula can be written for $p_{21}(t)$. The barrier heights are calculated using the scheme suggested in [7]. They are fully determined by the external magnetic field acting on the particle. In our case,

$$H(t) = H_0 \cos(\omega_{\mathrm{rf}} t) + H_s, \tag{12}$$

where H_s is the static magnetic field and H_0 is the amplitude of the rf field. Making use of Eqs. (2)–(12), one can calculate the absorption spectra [2], but these formulas are unsuitable for the qualitative analysis.

Let us use a simplified relaxation model which ignores the relaxational transitions from the lower energy level to the excited level and assumes that the relaxation process is localized at time instants corresponding to the maxima of the rf field (under condition that $H_s + H_0 \le H_c$). The corresponding points are indicated in Fig. 1 by dashed lines. This so-called one-way localized relaxation (OWLR) model drastically simplifies the general formula presented in [4]. First, this model allows one to pass from the differential relaxation parameters $p_{21}(t)$ and $p_{12}(t)$ to the integral characteristics

$$r_k = \exp\left[-2 \int\limits_{t_k - t_\varepsilon}^{t_k} p_k(t) dt\right], \tag{13}$$

which determine the probability for a particle to not change its state upon passing through the points of rf field maxima [$t_k = kT_{\mathrm{rf}}/2$ ($k = 1$ and 2) and t_ε is a time interval small compared to the period of the rf field]. Equation (13) is substantiated in [4].

In the OWLR model, one has for the time intervals between the localization points of the relaxation process

$$\hat{G}_\alpha(t, t') = \hat{g}_\alpha(t' - t) = \begin{pmatrix} e^{-i\omega_\alpha(t'-t)} & 0 \\ 0 & e^{i\omega_\alpha(t'-t)} \end{pmatrix}, \tag{14}$$
$$(t, t') \in (t_k, t_{k+1}).$$

When calculating the function $\hat{G}_\alpha(t, t')$, one can ignore the hyperfine interactions in the vicinity of points t_k and retain only the relaxation operator $\hat{P}$. Moreover, the operators $\hat{P}(t)$ for different instants of time commute with each other in the one-way relaxation model. This fact allows the functions $\hat{G}_\alpha(t, t')$ to be expressed through the integral characteristics r_k of the relaxation process:

$$\begin{aligned} \hat{G}_\alpha(t_1 - t_\varepsilon, t_1 + t_\varepsilon) &= \hat{R}_1 = \begin{pmatrix} r_1 & q_1 \\ 0 & 1 \end{pmatrix}, \\ \hat{G}_\alpha(t_2 - t_\varepsilon, t_2 + t_\varepsilon) &= \hat{R}_2 = \begin{pmatrix} 1 & 0 \\ q_2 & r_2 \end{pmatrix}, \end{aligned} \tag{15}$$

where $q_k = 1 - r_k$. For arbitrary times t and t', the function $\hat{G}_\alpha(t, t')$ can easily be found with allowance made for the properties of the $\hat{T}$-product. Using Eqs. (14) and (15), one can express all operators in Eqs. (7)–(10) in an explicit form and calculate the absorption spectrum for arbitrary frequencies of the rf field and arbitrary values of parameters r_1 and r_2 (Fig. 3).

In the case that $H_s + H_0 \le H_c$ and the stochastic magnetization reversal occurs at both ends of the hysteresis loop, one has

$$\hat{G}(0, T_{\mathrm{rf}}) = \begin{pmatrix} r_1 e^{-i\omega_\alpha T_{\mathrm{rf}}} + q_1 q_2 & q_1 r_2 \\ q_2 e^{i\omega_\alpha T_{\mathrm{rf}}} & r_2 e^{i\omega_\alpha T_{\mathrm{rf}}} \end{pmatrix}. \tag{16}$$

For high rf frequencies, $\omega_{\mathrm{rf}} \gg \Gamma_0$, the term $\Delta\phi_\alpha$ in Eq. (7) is a small and smoothly varying correction [3], so that it can be ignored when determining the shapes of individual lines in the spectrum. (Note that at lower frequencies it becomes the leading term.) Taking this into account, one can readily find from Eq. (7) that the line widths and positions obey the equation

$$\det(\hat{1} - e^{i\tilde{\omega} T_{\mathrm{rf}}} \hat{G}_\alpha(0, T_{\mathrm{rf}})) = 0, \tag{17}$$

which is reduced in our case to the equation

$$\begin{aligned} &(1 - r_1 e^{i(\tilde{\omega} - \omega_\alpha)T_{\mathrm{rf}}})(1 - r_2 e^{i(\tilde{\omega} + \omega_\alpha)T_{\mathrm{rf}}}) \\ &\qquad - q_1 q_2 e^{i\tilde{\omega} T_{\mathrm{rf}}} = 0. \end{aligned} \tag{18}$$

Note that in the absence of the static field ($H_s = 0$) $r_1 = r_2$. This case was analyzed in detail in [4], where it was found that at frequencies satisfying condition (1) the lines with natural width Γ_0 should be observed in the absorption spectrum, whereas, on the detuning from the resonance frequencies, the lines strongly broaden. One can easily verify that at exact resonance (1) the narrow lines with natural width are also retained in the static magnetic field, i.e., at $r_1 > r_2$. Indeed, if condition (1) is satisfied, dispersion Eq. (18) is reduced to an equation of the form

$$(1 - e^{i\tilde{\omega} T_{\mathrm{rf}}})(1 - r_1 r_2 e^{i\tilde{\omega} T_{\mathrm{rf}}}) = 0. \tag{19}$$

In this case, the absorption spectrum must contain components with natural width Γ_0 at frequencies ω_α, and it is easy to show that these lines are strong (and become

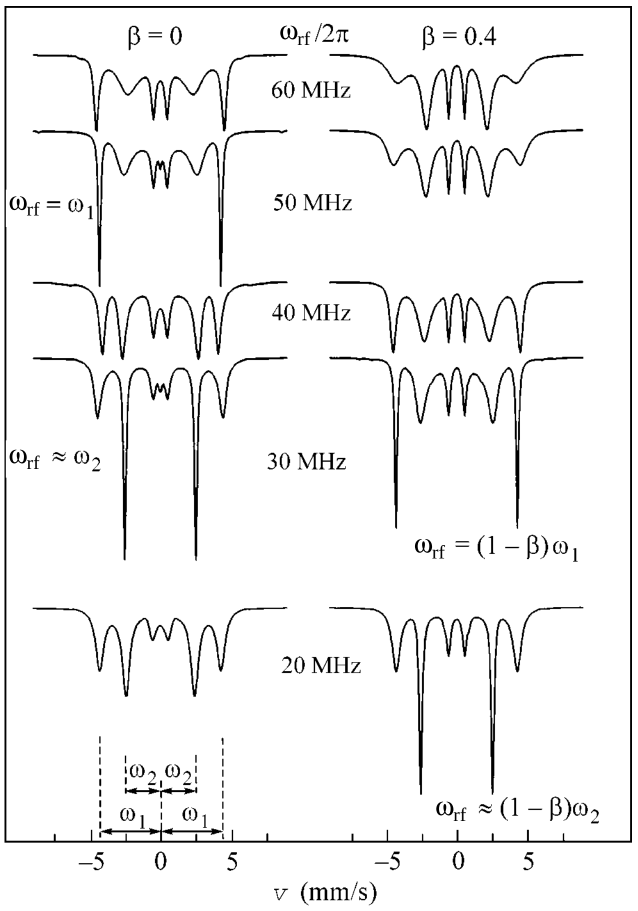

Fig. 3. Mössbauer spectra in the static and rf magnetic fields in the OWLR model with $q = 0.3$ for different frequencies of the rf field in the cases $H_s + H_0 = H_c$ ($\beta = 0$) and $H_s + H_0 > H_c$ ($\beta = 0.4$). The spectra are calculated for the ^{57}Fe nuclei, $\omega_{3/2,\,1/2} = \omega_1 = 2\pi \times 50$ MHz, and the nonpolarized gamma-ray beam perpendicular to the direction of the external rf field.

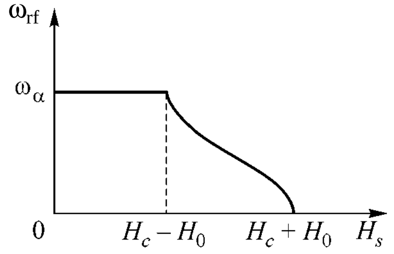

Fig. 4. The frequency of relaxation-stimulated resonances as a function of external magnetic field.

even stronger with an increase in H_s) and noticeably broaden upon detuning from the resonance. The characteristic features of these resonances are demonstrated in the left spectra in Fig. 3, where the resonance behavior of the outermost and inner lines at frequencies, respectively, $\omega_{\rm rf} = \omega_{3/2,\,1/2} = \omega_1$ and $\omega_{\rm rf} = \omega_{1/2,\,1/2} = \omega_2$ is clearly seen.

Evidently, these results are valid only if $H_s + H_0 \le H_c$. In this case, the static field does not shift the frequencies of the previously predicted relaxation-stimulated resonances. In stronger fields, $H_s + H_0 \ge H_c$ (but $H_0 - H_s < H_c$), the situation changes dramatically, as is seen from the hysteresis loop shapes (Fig. 1b). In this case, the stochastic magnetization reversal occurs only once during the period of the rf field, and one must set $r_2 = 0$, $q_2 = 1$, and $t_2 = T_{\rm rf}\{1 - \arccos[(H_c - H_s)/H_0]/2\pi\}$ in Eq. (15). As a result, Eq. (17) takes the form

$$1 - r_1 e^{i(\tilde{\omega} - \omega_\alpha)T_{\rm rf}} - q_1 e^{i(\tilde{\omega} - \beta\omega_\alpha)T_{\rm rf}} = 0, \qquad (20)$$

where the asymmetry parameter

$$\beta = \arccos[(H_c - H_s)/H_0]/\pi. \qquad (21)$$

One can readily verify that for the rf frequencies

$$\omega_{\rm rf} = \frac{(1 - \beta)\omega_\alpha}{n} \qquad (22)$$

dispersion Eq. (20) takes the form

$$1 - e^{i(\tilde{\omega} - \omega_\alpha)T_{\rm rf}} = 0. \qquad (23)$$

The latter equation also determines the lines with natural width Γ_0 at ω_α, and these lines additionally broaden upon detuning the rf frequency from resonance value (22). Therefore, the relaxation-stimulated resonance will also occur in this case, but the resonance frequency will shift to lower frequencies with increasing static field H_s, in compliance with condition (22). In the right column of Fig. 3, the typical absorption spectra are shown for the rf frequencies in the vicinity of resonance (22) for the outermost and inner lines at frequencies $\omega_{\rm rf} = (1 - \beta)\omega_1$ and $(1 - \beta)\omega_2$, respectively. One can see from this figure that the relaxation-stimulated resonance clearly manifests itself in this case as well. The dependence of resonance frequency on the static magnetic field is shown in Fig. 4 for the two above-mentioned cases of stochastic magnetization reversal.

If the parameters H_0 and H_s are chosen in such a way that the conditions $H_s + H_0 > H_c$ and $H_0 - H_s > H_c$ are met and the magnetization reversal process becomes strictly determinate ($r_1 = 0$, $q_1 = 1$ and $r_2 = 0$, $q_2 = 1$), dispersion Eq. (20) transforms to the equation

$$1 - e^{i(\tilde{\omega} - \beta\omega_\alpha)T_{\rm rf}} = 0. \qquad (24)$$

In this limiting case, the positions of main lines in the spectrum are determined by the hyperfine field βH_{hf} averaged over the rf period, and the sidebands appear at distances $\pm n\omega_{\rm rf}$ from the main lines, in accordance with the results of study [8], where this limit was explored both theoretically and experimentally. Clearly, no resonance phenomena for the rf field are observed in this case.

Thus, the above analysis indicates that the effect of a static magnetic field on the previously predicted relaxation-stimulated resonances has a nonlinear threshold character (Fig. 4). It has no close analogies among the other resonance phenomena. Note that the obtained results can be of great practical importance. The tuning to the resonance can be performed not only by changing the frequency of the rf field but also by applying an external static field, which can substantially simplify the relevant experiments.

REFERENCES

1. L. Pfeiffer, J. Appl. Phys. **42**, 1725 (1971).
2. A. M. Afanas'ev, M. A. Chuev, and J. Hesse, Phys. Rev. B **56**, 5489 (1997).
3. A. M. Afanas'ev, M. A. Chuev, and J. Hesse, Zh. Éksp. Teor. Fiz. **116**, 1001 (1999) [JETP **89**, 533 (1999)].
4. A. M. Afanas'ev, M. A. Chuev, and J. Hesse, J. Phys.: Condens. Matter **12**, 623 (2000).
5. J. Hesse, T. Graf, M. Kopcewicz, *et al.*, Hyperfine Interact. **113**, 499 (1998).
6. I. F. Lyuksyutov, T. Nattermann, and V. Pokrovsky, Phys. Rev. B **59**, 4260 (1999).
7. E. C. Stoner and E. P. Wohlfarth, Philos. Trans. R. Soc. London, Ser. A **240**, 599 (1948).
8. A. Ya. Dzyublik, V. Yu. Spivak, R. A. Manapov, and F. G. Vagizov, Pis'ma Zh. Éksp. Teor. Fiz. **67**, 57 (1998) [JETP Lett. **67**, 61 (1998)].

Translated by V. Sakun

JETP Letters, Vol. 73, No. 10, 2001, pp. 524–528. Translated from Pis'ma v Zhurnal Éksperimental'noĭ i Teoreticheskoĭ Fiziki, Vol. 73, No. 10, 2001, pp. 593–597.
Original Russian Text Copyright © 2001 by Lozovik, Ovchinnikov.

Cooling of Excitons by Coherent Phonon Radiation

Yu. E. Lozovik* and I. V. Ovchinnikov
Institute of Spectroscopy, Russian Academy of Sciences, Troitsk, Moscow region, 142190 Russia
** e-mail:lozovik@isan.troitsk.ru*

Received April 9, 2001

The effect of exciton cooling by coherent phonon radiation, which is based on coherent confinement of exciton populations, is considered. Peculiarities of coherent confinement of excitons in an exciton system are analyzed, in which the umklapp processes as well as recombination and relaxation play an important role. The limitations imposed on the parameters of the system for which the effect can be realized are determined taking into account these peculiarities. © *2001 MAIK “Nauka/Interperiodica”.*

PACS numbers: 71.35.Lk; 63.20.Ls

The detection of coherent states of excitons formed in a quasi-equilibrium exciton system at low temperatures is an interesting problem in solid-state physics. The coherent state of excitons must possess a number of interesting properties such as superfluidity and supertransport of energy (i.e., superthermal conductivity) associated with it; in the case of indirect excitons in coupled quantum wells, these are nondissipative electric currents in each of the wells, Josephson effects, and so on [1–3]. In the case of pulsed pumping, the equilibrium state of excitons is formed only if the exciton relaxation time is much shorter than their lifetime determined by the electron–hole recombination.[1] In the case of continuous laser pumping creating excitons, it is difficult to attain equilibrium at a low temperature (even for a fairly low temperature of the lattice).

It follows hence that the problem of cooling the exciton subsystem is very important for the observation of interesting low-temperature phases of excitons. In this connection, we consider here the effect of exciton cooling by a coherent phonon beam. We will describe the idea of the method below, confining ourselves to a few general remarks at this stage.

A coherent phonon beam can be excited in a solid, for example, with the help of an ultrashort laser pulse [4] through parametric swinging of the lattice or induced scattering.[2] Another possible method of excitation of a coherent phonon beam is similar to a certain extent to the creation of a conventional laser beam (“phonon laser”) by using, for example, a three-level system in semiconducting structures, in which phonons play the role of photons. A number of possible schemes of a phonon laser have been proposed at present [6, 7], and certain advances have been made in this direction, which raises hopes of obtaining a reliable source of coherent phonon radiation in the nearest future.

The idea behind exciton cooling by a coherent phonon beam lies in the excitation of an exciton–exciton transition by coherent phonons with an entropy close to zero, followed by spontaneous emission of phonons carrying away the entropy of the system and, hence, cooling the exciton system. In this work, we consider an interesting special case of such a cooling associated with the effect of coherent confinement of populations in the exciton subsystem. This problem differs from the cooling of atoms by laser radiation not only in the replacement of photons by phonons, but also in the nontrivial role of the Brillouin zone in the given process as well as in taking into account relaxation in the exciton system.

Let us now consider the problem under investigation. We assume that there are two exciton levels (which will be denoted by U and L) coupled through a standing phonon wave. Such exciton levels may be, for example, the levels adjoining various size-quantization levels in quantum wells or quantum wires or indirect and direct excitons in coupled quantum wells. Thus, we consider the effect of cooling in the exciton–exciton transition. Nevertheless, this effect may also take place during a transition between a single exciton level and the continuous spectrum of scattering for electrons and holes. In this case, our description requires a certain generalization which, however, does not lead to any qualitatively new results.

The effective potential of interaction between excitons and a coherent phonon waves can be written in the form

$$\hat{V}(\mathbf{x}) = \frac{1}{2}g((e^{i\mathbf{kx}} + e^{-i\mathbf{kx}})e^{-i\omega_k t} + \text{c.c.}), \qquad (1)$$

---

[1] For this reason, indirect excitons in coupled quantum wells whose recombination is associated with tunneling of carriers through the barrier between the quantum wells are favorable for observation. For this reason, their lifetime is considerably longer than for direct excitons [2, 3].

[2] The high-intensity pulse of coherent acoustic phonons required for cooling (see below) can be obtained in a layered system or superlattice [5].

where g is a constant proportional to the matrix element on the phonon induced exciton–exciton transition and to the square root of the phonon radiation intensity. The potential of interaction between excitons and phonons is a scalar [8]; since the chosen exciton levels are coupled through a phonon transition, there exist other limitations imposed on them (e.g., they must have the same parity, spin, etc.).

We assume that the wave vector $\mathbf{k}$ of phonon radiation is parallel to a symmetry axis of the Brillouin zone ($\mathbf{e}_x$) and that the length of this vector is exactly one-fourth of the width of the Brillouin zone in this direction. Such phonon radiation can be created using, for example, a phonon transition in an nondirect-gap semiconductor [7]. In the case under investigation, induced transition may transfer an exciton with a fixed momentum in the Brillouin zone only to three more states in the Brillouin zone. In this case, umklapp effects for excitons are significant (see figure). Thus, potential (1) splits the complete set of exciton states on levels U and L into tetrads of states coupled through induced transitions. Such tetrads of states are parametrized by the wave vector belonging to half the Brillouin zone. Thus, p_x is defined only in mod($2k$). Within each tetrad, we define the states and the energies corresponding to them as follows:

$$\begin{gathered}|\mathbf{p}\rangle_1 = |\mathbf{p}\rangle_L, \quad |\mathbf{p}\rangle_2 = |\mathbf{p}-2\mathbf{k}\rangle_L,\\ |\mathbf{p}\rangle_3 = e^{-i\omega_k t}|\mathbf{p}-\mathbf{k}\rangle_U, \quad |\mathbf{p}\rangle_4 = \mathbf{e}^{-\mathbf{i}\omega_k \mathbf{t}}|\mathbf{p}-3\mathbf{k}\rangle_U,\\ \omega_1(\mathbf{p}) = \omega(\mathbf{p})_L, \quad \omega_2(\mathbf{p}) = \omega(\mathbf{p}-2\mathbf{k})_L,\\ \omega_3(\mathbf{p}) = \omega(\mathbf{p}-\mathbf{k})_U - \omega_k, \quad \omega_4(\mathbf{p}) = \omega(\mathbf{p}+3\mathbf{k})_U - \omega_k.\end{gathered} \tag{2}$$

Here, we have also introduced the temporal factors in order to eliminate the time dependence from the Hamiltonian. In such a basis, the one-particle Hamiltonian for excitons taking into account expression (1) can be written in the form

$$\hat{\mathcal{H}}(\mathbf{p}) = \begin{Vmatrix} \omega_1(\mathbf{p}) & 0 & \frac{1}{2}g & \frac{1}{2}g \\ 0 & \omega_2(\mathbf{p}) & \frac{1}{2}g & \frac{1}{2}g \\ \frac{1}{2}g & \frac{1}{2}g & \omega_3(\mathrm{p}) & 0 \\ \frac{1}{2}g & \frac{1}{2}g & 0 & \omega_4(\mathbf{p}) \end{Vmatrix}. \tag{3}$$

For simplicity, we assume that the coupling constant g is independent of the momentum of interacting exciton levels. The equation of the system dynamics has the form of the Liouville equation for the density matrix:

$$i\frac{\partial}{\partial t}\hat{\rho}(\mathbf{p}) = [\hat{\mathcal{H}}(\mathbf{p}), \hat{\rho}(\mathbf{p})].$$

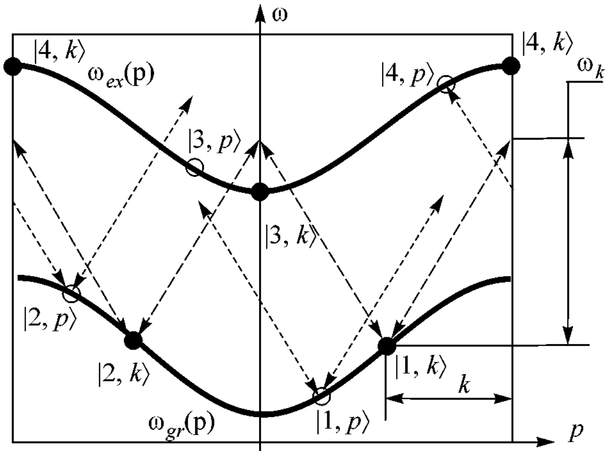

Cross section of the Brillouin zone by a plane parallel to the wave vector k of phonon radiation. Phonon radiation splits the exciton bands into tetrads of states coupled through induced transitions, which is associated with umklapp effects. For example, the absorption of a phonon with the wave vector $-k$ transforms the state $|2, p\rangle$ into the state $|4, p\rangle$. The tetrad of states characterized by the wave vector k possesses a superposition state which does not interact with the phonon fields.

This equation preserves the trace of $\hat{\rho}(\mathbf{p})$; i.e., the initial distribution over tetrads coupled through induced transitions remains unchanged. This is due to the fact that Hamiltonian (3) takes into account induced transitions only. In transitions from the upper to the lower exciton level accompanied by spontaneous emission of a phonon, photons are emitted isotropically, in contrast to induced transitions. Consequently, an exciton from the upper level goes over to lower states with different momenta $\mathbf{p}$ as a result of a spontaneous transition.

The form of Hamiltonian (3) implies that for momenta $\mathbf{p}$ for which the energies of the lower coupled levels coincide, the states $1/\sqrt{2}\,(|\mathbf{p}\rangle_1 - |\mathbf{p}_0\rangle_2)$ are stationary and are not involved in the interaction with the phonon field. An exciton falling once into one of such states will not be excited to upper levels and will remain in this state forever. However, the excitons from other lower states will again be excited to the upper level and then decay to a lower level until they occupy (as a result of a spontaneous transition) one of such preferred states. Thus, after some time, all excitons will be in states which do not interact with the phonon field, and the evolution of the system terminates. This is the essence of the effect under investigation. It should also be noted that such states always exist since $\omega_1(\mathbf{p}) = \omega_2(\mathbf{p} \pm 2\mathbf{k})$, and their difference as a function of p_x for fixed remaining components of $\mathbf{p}$ assumes values of the same magnitude but of opposite signs at the boundary of their range of definition. Consequently, there exists at least one value of $p_x = p_0$ for which ω_1 is equal to ω_2. Such states form a surface of dimension $n - 1$, where n is the dimension of the physical space in which excitons are confined. In the case when the lower level is symmetric relative to reflection in the plane $p_x = 0$, this surface is defined by the equation $p_x = k$. This situation will be considered by us below (which, however, does not lead to any loss of generality).

In order to confirm the above qualitative description of the evolution of the system under conditions of coherent confinement of the exciton population, we take into account spontaneous transitions and relaxation in the exciton system, Let us first analyze the role of a spontaneous transition. The energy of upper levels is supplemented with the complex component $-i\gamma$, where γ is the spontaneous transition rate. The arrival of excitons to lower states is described by the integral terms taking into account the possibility of the arrival of an exciton from an upper level from states with different momenta $\mathbf{p}$. It should be noted that we do not specify the phonon branch corresponding to the exciting phonon field, but a spontaneous transition from an upper to a lower level is mainly due to the emission of longitudinal acoustic phonons which interact with excitons most strongly. A phonon emitted as a result of spontaneous transition of an exciton from an upper to a lower level has a wave vector which is at least not smaller than the wave vector k of the coherent phonon beam. A spontaneous transition from the upper exciton level to the lower one may also be accompanied by the emission of more than one phonon. In light of these remarks, it is natural to assume that the spontaneous transition from the upper exciton level to a state on the lower exciton level occurs with the same probability for all points of the Brillouin zone. In this case, the equation for the density matrix can be written in the form

$$\begin{aligned} i\frac{\partial}{\partial t}\hat{\rho}(\mathbf{p}) &= [\hat{\mathcal{H}}(\mathbf{p}), \hat{\rho}(\mathbf{p})] \\ &- i\gamma\{\delta_{3,i}\delta_{3,k} + \delta_{4,i}\delta_{4,k}, \hat{\rho}(\mathbf{p})\} \\ &+ i\gamma\overline{\rho_U(\mathbf{p})}(\delta_{3,i}\delta_{3,k} + \delta_{4,i}\delta_{4,k}), \\ \rho_U(\mathbf{p}) &= \rho_{3,3}(\mathbf{p}) + \rho_{4,4}(\mathbf{p}). \end{aligned} \tag{4}$$

Here, the braces indicate anticommutator and the subscripts label states (2). Averaging is carried out over the entire range of definition of $\mathbf{p}$.

We disregard at the moment other processes occurring in the exciton system (these processes will be taken into account phenomenologically later) and analyze the asymptotic behavior of an idealized system described by Eq. (4). The density matrix for $t \longrightarrow \infty$ is a steady-state solution of Eq. (4). Taking the trace of this equation and equating to zero the derivatives with respect to time, we can easily verify that $\rho_{3,3}(\mathbf{p})$ and $\rho_{4,4}(\mathbf{p})$ are constant in the steady state in the entire range of definition of $\mathbf{p}$; i.e., the upper levels are populated uniformly. Thus, while determining the steady-state solution of Eq. (4), we can replace the integral term by the values of $\rho_{3,3}(\mathbf{p})$ and $\rho_{4,4}(\mathbf{p})$ at the same point of the $\mathbf{p}$ space. As a result, we obtain a closed system of homogeneous linearly dependent equations for elements $\rho(\mathbf{p})$. Solving this system, we obtain

$$\rho_U(\mathbf{p}) = f(\mathbf{p})\chi(\mathbf{p}), \tag{5}$$

where $\chi(\mathbf{p}) = \mathrm{Sp}(\hat{\rho}(\mathbf{p}))$. Function f may be regarded as a steady-state population of upper levels under the conditions of the effect of coherent confinement of populations in the four-level system. In connection with the problem of coherent confinement of populations by laser radiation in an atomic system [9], the problem of steady-state population of upper levels in systems with a finite number of states was considered, for example, in [10]. Away from the position corresponding to the states of coherent confinement of populations in the case of high-intensity phonon radiation, the function $f(\mathbf{p})$ tends to 1/2; i.e., the intense phonon radiation saturates the exciton–exciton transition, and the populations of the upper and lower levels become equal. In the vicinity of $p_x = k$, function f has a Lorentzian dip to the value 0 at point k itself. The fact that function f is equal to zero indicates that, at this point of the $\mathbf{p}$ space, the state in which all excitons are in the bound state and do not interact with phonon radiation is stationary, and hence the upper levels are not populated. The width of the dip depends on the intensity of phonon radiation and on the rate of detuning (upon a displacement along p_x) of the energies of lower levels from the case in which the effect of coherent confinement of populations is realized ($\omega_1(\mathbf{p}) = \omega_2(\mathbf{p})$). The singularities of function f listed above are taken into account in the following approximation:

$$f(p_x) = \frac{1}{2}\left(1 - \frac{G^2}{G^2 + (p_x - k)^2}\right), \tag{6}$$

$$G = g\left(\frac{\partial}{\partial p_x}(\omega_2(\mathbf{p}) - \omega_1(\mathbf{p}))\bigg|_{p_x = k}\right)^{-1}. \tag{7}$$

In contrast to atomic systems, relaxation processes in the exciton system are extremely diversified and are associated with various effects. Moreover, excitons possess a finite lifetime, and the exciton system itself, being a quasi-equilibrium system, may exist for a long time only in the presence of exciton pumping (e.g., by a laser). In order to take into account these effects, we use the relaxation time approximation for the density matrix assuming that the exciton system in zero external exciton field is completely characterized by the equilibrium density matrix $\hat{\rho}_0(\mathbf{p})$ and the time τ of relaxation to equilibrium. Taking the trace of Eq. (4), we obtain

$$\frac{\partial}{\partial t}\chi(\mathbf{p}) = 2\gamma(\overline{\rho_U(\mathbf{p})} - \rho_U(\mathbf{p})) - \frac{1}{\tau}(\chi(\mathbf{p}) - \chi_0(\mathbf{p})). \tag{8}$$

In this equation, however, the relation between functions χ and ρ_U is unknown. In order to derive this relation, we use the adiabatic approximation in which the equilibrium relative to induced transition in each tetrad of states is attained much faster than the equilibrium relative to exciton diffusion in the **p** space. Such an approximation is valid for $\gamma \ll g$. In this case, we can use dependence (5).

If we assume that f depends only on p_x, we can obtain the equation describing the one-dimensional exciton distribution integrated over the remaining direction of **p**. Let us now go over to the x space using the form of function f from (6) and assuming, for definiteness, that $p_x \in (0, 2k)$. This gives[3]

$$((e^{2ikx}-1)/(2kx)-1)\chi(x)$$

$$-\frac{1}{2}G\int e^{ik(x-x')-G|x-x'|}\chi(x')dx' = \nu(\chi(x)-\chi_0(x)), \quad (9)$$

$$\nu = (\gamma\tau)^{-1}.$$

The exponential factor in the integrand is just the Green's function of operator $(\partial/\partial x - ik)^2 - G^2$. Using this fact, we find that, for large $x \gg k^{-1}$ and such that $\chi_0(x) \longrightarrow 0$, function χ satisfies the following equation:

$$\left(\left(\frac{\partial}{\partial x}-ik\right)^2-\Delta p^2\right)\chi(x) = 0,$$

$$\chi(x) \sim \exp(ikx - \Delta p|x|), \quad (10)$$

$$\Delta p = \sqrt{\frac{\nu}{1+\nu}}G.$$

Large values of x correspond to small sizes in the momentum space. The smallest size in the momentum space is the distribution excitons trapped in the states of coherent confinement of populations. Result (10) correspond to the Lorentzian distribution of trapped excitons in the momentum space of width Δp:

$$\chi_u(p_x) = \frac{\Delta p}{\pi(\Delta p^2 + (p_x - k)^2)}. \quad (11)$$

In order to determine the number of excitons in the states of coherent confinement of populations, we approximately write the steady-state distribution over momenta p_x in the form

$$\chi(p_x) = n\chi_u(p_x) + (1-n)\chi_0(p_x). \quad (12)$$

Here, the value of n is the fraction of the total number of excitons in the states of coherent confinement of populations. This gives

$$n((f+\nu)(\chi_u-\chi_0) - \overline{(f+\nu)(\chi_u-\chi_0)}) + (f\chi_0 - \overline{f\chi_0}) = 0. \quad (13)$$

In this expression, the arguments of the functions $f(p_x)$, $\chi_u(p_x)$, and $\chi_0(p_x)$ have been omitted for brevity. The value of n can be determined from the requirement of the minimum root-mean-square value of the expression on the left-hand side of this equation, which gives

$$n = \frac{\overline{(f+\nu)(\chi_u-\chi_0)f\chi_0} - \overline{(f+\nu)(\chi_u-\chi_0)}\,\overline{f\chi_0}}{\overline{((f+\nu)(\chi_u-\chi_0))^2} - \overline{(f+\nu)(\chi_u-\chi_0)}^2}. \quad (14)$$

We can easily determine the asymptotic behavior of the relative number of excitons in the states of coherent confinement of populations, e.g., in the limit of a wide equilibrium distribution of excitons ($\chi_0 \equiv \mathrm{const}(p_x)$):

$$n = \begin{cases} 1 - \dfrac{2k\sqrt{\nu}}{\pi G}, & \gamma\tau = \nu^{-1} \gg k/G \\ \dfrac{2\pi G}{k\nu}, & \gamma\tau \ll k/G. \end{cases}$$

The rate of pumping of excitons in the state of coherent confinement of populations is determined by the rate γ of spontaneous transition from the upper to the lower level. Thus, in the case of insignificant relaxation (when the pumping rate γ is much higher than the relaxation rate τ^{-1}), almost all excitons are trapped in the states of coherent confinement. In the opposite case of strong relaxation as compared to the pumping rate, the described effect is insignificant.

Thus, we have considered the possible realization of the effect of exciton cooling by a high-intensity coherent phonon beam. The decisive role of the umklapp effects and a considerable role of relaxation in the effect under investigation have been analyzed.

This work was supported by grants from INTAS, the Russian Foundation for Basic Research, and the program "Physics of Semiconducting Nanostructures."

REFERENCES

1. *Bose-Einstein Condensation,* Ed. by A. Griffin, D. W. Snoke, and S. Stringari (Cambridge Univ. Press, Cambridge, 1995); A. L. Ivanov, H. Haug, and L. V. Keldysh, Phys. Rep. **296**, 237 (1998); L. V. Keldysh and Yu. V. Kopaev, Fiz. Tverd. Tela (Leningrad) **6**, 2791 (1964) [Sov. Phys. Solid State **6**, 2219 (1965)]; B. I. Halperin and T. M. Rice, Solid State Phys. **21**, 115 (1968).
2. Yu. E. Lozovik and O. L. Berman, Pis'ma Zh. Éksp. Teor. Fiz. **64**, 526 (1996) [JETP Lett. **64**, 573 (1996)]; Yu. E. Lozovik, O. L. Berman, and V. G. Tsvetus, Phys. Rev. B **59**, 5627 (1999); Yu. E. Lozovik and V. I. Yudson, Pis'ma Zh. Éksp. Teor. Fiz. **22**, 36 (1975) [JETP Lett. **22**, 11 (1975)]; Solid State Commun. **18**, 628 (1976); A. V. Klyuchnik and Yu. E. Lozovik, J. Low Temp. Phys. **38**, 761 (1980); J. Phys. C **11**, L483 (1978); S. I. Shevchenko, Phys. Rev. Lett. **72**, 3242 (1994); Yu. E. Lozovik and A. V. Poushnov, Phys. Lett. A **228**, 399 (1997); Xuejun Zhu, P. B. Littlewood, M. S. Hybertsen, and T. M. Rice, Phys. Rev. Lett. **74**, 1633 (1995); Y. Naveh and B. Laikhtman, Phys. Rev. Lett. **77**, 900 (1996); A. Imamog̅lu, Phys. Rev. B **57**, R4195 (1998);

---

[3] Formally, we must use the expansion of function χ into a Fourier series and not into a Fourier integral. However, for our purpose (formula (11)) both descriptions give the same result, so we can use the expansion into a Fourier integral for the sake of brevity.

S. Conti, G. Vignale, and A. H. MacDonald, Phys. Rev. B **57**, R6846 (1998); Yu. E. Lozovik and I. V. Ovchinnikov, Pis'ma Zh. Éksp. Teor. Fiz. **72** (8), 671 (2000) [JETP Lett. **72**, 431 (2000)]; Solid State Commun. (in press).

3. A. V. Larionov, V. B. Timofeev, J. Hvam, and C. Soerensen, Pis'ma Zh. Éksp. Teor. Fiz. **71**, 174 (2000) [JETP Lett. **71**, 117 (2000)]; L. V. Butov and A. I. Filin, Phys. Rev. B **58**, 1980 (1998); V. Sivan, P. M. Solomon, and H. Strikman, Phys. Rev. Lett. **68**, 1196 (1992); J.-P. Cheng, J. Kono, B. D. McCombe, *et al.*, Phys. Rev. Lett. **74**, 450 (1995); T. Fukuzawa, E. E. Mendez, and J. M. Hong, Phys. Rev. Lett. **64**, 3066 (1990); L. V. Butov, A. V. Mintsev, Yu. E. Lozovik, *et al.*, Phys. Rev. B **62**, 1548 (2000).
4. A. L. Dobryakov, V. A. Karavinskii, S. A. Kovalenko, *et al.*, Pis'ma Zh. Éksp. Teor. Fiz. **71**, 430 (2000) [JETP Lett. **71**, 298 (2000)]; V. M. Farztdinov, Yu. E. Lozovik, N. P. Ernsting, *et al.*, Phys. Rev. B **56**, 4176 (1997).
5. Yu. E. Lozovik and V. A. Sharapov (in press).
6. I. C. Rodriguez, S. S. Makler, and E. V. Anda, Braz. J. Phys. **26**, 694 (1999); S. S. Makler, I. Camps, J. Weberszpil, and D. E. Tuyarot, J. Phys.: Condens. Matter **12**, 3149 (2000); P. A. Fokker, R. S. Meltzer, Y. P. Wang, *et al.*, Phys. Rev. B **55**, 2934 (1997); J. Y. Prieur, M. Devaud, J. Joffrin, *et al.*, Physica B (Amsterdam) **220**, 235 (1996); S. T. Zavtrak, Phys. Rev. E **51**, 2480 (1995); J. Y. Prieur, R. Höhler, J. Joffrin, and M. Devaud, Europhys. Lett. **24**, 409 (1993).
7. Yu. E. Lozovik, S. P. Merkulova, and I. V. Ovchinnikov, Phys. Lett. A (in press).
8. J. Bardeen and W. Shockley, Phys. Rev. **80**, 72 (1950); A. Anselm and Yu. A. Firsov, Zh. Éksp. Teor. Fiz. **28**, 151 (1955).
9. A. Aspect, E. Arimondo, R. Kaiser, *et al.*, Phys. Rev. Lett. **61**, 826 (1988).
10. B. D. Agap'ev, M. B. Gornyĭ, B. G. Matisov, and Yu. V. Rozhdenstvenskiĭ, Usp. Fiz. Nauk **163** (9), 1 (1993) [Phys. Usp. **36**, 763 (1993)].

Translated by N. Wadhwa

JETP Letters, Vol. 73, No. 10, 2001, pp. 529–531. Translated from Pis'ma v Zhurnal Éksperimental'noĭ i Teoreticheskoĭ Fiziki, Vol. 73, No. 10, 2001, pp. 598–600.
Original Russian Text Copyright © 2001 by Yakimov, Dvurechenskiĭ, Nikiforov.

Spatial Separation of Electrons in Ge/Si(001) Heterostructures with Quantum Dots

A. I. Yakimov*, A. V. Dvurechenskiĭ, and A. I. Nikiforov
Institute of Semiconductor Physics, Siberian Division, Russian Academy of Sciences,
pr. Akademika Lavrent'eva 13, Novosibirsk, 630090 Russia
** e-mail: yakimov@isp.nsc.ru*

Received April 10, 2001

It is shown experimentally that the excitation of interband optical transitions in arrays of Ge/*n*-Si(001) quantum dots leads to a decrease in the concentration of electrons in the conduction band. The phenomenon observed is due to the formation of negatively charged exciton complexes in Ge islands and represents the first experimental confirmation of the spatial separation of electrons in the silicon matrix surrounding the islands. *© 2001 MAIK “Nauka/Interperiodica”.*

PACS numbers: 73.21.La; 71.35.-y

One of the promising methods for generating assemblies of quantum dots (QDs) is based on the use of kinetic effects in morphological changes at the surface of semiconductors during heteroepitaxy. At a large mismatch of the lattice constant, semiconductor layers will grow by the Stranski–Krastanov mechanism. The growth of a germanium film for the Ge/Si(001) system is first carried out layer by layer up to a thickness of four or five monolayers, and then a transition to the three-dimensional growth of pyramidal Ge nanoclusters (quantum dots) takes place. These nanoclusters provide partial relaxation of elastic strains in the heteroepitaxial structure [1].

The Ge/Si structures with Ge quantum dots relate to the second-kind heterojunctions in which electrons and holes reside in potential wells located on different sides of the heterojunction (Fig. 1), forming spatially indirect excitons. Such an unusual electronic configuration opens new possibilities both in fundamental research and for instrumental applications [2]. Here, the conduction band of one of the materials (Si) is close to the valence band of the other (Ge), which results in the spatial separation of carriers. In the given case, holes are localized in Ge nanoclusters, whereas there is a potential barrier for electrons in Ge. However, the localization of holes in Ge leads to a change in the behavior of the potential in the surrounding silicon matrix. A consequence of this change is the possibility of the formation of a potential well around Ge islands for electrons and the formation of electron states bound in this well [3]. The modeling of the electron structure of exciton complexes carried out in [3, 4] predicts that, on successively adding excitons to pyramidal Ge nanoclusters in Si(001), holes are concentrated in Ge in the vicinity of the base of a pyramid, and electrons are alternately localized in Si either in the vicinity of the apex of a Ge pyramid or in the vicinity of the boundary between Si and the wetting Ge layer (Fig. 1b). Though the physical nature of the spatial separation of electrons in silicon is clear (this separation minimizes the Coulomb repulsion of electrons), no experimental evidence of such an unusual electron configuration has been obtained so far.

In this work, the occurrence of the spatial separation of electrons presented in Fig. 1 has been confirmed experimentally. The idea of the experiment can be outlined as follows: It is known that the position of the chemical potential in the impurity band of doped semiconductors in the case of weak compensation is determined by the concentration of so-called 0- and 2-complexes [5]. If there is none of the ionized donors in the vicinity of a given acceptor, this object is named 0-complex. If two ionized donors are arranged on the opposite sides of an acceptor, this is a 2-complex. Shklovskiĭ and Éfros [5] showed that the formation of 2-complexes is favorable in energy; that is, a negatively charged acceptor can hold together two positively charged donors on its opposite sides. This statement can also be extended to the case of a charged exciton complex composed of a hole in a Ge island and two electrons located above and below the pyramid. Calculations in the self-consistent field approximation presented in [6] showed that, given the spatial separation of electrons, $N + 1$ electrons can be held in the vicinity of a Ge QD containing $N < 4$ holes, forming an artificial “ion.”[1] Consider silicon of the *n* type containing Ge nanoclusters. In the case of interband illumination, electrons and holes are excited in pairs, a hole is captured in a Ge island, and an electron occupies the lowest

---

[1] Actually, the valley degeneracy factor in Si was not taken into account in [6]. Taking into account this factor leads to the conclusion that an “excess” electron can be held at $N < 8$.

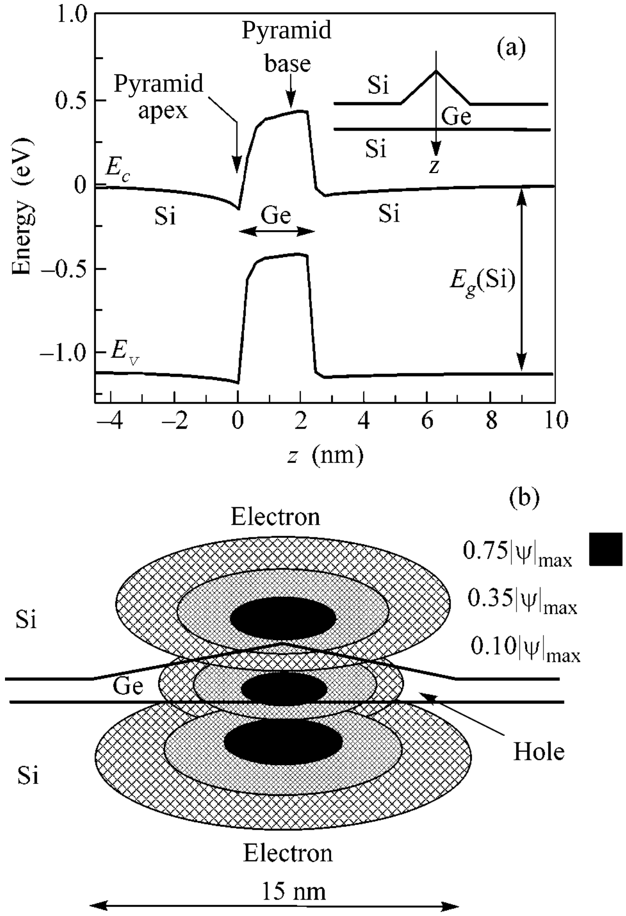

Fig. 1. (a) Calculated profile of conduction and valence bands along the *z* axis passing through the vertex of a Ge pyramid [4]. (b) Calculated structure of the wave functions of two electrons and a hole localized in the vicinity of a Ge pyramid [3]. Gradations of gray color correspond to regions at whose boundaries the wave functions drop down to levels of 75, 35, and 10%. The pyramid resides on an underlying continuous Ge layer and surrounded by silicon on all sides (see the inset in (a)). The pyramid base is 15 × 15 nm in size. The calculation was performed with allowance made for the nonuniform distribution of elastic deformations in the heterosystem within the Hartree approximation [3].

bound state in energy in the conduction band of Si in the vicinity of the apex of a germanium pyramid. Because one hole can hold two electrons at a QD, an equilibrium electron will be captured in the potential well located under the island, and the concentration of electrons in Si will decrease under conditions of illumination. Note that the concentration of free carriers usually increases upon illumination. Therefore, measuring experimentally the change in the concentration of free electrons under conditions of interband illumination leads to the conclusion that the electron configuration presented in Fig. 1 exists. Previously, indirect arguments about the photoinduced localization of equilibrium electrons in the potential of nonequilibrium holes were given in [6].

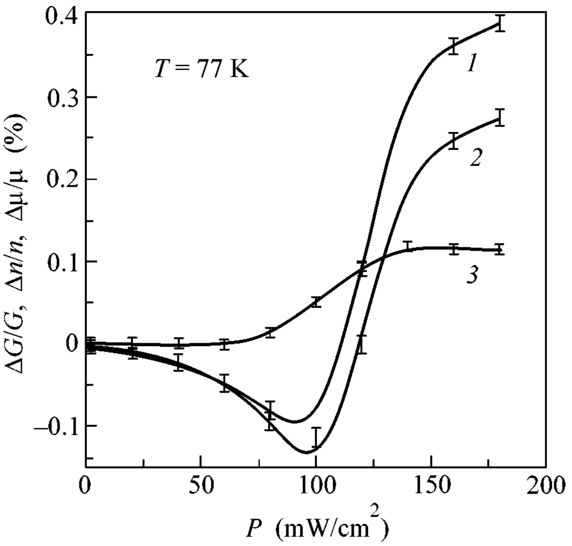

Fig. 2. Dependence of (*1*) the relative photoconductivity, (*2*) the relative change in the concentration of electrons in the Si conduction band, and (*3*) the Hall mobility on the intensity of interband illumination.

To verify the notions outlined above, we investigated epitaxial Ge/Si structures grown on a Si(001) substrate with a phosphorus concentration of $N_s \approx 10^{15}$ cm^{-3}. The samples consisted of ten layers of Ge islands separated with Si spacers 30 nm thick. The concentration of donors (Sb) in the epitaxial Si layer was 3×10^{16} cm^{-3}. Ge nanoclusters were shaped as pyramids with an average size of the base of 15 nm and a height of 1.5 nm. The layer density of nanoclusters in each layer was $\approx 3 \times 10^{11}$ cm^{-2}. A GaAs light-emitting diode (LED) whose radiation maximum was at a wavelength of ~0.9 μm was used as the light source. The intensity of the LED radiation was modulated with a frequency of 2 kHz. The photoconductivity (PC) and the Hall coefficient were measured by the van der Pau method at the modulation frequency using a lock-in nanovoltmeter. This allowed small variations of the resistance and the Hall emf to be measured upon illumination of the structures. In order to exclude the illumination of contacts, which may result in a spurious PC [7], the contacts themselves and the region around the contacts were protected with a nontransparent coating.

Experimental curves of the relative PC $\Delta G/G$, the relative change in the concentration of electrons $\Delta n/n$, and the relative change in the Hall mobility $\Delta\mu/\mu$ are shown in Fig. 2 as functions of the illumination power P at $T = 77$ K. In accordance with the notions outlined above, a decrease in the concentration of electrons is actually observed upon illumination in the range $P =$ 0–100 mW/cm^2. This decrease is accompanied with the appearance of a negative photoconductivity. The mobility remains virtually unchanged at $P < 70$ mW/cm^2 and weakly increases at more intense illumination. The growth of mobility is apparently associated with the fact that a positively charged nucleus cannot hold an "excess" electron as the number of holes in the QD increases. Therefore, scattering from "ions" (N holes + (N + 1) electrons) gives way to weaker scattering from dipoles (N holes + N electrons). The decrease in the binding energy of the "excess" electron in the field of N holes at large N can also be explained by the change in the sign of Δn and ΔG at $P > 100$ mW/cm^2.

Thus, it was found that the concentration of electrons in the conduction band of Ge/Si(001) heterostructures with germanium quantum dots decreases upon illumination that leads to interband transitions. The reason for this behavior is the formation of negatively charged "ions." This possibility of this formation is due to the spatial separation of electrons at Si/Ge heteroboundaries.

This work was supported by the Russian Foundation for Basic Research, project no. 00-02-17885.

REFERENCES

1. O. P. Pchelyakov, Yu. B. Bolkhovityanov, A. V. Dvurechenskiĭ, *et al.*, Fiz. Tekh. Poluprovodn. (St. Petersburg) **34**, 1281 (2000) [Semiconductors **34**, 1229 (2000)].
2. Zh. I. Alferov, Fiz. Tekh. Poluprovodn. (St. Petersburg) **32**, 3 (1998) [Semiconductors **32**, 1 (1998)].
3. A. I. Yakimov, N. P. Stepina, A. V. Dvurechenskii, *et al.*, Phys. Rev. B **63**, 45312 (2001).
4. A. I. Yakimov, N. P. Stepina, A. V. Dvurechenskii, *et al.*, Semicond. Sci. Technol. **15**, 1125 (2000).
5. B. I. Shklovskiĭ and A. L. Éfros, *Electronic Properties of Doped Semiconductors* (Nauka, Moscow, 1979; Springer-Verlag, New York, 1984).
6. A. I. Yakimov, A. V. Dvurechenskii, A. I. Nikiforov, *et al.*, Phys. Rev. B **62**, R16283 (2000).
7. V. G. Kustov, Fiz. Tekh. Poluprovodn. (Leningrad) **10**, 2215 (1976) [Sov. Phys. Semicond. **10**, 1318 (1976)].

Translated by A. Bagatur'yants

JETP Letters, Vol. 73, No. 10, 2001, pp. 532–535. From Pis'ma v Zhurnal Éksperimental'noĭ i Teoreticheskoĭ Fiziki, Vol. 73, No. 10, 2001, pp. 601–604.
Original English Text Copyright © 2001 by Gasparov, Sidorov, Zver'kova, Kulakov.

Electron Transport in Diborides: Observation of Superconductivity in ZrB_2[1]

V. A. Gasparov*, N. S. Sidorov, I. I. Zver'kova, and M. P. Kulakov
Institute of Solid State Physics, Russian Academy of Sciences, Chernogolovka, Moscow region, 142432 Russia
** e-mail: vgasparo@issp.ac.ru*
Received April 12, 2001

We report on syntheses and electron transport properties of polycrystalline samples of diborides (AB_2) with different transition metals atoms (A = Zr, Nb, Ta). The temperature dependence of resistivity, $\rho(T)$, and *ac* susceptibility of these samples reveal a superconducting transition of ZrB_2 with $T_c = 5.5$ K, while NbB_2 and TaB_2 have been observed to be nonsuperconducting up to 0.37K. $H_{c2}(T)$ is linear in temperature below T_c, leading to a rather low $H_{c2}(0) = 0.1$ T. At T close to T_c, $H_{c2}(T)$ demonstrates a downward curvature. We conclude that these diborides, as well as MgB_2 samples, behave like simple metals in the normal state with usual Bloch–Grüneisen temperature dependence of resistivity and with Debye temperatures 280, 460, and 440 K for ZrB_2, NbB_2, and MgB_2, respectively, rather than T^2 and T^3, as previously reported for MgB_2. *© 2001 MAIK “Nauka/Interperiodica”.*

PACS numbers: 74.25.Fy; 74.72.-h

The recent discovery of Akimitsu [1] of superconductivity in MgB_2 at 39 K has lead to a booming activity in the physics community. It was reported that measurements of the upper critical field, $H_{c2}(T)$, and the thermodynamic critical field, $H_c(T)$, as well as the specific heat, are all consistent with MgB_2 being a fairly typical intermetallic electron phonon mediated BCS superconductor with a superconducting transition temperature approximately twice that of a typical “metallic” superconductor. At the same time, an unexpected T^2- and even T^3-normal state temperature dependence of the resistance has been reported [2, 3]. These results have initiated considerable interest in electron transport measurements and in a search for superconductivity in other diborides. Natural candidates for this search are AB_2-type light metal diborides (A = Li, Be, Al). However, up to now superconductivity has not been reported in the majority of these compounds [4–6]. Only very recently has superconductivity below 1 K ($T_c = 0.72$ K) been reported in $BeB_{2.75}$ [7]. According to [8], no superconducting transition down to 0.42 K has been observed in powders of diborides of transition metals (A = Ti, Zr, Hf, V, Ta, Cr, Mo, U). Only NbB_2 was found to be superconducting with very low $T_c = 0.62$ K. Since completing this work, we have become aware of a recent paper [9] in which superconductivity was observed in TaB_2 at $T_c = 9.5$ K. This result contradicts the data reported in this letter.

The crystal structure of diborides (ω phase [10]) can be viewed as a set of two-dimensional graphite-like monolayers of boron atoms with honeycomb lattice, intercalated with A atoms monolayers forming ABAB heterostructure. It was proposed that superconductivity in a series of diborides of light metals (A = Be, Mg, Ca, Al) and a series of transition metals (A = Ti, Zr, Hf, V, Nb, Ta) appears near a critical point in a strain and charge density phase diagram. An increase of the B–B distance larger than a critical value driven by A atom radii results in collapse of the ideal ω phase into the trigonal rumpled ω phase. Lattice instability driven by both atom radii and charge densities may be a key reason why superconductivity appears in MgB_2 rather than in other diborides. This phase diagram suggests that ZrB_2 is a good candidate for superconductivity having strain close to the critical value (see [10]). In order to clarify whether this assumption is correct, we studied the electron transport properties of ZrB_2, NbB_2, TaB_2, and MgB_2.

Polycrystalline samples of ZrB_2 and NbB_2 were obtained by conventional solid state reaction. Starting materials were Zr and Nb metal powders (99.99% purity) and submicron amorphous boron powder (99.9% purity). These materials were lightly mixed in appropriate amounts and pressed into a pellet 10 mm thick and 20 mm in diameter. The pellets were placed on *W* foil, which was in turn placed between two *W* ingots. These whole assembly was burned at 1700°C for two hours in an *HV* chamber at 2×10^{-4} Pa by *e*-beam heating of *W* ingot. The TaB_2 samples were pre-

---

[1] This article was submitted by the authors in English.

pared in the same way from TaB_2 powder (Donetsk Factory of Chemicals).

The resulting ceramic pellets had over 60–90% of the theoretical mass density and were black in color. They demonstrated good metallic conductivity at low temperatures. After regrinding the prepared pellets in an agate mortar, the respective powders were placed in a tungsten can and melted by *e*-beam heating of the *W* crucible for a few minutes in an *HV* chamber at 1×10^{-4} Pa. The resulting melt had shiny single crystals about 0.1 mm in size on top with solid polycrystalline ingot underneath between melted *W* can walls. However, these single crystals were found to be nonsuperconducting due to the presence of a high concentration of *W* impurities observed from XRD. The MgB_2 samples were sintered from metallic Mg plates placed on top of boron-pressed pellets. The pellets were placed on Mo foil, which was in turn placed on a Mo crucible. The crucible, with foil and pellets, was burned for two hours at 1400°C in a tube furnace under an Ar pressure of 20 atm, with subsequent cooling to room temperature when the furnace was turned off.

An X-ray θ–2θ scan diffraction pattern (see Fig. 1) was obtained using CuK_α radiation. The measurements showed the samples of all diborides to consist largely of the desired AlB_2 phase. We would like to note that a small amount of ZrB_{12} impurity phase was found to be present after the first step of preparation. This phase was washed out after subsequent regrinding and annealing. The X-ray diffraction pattern was indexed within a hexagonal unit cell (space group *P*6/*mmm*). This crystal structure consists of honeycomb-net planes of boron, separated by triangular planes of the metals. The analysis of the data yielded following values of the lattice parameters: a = 3.170 Å and c = 3.532 Å for ZrB_2, a = 3.111 Å and c = 3.267 Å for NbB_2, and a = 3.087 Å and c = 3.247 Å for TaB_2. All parameters are in good agreement with published data [11].

For resistive measurements, we used following sample preparation procedure: the pellets were first cut by using a diamond saw with ethyl alcohol as coolant. Rectangular solid bars of about 0.5 × 0.5 × 6 mm size were obtained from pellets by using the spark erosion method. A standard four-probe *ac* (9 Hz) method was used for resistance measurements. Silver Print was used for making electrical contacts. The samples were mount in a liquid helium cryostat able to regulate the temperature from 1.8 K to room temperature. We employed a radio frequency (RF) coil technique for *ac* susceptibility measurement [12]. Magnetoresistivity measurements utilizing a superconducting magnet were also performed. A well-defined geometry of the samples allowed us to perform accurate measurements of resistivity with the magnetic field applied perpendicularly to the direction of electric current.

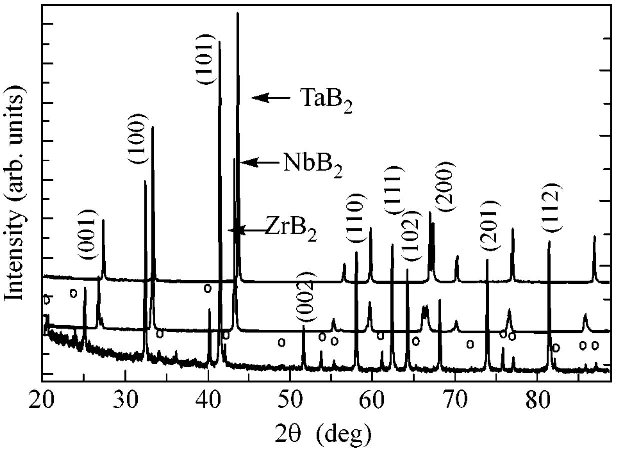

Fig. 1. X-ray θ–2θ scan of ZrB_2, NbB_2, and TaB_2 pellets at room temperature. The cycles mark the reflections from cubic ZrB_{12} (a = 7.388 Å) impurity.

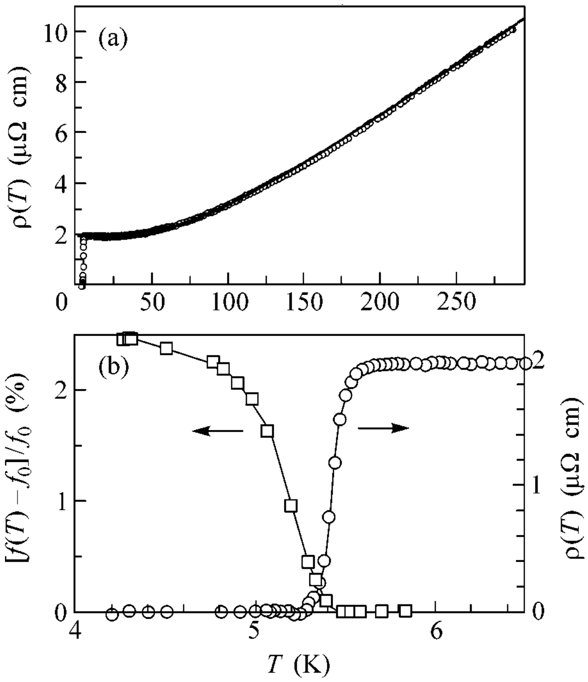

Fig. 2. (a) Typical temperature dependence of the resistivity of ZrB_2 sample. Symbols denote the data and the solid line is Bloch–Grüneisen law fit with Debye temperature 280 K. (b) Low-temperature dependence of the *ac* susceptibility (proportional to the frequency shift $[f(T) - f_0]/f_0$—left axis) measured with the frequency $f_0 = f(6\ \mathrm{K}) = 9$ MHz, and the resistivity (right axis) in ZrB_2.

Figure 2 shows the typical temperature dependence of the resistivity for ZrB_2 samples. The resistivity exhibits a very sharp superconducting transition at 5.5 K shown in Fig. 2b. The transition width is about 0.14 K for a 10 to 90% drop. Such a narrow transition is a characteristic of good quality superconducting material. The resistivity value 10 μΩ cm at room temperature is almost the same as that of MgB_2 (see Fig. 4), whereas the residual resistivity is about 2 μΩ cm. One

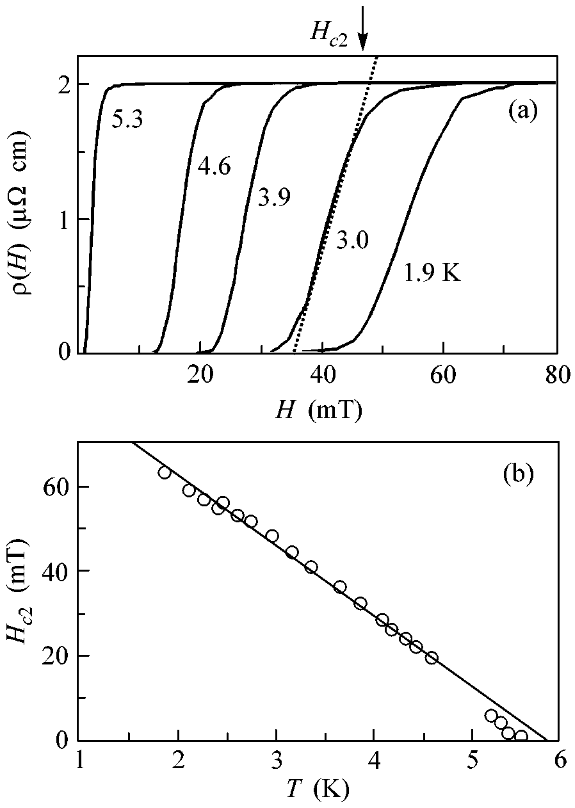

Fig. 3. (a) Magnetic field resistive transition curves in ZrB_2 sample at different temperatures. The dashed line is drawn through the $\rho(H)$ dependence with maximal $d\rho/dH$ derivative for illustration of the H_{c2} determination. (b) Temperature variation of the upper resistive critical magnetic field $H_{c2}(T)$ in ZrB_2 sample.

should note that the temperature dependence of the resistivity bellow 150 K may be fitted by a square law, $\rho(T) = a + b \times T^2$, characteristic for electron–electron scattering [13]. Nevertheless, the overall temperature dependence of resistivity can be perfectly fitted with the classical Bloch–Grüneisen law (solid line), with rather low Debye temperature, $T_D = 280$ K.

Figure 2b shows temperature dependence of the normalized real part of *ac* susceptibility and the resistivity, $\rho(T)$, in the same ZrB_2 sample as on Fig. 2a. For this type of measurements, the sample is placed inside the inductance coil of *LC* circuit, and the resonant frequency of this circuit is monitored as a function of temperature. The temperature dependence of the sample *ac* susceptibility $\chi(T)$ causes changes in inductance L and in turn the resonant frequency $f(T)$ of the circuit, $\Delta f/f \propto -\mathrm{Re}\chi$. Susceptibility data of Fig. 2a clearly show the superconducting transition in ZrB_2 sample at 5.5 K. The onset temperature of the *ac* susceptibility corresponds to the end point resistance transition, typical for superconducting transition.

Figure 3 shows magnetic-field-dependent electrical resistivity data taken at a variety of temperatures. Using these data, the resistive upper critical magnetic field, $H_{c2}(T)$, can be extracted from each curve. We can do it by extending the $\rho(H)$ line with maximum $d\rho/dH$ up to the normal state (see the dotted line). Figure 3b presents temperature dependence of the $H_{c2}(T)$ for a ZrB_2 sample derived from this extrapolation. Contrary to conventional theory [14], we found that the $H_{c2}(T)$ dependence is linear over an extended region of T with some downward curvature close to T_c. This leads to a rather low zero temperature value of $H_{c2}(0) = 0.1$ T ($\xi(0) = 570$ Å), which is significantly smaller than for MgB_2 (18 T) [15]. Such a linear H_{c2} (T) dependence is characteristic for 2D superconductors [16] and was also observed in MgB_2 [15] wires and $BaNbO_{3-x}$ films [17, 18]. The results of extended study of the $H_{c2}(T)$ dependence ZrB_2 samples will be discussed elsewhere.

Figure 4 shows the temperature dependences of the resistivity for NbB_2 and MgB_2 samples. Best fits were obtained using the classical Bloch–Grüneisen law rather than $a + b \times T^2$ or $a + b \times T^3$ forms previously reported for MgB_2 [2, 3]. The solid fitting lines with the Bloch–Grüneisen form in Fig. 4 nearly overlays the data. The Debye temperatures derived from these fits are rather high in comparison with ZrB_2, i.e., 460 and 440 K for NbB_2 and MgB_2, respectively. The T_c value for the MgB_2 samples is the same that is found elsewhere, i.e., 39 K [1–3]. We suggest that previously reported T^2 and T^3 dependences of the resistivity of MgB_2 may be due to rather high residual resistance, $\rho(0)$, of the samples and respectively weak $\rho(T)$ dependence. Our data are well consistent with the Bloch–Grüneisen law, which is characteristic for electron–phonon scattering [13]. Nevertheless, we believe that only data obtained on high purity single crystals can solidify this conclusion. Note that the resistivity ratio for all diborides studied is approximately 5 rather than 10000 or even a few million as for pure metals [13].

In contrast to the data of [9], our *RF* susceptibility measurements of TaB_2 samples did not reveal any superconducting transition. At the same time, our XRD data have shown the same [9] clear AlB_2 spectra (see Fig. 1). In contrast to [9], we did not find any impurities in our TaB_2 samples from XRD data (see Fig. 1). Our resistive measurements up to 0.37 K do not show any superconducting transition in NbB_2 either. This contradicts the *ac* susceptibility data of [8], which reports the superconducting transition in NbB_2 to be at 0.62 K. We observed the superconducting transition at 4.4 K in melted TaB_2 samples, while the XRD data of these samples revealed the presence of metallic Ta impurities. We believe these contradictions are due to the different sample preparation technique of [8, 9]. The samples used in those papers were prepared using a borothermic method from Nb_2O_5 and Ta_2O_5 pentoxides and boron [19]. Therefore, those samples might consist of reduced Nb and Ta oxides intercalated by boron, which could be

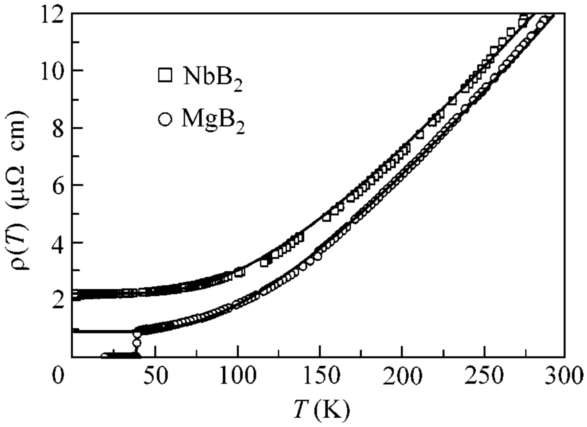

Fig. 4. Typical temperature dependence of the resistivity of NbB_2 and MgB_2 samples. The solid lines denotes the Bloch–Grüneisen law fit with Debye temperatures 440 and 460 K for MgB_2 and NbB_2, respectively.

the source of superconducting transition. Recently, we have shown that oxygen-reduced $BaNbO_{3-x}$ compounds exhibit superconducting transition even at T_c = 22 K [17, 18]. Also, since the superconductivity in TaB_2 was not observed before on the samples made by the same technique [8], the reason for this discrepancy with data obtained in [9] should be emphasized from resistance measurements. Therefore, care must be taken for sample preparation and composition before final conclusions about superconductivity in NbB_2, TaB_2, and other diborides can be drawn.

In summary, we report the temperature dependence resistivity and high frequency susceptibility measurements of synthesized samples of ZrB_2, NbB_2, TaB_2, and MgB_2. We discovered a superconducting transition at 5.5 K in ZrB_2 samples. The superconducting transition width for the resistivity measurement was about 0.14 K, and the resistivity in the normal state followed a classical Bloch–Grüneisen behavior in all diborides studied. The linear $H_{c2}(T)$ dependence was observed for ZrB_2 samples over an almost full range of temperatures below T_c, leading to a rather low $H_{c2}(0)$ = 0.1 T. A superconducting transition was not found in NbB_2 samples up to 0.37 K or in TaB_2 samples above 4.4 K.

We gratefully acknowledge helpful discussions with V.F. Gantmakher, measurements of $\rho(T)$ dependence in NbB_2 samples up to 0.37 K by V.N. Zverev, help in manuscript preparation from L.V. Gasparov, and help in samples preparations from S.N. Ermolov, V.V. Lomejko and V.G. Kolishev. This work was supported by the Russian Council on High-Temperature Superconductivity (grant no. Volna 4G) and the Russian Scientific Program: Surface Atomic Structures (grant no. 4.10.99).

REFERENCES

1. J. Nagamatsu, N. Nakagawa, T. Muranaka, *et al.*, Nature **410**, 63 (2001).
2. C. U. Jung, Min-Seok Park, W. N. Kang, *et al.*, cond-mat/0102215 (2001).
3. D. K. Finnemore, J. E. Ostenson, S. L. Bud'ko, *et al.*, cond-mat/0102114 (2001).
4. J. S. Slusky, N. Rogado, K. A. Regan, *et al.*, cond-mat/0102262 (2001).
5. I. Felner, cond-mat/0102508 (2001).
6. Y. G. Zhao, X. P. Zhang, P. Y. Qiao, *et al.*, cond-mat/0103077 (2001).
7. D. P. Young, P. W. Adams, J. Y. Chan, and F. R. Fronczek, cond-mat/0104063 (2001).
8. L. Leyarovska and E. Leyarovski, J. Less-Common Met. **67**, 249 (1979).
9. D. Kaczorowski, A. J. Zaleski, O. J. Zoga, and J. Klamut, cond-mat/0103571 (2001).
10. A. Bianconi, N. L. Saini, D. Di Castro, *et al.*, cond-mat/0102410 (2001).
11. Nat. Bur. Stand. Monogr., 25, 20, 113 (1983); *ibid*, 25, 21, 97 (1984); Wong-Ng *et al.*, Powder Diffr. **2**, 115 (1987).
12. V. A. Gasparov, M. R. Mkrtchyan, M. A. Obolensky, and A. V. Bondarenko, Physica C (Amsterdam) **231**, 197 (1994).
13. V. A. Gasparov and R. Huguenin, Adv. Phys. **42**, 393 (1993).
14. E. Helfand and N. R. Werthamer, Phys. Rev. **147**, 288 (1966).
15. S. L. Bud'ko, C. Petrovic, G. Lapertot, *et al.*, cond-mat/0102413 (2001).
16. D. E. Prober, R. E. Schwall, and M. R. Beasley, Phys. Rev. B **21**, 2717 (1980).
17. V. A. Gasparov, S. N. Ermolov, S. S. Khassanov, *et al.*, Physica B (Amsterdam) **284–288**, 1119 (2000).
18. V. A. Gasparov, S. N. Ermolov, G. K. Strukova, *et al.*, Phys. Rev. B **63**, 174512 (2001).
19. P. Peshev, L. Leyarovska, and G. Bliznakov, J. Less-Common Met. **15**, 259 (1968).

JETP Letters, Vol. 73, No. 10, 2001, pp. 536–539. Translated from Pis'ma v Zhurnal Éksperimental'noĭ i Teoreticheskoĭ Fiziki, Vol. 73, No. 10, 2001, pp. 605–608.
Original Russian Text Copyright © 2001 by Shikin.

Critical Width of Hall Incompressible Strips in Regularly Nonuniform 2D Electron Systems

V. Shikin

Institute of Solid-State Physics, Russian Academy of Sciences, Chernogolovka, Moscow region, 142432 Russia

Received April 12, 2001

A formalism for determining the critical width of Hall incompressible strips, which arise in regularly nonuniform 2D electron systems in the presence of a magnetic field, is proposed. Under equilibrium conditions, this width is determined by competition between the cyclotron and Coulomb energies at distances of about the critical width of a channel with integer filling factor. The calculations are applied to interpretation of available experimental data. © *2001 MAIK "Nauka/Interperiodica".*

PACS numbers: 73.43.Cd

A theory proposed by Chklovskii *et al.* [1, 2] for incompressible Hall strips in nonuniform 2D electron systems should involve a lower bound on strip width $2a$. In any case, there is the restriction

$$a_{\min} \geq l_H, \tag{1}$$

where l_H is the magnetic length. Indeed, each strip of width $2a_l$ is characterized by its local integer magnetic filling factor ν_l, which is well defined at distances larger than the magnetic length. Therefore, the semiphenomenological theory of strips [1, 2] loses its meaning at smaller distances.

In this work, we find that actual critical conditions for existing integer-factor strips are stringent because the structure of integer-factor strips in the electron density profile smears when the formalism [1, 2] is refined by nonuniform-origin corrections [the electron energy in a magnetic field in a nonuniform external potential $V(x)$ depends not only on the cyclotron frequency but also on the gradients of the potential $V(x)$]. An algorithm for estimating the "quality" of an individual incompressible channel in the approximation [1, 2] is proposed in the first part of the work. Then, based on the theory [1, 2], we discuss its modification taking into account a nonuniform external potential. In particular, this modification provides more definite determination of narrow strips in the electron density distribution to the point of disappearance. Specific calculations are performed for an unshielded Corbino disc. Relevant experiments [3], which were carried out in this geometry, testify, in our opinion, to existence of critical dimensions of incompressible strips.

1. Let us consider a 2D Corbino disk with planar terminals in the quasi-one-dimensional approximation, when $(R_1 - R_2)/(R_1 + R_2) \ll 1$, where R_1 and R_2 are, respectively, the outer and inner radii of the Corbino disk. A piecewise smooth solution to the contact Dirichlet problem for the electric potential gives the following nonuniform part $\delta n(x)$ of the electron density in the 2D region:

$$\begin{gathered}\delta n_o(x) = \frac{\kappa w W_{ab}}{\pi^2 e^2 (w^2 - x^2)}, \quad -w \leq x \leq +w; \\ \int_{-w}^{+w} ds \delta_o n(s)/(x - s) = 0.\end{gathered} \tag{2}$$

Here, $2w = R_2 - R_1$ is the width of the 2D region between metallic banks, the X axis is directed along a disc radius, the coordinate origin coincides with the center of the 2D region, k is the dielectric constant of the medium, and W_{ab} is the contact energy. In the limit $a_b^* \ll w$, approximation (2) is applicable far from the points $x = \pm w$, where a_b^* is the effective Bohr radius.

When a magnetic field normal to the 2D-system plane is applied, points with

$$\nu(x) = \pi l_H^2 (n_s + \delta n(x_l)) = l; \quad l = 1, 2, 3\ldots \tag{3}$$

arise in the electron-density profile. These points become the centers of appearance of integer-factor incompressible strips. Following [1], each strip will be analyzed separately.

Within a given lth strip, an initial equilibrium equation for a system of noninteracting 2D electrons (Chklovskii *et al.* [1, 2] also used the one-electron approximation) has the form

$$\begin{gathered}\mu(x) = e\varphi(x) + \zeta(\nu(x), H) = \text{const}, \\ \zeta(\nu(x), H) = -T \ln S(\nu, H),\end{gathered} \tag{4}$$

$$\begin{gathered}2S(H, T, \nu) = \left(\frac{1}{\nu} - 1\right) + \left[\left(\frac{1}{\nu} - 1\right)^2 + 4\epsilon\left(\frac{2}{\nu} - 1\right)\right]^{1/2}, \\ \epsilon = \exp(-\hbar\omega_c/T) \ll 1,\end{gathered} \tag{5}$$

0021-3640/01/7310-0536$21.00 © 2001 MAIK "Nauka/Interperiodica"

$$\nu(x) = \pi l_H^2 n(x), \quad l_H^2 = c\hbar/eH, \quad \nu < 2,$$
$$\kappa e\varphi'(x) = 2e^2\int_{-w}^{+w} ds\delta n(s)/(x-s), \tag{6}$$

where T is the temperature and the integral Poisson relation between the electric potential $\varphi(x)$ and the electron density $\delta n(x)$ takes into account the absence of additional shieldings in the problem.

In the vicinity of the point x_l, which is taken now as the coordinate origin, it is convenient to represent Eq. (4) in the form

$$\frac{2e^2\epsilon^{1/2}}{\kappa T}\int_{-a}^{+a} ds\frac{[\delta n(s) - \delta n_o(s)]}{(x-s)} = -\frac{d\nu}{dx}. \tag{7}$$

Equation (7) is derived by using the properties of the function $S(\nu)$ in Eq. (5) in the limit $\nu \longrightarrow 1$. In addition, the derivative of electric potential, which is induced by density $\delta n_o(x)$ (2), is omitted on both sides of Eq. (7) because this derivative equals zero according to Eq. (2). The quantity $\delta n(x)$ is noticeably disturbed only within the interval between the points a. As a result, the difference $\delta n(x) - \delta n_o(x)$ is nonzero within this interval with the center at the point x_l. This fact is used in Eq. (7), where the limits of integration $\pm w$ are replaced by $\pm a$ and influence of neighboring channels is ignored as in [1].

Equation (7) illustrates the causes of Hall flattening of the profile $n(x)$ in the vicinities of integer-factor points (3). The derivative $d\nu(x)/dx$ is exponentially small at these points because $\epsilon \longrightarrow 0$.

To quantitatively estimate $dn(x_l)/dx$, we set (as in [1])

$$\delta n(x) - \delta n_o(x) \simeq (n_l' - n_o')\delta x, \tag{8}$$

where δx is measured from the center of the given channel. After calculation of the resulting integral, Eq. (7) in the vicinity of the point x_l is reduced to the determination of n_l':

$$n_l' = n_o'/(1+\gamma); \quad \gamma = \pi\kappa T l_H^2/4ae^2\epsilon^{1/2} \gg 1. \tag{9}$$

Inequality $\gamma \gg 1$, which is valid due primarily to smallness of the parameter $\epsilon \longrightarrow 0$, is necessary for validity of simplified Eqs. (7) and (8).

An analysis of Eq. (7) can provide an estimate for the parameter $2a$ entering into Eq. (9). However, for further consideration, it is enough to take the estimate $2a$ from [1]

$$a^2 = 2\kappa\hbar\omega_c/(\pi^2 e^2 dn(x_o)/dx), \tag{10}$$

which is valid for $T \longrightarrow 0$.

Formula (9) provides a convenient criterion for determining “quality” of a strip. In the limiting case

$$\eta_l' \ll n_o', \tag{11}$$

an integer-factor channel is well defined. In the other limiting case

$$\eta_l' \le n_o', \tag{11a}$$

the channel loses properties characteristic for the integer-factor channel.

Criterion (11) indicates that the strip quality easily deteriorates as the temperature increases. This fact was also manifested in numerical calculations [4]. Thereby, the parameter γ appearing in Eq. (9) would specify how sharply the parameters of an individual strip are determined. However, this kind of degradation of strips is not dominant. When the theory proposed in [1] is naturally modified so that nonuniform-origin corrections are included in the determination of the electrochemical potential, the behavior of thin integer-factor strips changes.

2. Modifications of the theory described in [1] imply that definition (5) of function $S(\nu, H, T)$ for noninteracting 2D electrons in the quantization-inducing magnetic field is approximate. More correct representation of this function has the form (see [5, 6])

$$S(\nu, H, T) \longrightarrow S(\nu^*, H, T), \tag{12}$$

$$\nu^*(x) = \nu(x) - \frac{\pi l_H^2 e\delta\nu_l}{h\omega_c}\varphi''(x), \tag{12a}$$

where $\delta\nu_l$ is the jump of the integer part of the magnetic filling factor between neighboring Landau levels. In what follows, we take $\delta\nu_l = 1$.

Taking Eq. (12) into account, we write the equation

$$2\epsilon^{1/2}T^{-1}e\varphi' = -\nu' + \frac{\pi l_H^2 e}{h\omega_c}\varphi'''(x), \tag{13}$$

similar to Eq. (7), and solve it with respect to φ' under the boundary conditions

$$\varphi'(\pm a) = 0 \tag{13a}$$

and obtain

$$\lambda e\varphi' = -h\omega_c\left[\int_{-a}^{x} n'(s)\sinh\lambda(x-s)ds - \frac{\sinh\lambda(x+a)}{\sinh\lambda a}\int_{-a}^{+a} n'(s)\sinh\lambda(a-s)ds\right], \tag{14}$$

$$\lambda^2 a^2 = \frac{2a^2\epsilon^{1/2}h\omega_c}{\pi l_H^2 T} = \frac{h\omega_c}{\gamma V_a}, \quad V_a = \frac{2e^2}{\kappa a}, \tag{15}$$

where γ is defined in Eq. (9).

Parameter λa (15) controls the character of adjustment of the electron density in the integer-factor channel to thermodynamic-origin jumps of the function $S(\nu^*, H, T)$ in the vicinities of the singular points x_l (3). If $\lambda a \gg 1$, one deals with deformation (9). In the other

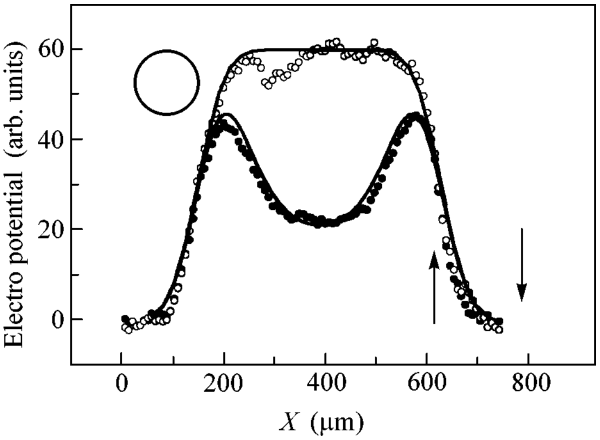

Gauss image $\phi(x)$ of the electric potential $\varphi(x)$ for the Corbino disk with the center of the 2D region at the point x_o = 390 μm. The solid lines are calculated for the normal and anomalous states by Eqs. (18)–(20). Open and closed circles are experimental data [3] measured at the magnetic field B = 7.9 and 8.5 T, at which the system is in the normal and anomalous states, respectively. The circle in the left upper part of the figure presents the actual dimensions of the laser beam. The interval between arrows in the right lower part of the figure is the range where the normal and anomalous states in the behavior of $\phi(x)$ overlap. The existence of this range testifies to the existence of the edge normal rings framing the anomalous region at the center of the disk.

limiting case $\lambda a \ll 1$, using Eqs. (14), (7), and (8), we obtain

$$n'_l = n'_o/(1+\delta); \quad \delta = 4e^2/(a\kappa h\omega_c). \tag{16}$$

Application of criterion (11a) to Eq. (16) gives

$$2a_{\min} = 8e^2/(\kappa h\omega_c). \tag{17}$$

3. Let us consider possible experimental consequences of Eq. (17). Under equilibrium conditions for which this formula has meaning, the 2D-system region, which is occupied by incompressible strips (in the multichannel variant of their appearance), would be expected to be separated from the edges of the 2D system by normal regions where the strips cannot exist. This pattern was actually observed in experiments on the linear electro-optical effect in the Corbino disk [3]. The open circles in the figure, which is taken from [3], show the electric potential in the normal state, when the 2D system is well conducting, whereas closed circles show the electrical potential in the anomalous state when the system of integer-factor strips arises in the central part of the Corbino disk. The problem of number of channels for data from [3] was discussed in [7]. In this case, the behavior of the electric potential near the Corbino disk edges, where the normal and anomalous data clearly overlap in a certain x interval, is of most interest. This interval is approximately marked by arrows in the figure and can exist only in the presence of the mechanism hindering appearance of narrow integer-factor channels in the regions with large gradients of electron density.

We use the following quantitative characteristics of the electric potential $\varphi(x)$. In the normal state, the potential has the form

$$\varphi(x) = \begin{cases} \varphi_o, & -w \le x \le +w \\ 0, & |x| \ge w, \end{cases} \tag{18}$$

where φ_o, nominal width $2w$, and radius R are determined by fitting Eqs. (18) and (20) to experimental data from [3].

Based on Eq. (2), we take the anomalous potential in the multichannel approximation in the form [7]

$$\varphi(x) = \begin{cases} c_1/(w^2 - x^2), & -x_c \le x \le +x_c \\ \varphi_o, & +x_c \le x \le +w \\ \varphi_o, & -w \le x \le -x_c. \end{cases} \tag{19}$$

The normalization of φ_o is identical for Eqs. (18) and (19). The constants c_1 and x_c provide the best approximation of data [3] for the quantum Hall regime by Eqs. (19) and (20) at fixed φ_o, w, and R.

To take into account the finiteness of a laser beam scanning 2D samples in measurements [3], we introduce the following image $\phi(x)$ with the fitting parameter R, which is the radius of the laser beam:

$$\phi(x) = \int_{-\infty}^{+\infty} \varphi(s) f(x-s)\,ds, \qquad f(x) = \exp(-x^2/R^2)/(R\sqrt{\pi}). \tag{20}$$

Images that are specified by Eqs. (20), (18) and (20), (19) are shown in the figure by solid lines in comparison with experimental data from [3] for (open circles) normal and (closed circles) anomalous states. This fitting yields the parameters $R \simeq 60$ μm, $x_o = 390$ μm, w = 240 μm, and $x_c \simeq 180$ μm, where x_o is the center of the distribution $\phi(x)$ in the figure.

Thus, Gauss images (20), (19), and (18) approximate the data [3] well, which testifies to the “stripped” structure of the Corbino disk in the quantum Hall regime. The central region is occupied by the system of incompressible strips whose internal structure is undefined because the radius R is nonzero. The periphery of the 2D system is occupied by normally conducting rings with the width

$$\Delta = w - x_c \simeq 60 \text{ μm}. \tag{21}$$

Unfortunately, Dietsche *et al.* [3] did not present intermediate measurements between the fields of 8.5 and 7.9 T, which would enable us to clarify the effect of the magnetic field on the position and structure of integer-factor strips. The magnitudes of the observed electric fields were also not presented. Nevertheless, value

(21) provides some indirect information on the magnitude of the contact energy W.

Condition (17) along with Eq. (2) determines the critical interval $2x_c$ for the Corbino disk, within which incompressible strips and their average description have meaning:

$$x_c = \xi_c/w, \quad \xi_c \simeq 1-\sqrt{\eta}, \quad \eta_o \ll \eta \ll 1,$$
$$\eta = \frac{a_{\min}^2}{w^2}\frac{W}{\hbar\omega_c}, \quad \eta_o = a_b^*/w. \tag{22}$$

Taking Eqs. (17) and (22) into account, we should take $W \simeq 1$ eV to ensure agreement between experimental and theoretical x_c values.

In summary, this study demonstrated that the width $2a$ of incompressible strips in the regularly nonuniform 2D electron systems cannot be arbitrarily small. The strip quality can be characterized by the ratio of the electron-density gradient $dn(x_l)/dx$ at the strip center to undisturbed value dn_o/dx. As the dimension $2a$ decreases, this ratio varies from an exponentially small value to almost unity. The characteristic transition value $2a_{\min}$ (17) is called the critical value. Possible experimental manifestations of existence of $a_{\min}$ are discussed by the example of the Corbino disk.

I am indebted to Prof. W. Dietsche for stimulating discussion and kindly placing electronic representation of the experimental data, which were reported in [3] and presented in the figure, at my disposal. I am also grateful to Prof. V. Gantmakher for helpful discussion of the results.

REFERENCES

1. D. Chklovskii, B. Shklovskii, and L. Glazman, Phys. Rev. B **46**, 4026 (1992).
2. D. B. Chklovskii, K. F. Matveev, and B. I. Shklovskii, Phys. Rev. B **47**, 12605 (1993).
3. W. Dietsche, K. von Klitzing, and K. Ploog, Surf. Sci. **361**, 289 (1996).
4. K. Lier and R. Gerhardts, Phys. Rev. B **50**, 7757 (1994).
5. A. MacDonald, T. Rice, and W. Brinkman, Phys. Rev. B **28**, 3648 (1983).
6. V. Shikin, Fiz. Nizk. Temp. **20**, 1158 (1994) [Low Temp. Phys. **20**, 910 (1994)].
7. V. Shikin, Pis'ma Zh. Éksp. Teor. Fiz. **71**, 95 (2000) [JETP Lett. **71**, 65 (2000)].

Translated by R. Tyapaev

JETP Letters, Vol. 73, No. 10, 2001, pp. 540–543. Translated from Pis'ma v Zhurnal Éksperimental'noĭ i Teoreticheskoĭ Fiziki, Vol. 73, No. 10, 2001, pp. 609–612.
Original Russian Text Copyright © 2001 by Eremin, Sakhratov, Savinkov, Dooglav, Mukhamedshin, Egorov.

Phase Diagram of $YBa_2Cu_3O_{7-y}$ at $T < T_c$ according to Transverse Nuclear Relaxation Data for Cu(2)

M. V. Eremin*, Yu. A. Sakhratov, A. V. Savinkov, A. V. Dooglav, I. R. Mukhamedshin, and A. V. Egorov
Kazan State University, Kremlevskaya ul. 18, Kazan, 420008 Russia
** e-mail:Mikhail.Eremin@ksu.ru*

Received April 16, 2001

Two peaks are observed at $T = 35$ and 47 K in the transverse relaxation rate for Cu(2) nuclei in $YBa_2Cu_3O_{7-y}$. A comparison of the relaxation rates for isotopes ^{63}Cu(2) and ^{65}Cu(2) at $T = 47$ K indicates the magnetic nature of relaxation. The enhancement of local magnetic field fluctuations perpendicular to CuO_2 planes at $T = 47$ K is associated with critical fluctuations of orbital currents. The peak at $T = 35$ K is attributed to the emergence of an inhomogeneous superconducting phase. The obtained experimental results and the available data from the literature made it possible to propose a qualitatively new phase diagram of the superconducting state. *© 2001 MAIK "Nauka/Interperiodica".*

PACS numbers: 74.25.Dw; 74.72.Bk; 76.60.Es

Anomalous behavior of the temperature dependence of the transverse magnetization relaxation rate for copper ions in CuO_2 planes of the superconducting compound $YBa_2Cu_3O_{7-y}$ was observed at the very outset of HTSC studies [1–5]. The transverse relaxation rate in superconducting samples with a nearly optimal doping level at $T = 35$ K increases quite sharply, indicating a phase transition [2, 6, 7]. Ohkawa [6] interpreted this transition as the second superconducting transition in the bilayer of $YBa_2Cu_3O_{7-y}$. Krämer and Mehring [7] attributed it to a transition of $YBa_2Cu_3O_{7-y}$ to a state with charge density waves (CDW). However, the authors of the latter publication [7] emphasized that such an interpretation requires further verification on samples with a different oxygen doping level. This was criticized recently by Grevin *et al.* [8], who reported the results of new measurements of the NQR line width of Cu(2) in slightly overdoped $YBa_2Cu_3O_{7-y}$ with $T_c = 89.5$ K. Grevin *et al.* emphasized the presence of a well-defined peak of the line width at 60 K and not at 35 K.

Our Cu(2) NQR measurements on few $YBa_2Cu_3O_{7-y}$ samples confirm the presence of the peak at $T = 35$ K in the transverse relaxation rate. The new results reported in this publication is that we observed one more transverse relaxation peak at $T = 47$ K. Moreover, it was found that this peak was also present in the data obtained by other authors [5, 9], but no proper attention was payed to it. In our opinion, the presence of two peaks on the temperature dependence of the transverse relaxation of Cu(2) nuclei in $YBa_2Cu_3O_{7-y}$ in some cases points to the existence of two phase transitions (and not one) below T_c.

The refined schematic phase diagram of phase coexistence in the optimal doping range of the superconducting state discussed earlier in [10] is presented in Fig. 1. In addition to the phase of spontaneous currents (or, which is the same, charge density waves with the imaginary order parameter (*id*-CDW)) proposed earlier [11–13], we assume the presence of at least one more phase in the superconducting state, in which Cooper pairs with a total nonzero quasimomentum appear; in other words, we presume the existence of a nonhomogeneous component of the superconducting phase of the *d* type (inhomogeneous SC). The possibility of the coexistence of several phases in underdoped cuprates is associated with Peierls-type instability of a quasi-two-dimensional system and was discussed in [11–13]. The scenario of the competition between *id*-CDW and *d*-SC successfully explains the nonmonotonic behavior of the effective gap near T_c [14]. Recently, this scenario was used for explaining the data on neutron scattering [15] and anomalous behavior of spin–lattice relaxation in superconducting cuprates at low temperatures [16].

Following [11, 12], we put into correspondence the dashed line in Fig. 1 to the boundary of the *id*-CDW state and the solid bell-shaped curve to the boundary of the *d*-type superconducting phase (*d*-SC). The behavior of the interface between the phases presented by the dashed line in Fig. 1 differs from that presented in [10] and is plotted in accordance with calculations [11, 12]. The presence of the interface denoted by the dot-and-dash curve is deduced by us from the transverse nuclear relaxation data which will be discussed below. In the region corresponding to a low doping level, the behavior of this interface is not determined in the present work and requires further investigation. The right edge of the boundary presented by the dot-and-dash curve is matched with the data considered in [10].

In our experiments, we used two $YBa_2Cu_3O_7$ (YBCO7) samples prepared by the solid-phase synthesis method. The critical temperatures of the samples (onset of transition) determined from the susceptibility measurements on a SQUID magnetometer were found to be 91.6 K (sample *1*) and 91.2 K (sample *2*). The NQR measurements for copper were made using a wide-range NQR/NMR coherent pulse spectrometer.

Transverse nuclear relaxation of Cu(2) in both samples was studied at temperatures varying from 77 to 4.2 K. The curves illustrating the decrease in transverse magnetization were described correctly by the function

$$M(\tau) = M_0 \exp\left(-\frac{(2\tau)^2}{2T_{2G}^2}\right)\exp\left(-\frac{2\tau}{T_{2L}}\right). \qquad (1)$$

The first exponent in this expression is the well-known Gaussian decrease in magnetization due to indirect spin–spin interactions of Cu(2) nuclei [17], while the second exponent takes into account the possibility of the emergence of an additional transverse relaxation channel. The Redfield contribution to transverse relaxation becomes noticeable only for $T > 60$–70 K and was disregarded. The transverse relaxation rates T_{2G}^{-1} and T_{2L}^{-1} obtained in accordance with Eq. (1) are presented in Fig. 2. It can be seen that below T_c, the Gaussian contribution T_{2G}^{-1} is independent of temperature, while the additional contribution T_{2L}^{-1} has a single peak at T = 35 K in sample *1* and two peaks at T = 35 and 47 K in sample *2*.

Nuclear spin–lattice relaxation of Cu(2) in both samples was studied at temperatures varying from 300 to 4.2 K. The curves for longitudinal magnetization recovery were described by the function

$$\frac{M(t) - M_0}{M_0} = \exp\left(-\frac{t}{T_1}\right)^N, \qquad (2)$$

where M_0 is the equilibrium magnetization, $M(t)$ is the transverse magnetization after time t following a saturating $\pi/2$ pulse, and parameter N characterizes the distribution of relaxation time for individual nuclear spins: N = 1 for a homogeneous system in which all spins relax at the same rate, and $N < 1$ for an inhomogeneous system in which the fluctuating fields responsible for relaxation are different for different spins.

The temperature dependence of the spin–lattice relaxation rate of Cu(2) is shown in Fig. 3. The rate of spin–lattice relaxation for both samples in the temperature range from 300 to 10 K displays the same temperature dependence and decreases very rapidly below T_c, which is associated with the emergence of a superconducting gap in the excitation spectrum of the superconductor. Below 35–40 K, the spin–lattice relaxation kinetics gradually becomes nonexponential ($N < 1$). No singularities in the spin–lattice relaxation rate is observed near T = 35 and 47 K.

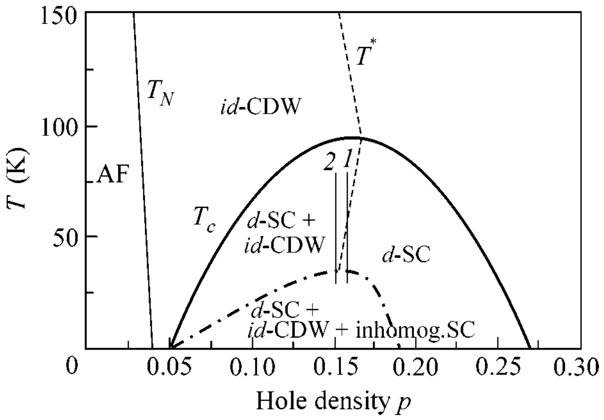

Fig. 1 Schematic phase diagram for $YBa_2Cu_3O_{7-y}$: p is the hole concentration per Cu(2) site like in the phase diagrams in [10].

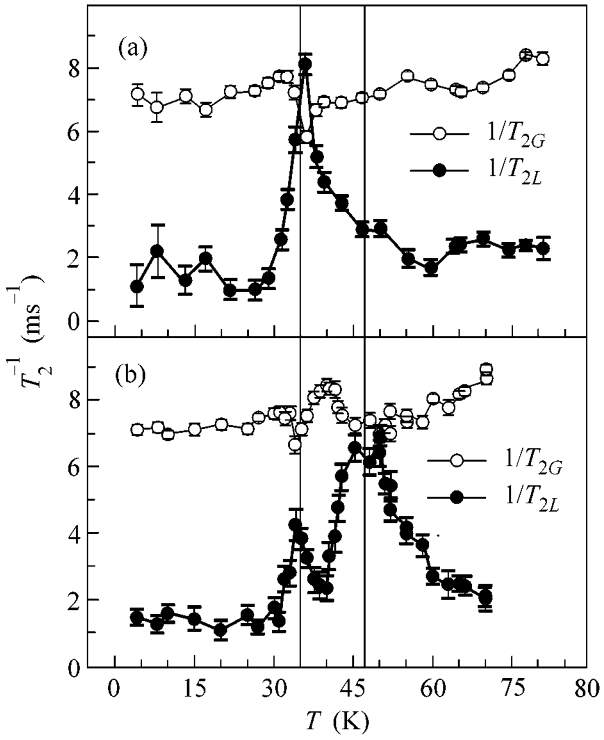

Fig. 2. Temperature dependence of the transverse relaxation rates T_{2G}^{-1} (dark circles) and T_{2L}^{-1} (light circles) for $^{63}Cu(2)$: (a) in sample *1*, (b) in sample *2*. Vertical lines correspond to 35 and 47 K.

It can be seen from Fig. 1 that, in the region of optimal doping, the interfaces are intersected twice as the temperature decreases along line *1* in the superconducting state. Since the temperature corresponding to the interface between two phases and depicted by the

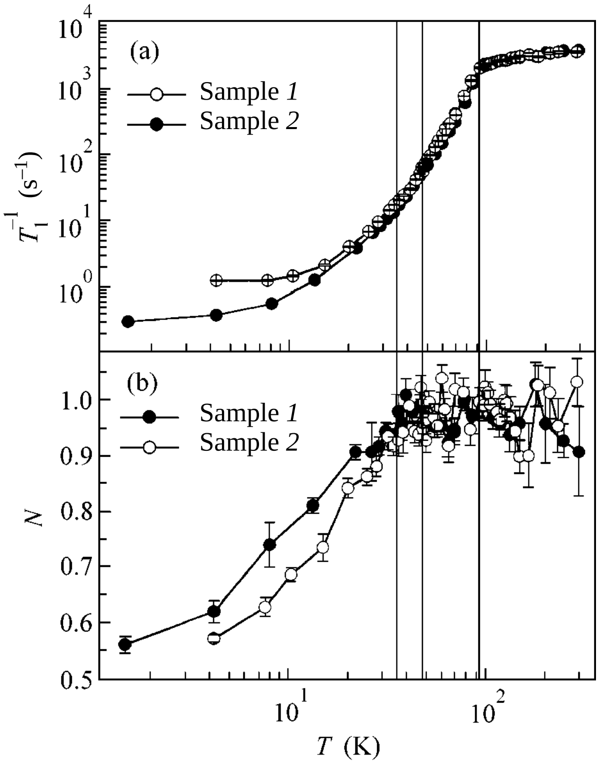

Fig. 3. Temperature dependence of (a) spin–lattice relaxation rate for ^{63}Cu(2) and (b) parameter N (see text) in sample *1* (dark circles) and *2* (light circles). Vertical lines correspond to 35, 47, and 91.4 K.

dashed line strongly depends on the doping level, only one intersection with the interface remains for a doping level close to optimal (e.g., for the decrease in temperature along line *2*), which can be naturally attributed to the peak of T_2^{-1} at $T \approx 35$ K.

It is well known that the longitudinal relaxation of the nuclear magnetic moments may be induced by fields fluctuating at the NMR (NQR) frequency and directed at right angles to the quantization axis coinciding with the direction of the electric field gradient at a nucleus in the case of NQR, while the transverse relaxation is associated with the fields fluctuating at a low frequency and directed along the quantization axis. Since the nuclei of ^{63}Cu and ^{65}Cu isotopes have different gyromagnetic ratios and quadrupole moments ($^{63}\gamma/^{65}\gamma = 0.933$ and $^{63}Q/^{65}Q = 1.081$), the measurements made at different isotopes make it possible to determine the factor causing the relaxation (magnetic field fluctuations or the fluctuations of the electric field gradient at a nucleus). Furthermore, if transverse relaxation is caused by the interaction between identical nuclear spins, its rate for the ^{63}Cu isotope must be 1.3 times higher than for ^{65}Cu [17, 18] due to the lower concentration (natural abundance) of the latter isotope.

The orbital currents circulating in CuO$_2$ planes induce fluctuating magnetic fields at Cu(2) nuclei, which are directed along the *c* axis of the crystal. Since the electric field gradient at Cu(2) nuclei is also directed along the *c* axis, the changes in the phases of spontaneous currents lead to the critical acceleration mainly of the transverse nuclear magnetic relaxation and weakly affect the spin–lattice relaxation. This is in good agreement with the results of experiments (Fig. 3a). Our comparative analysis of the relative relaxation rates at ^{63}Cu and ^{65}Cu isotopes confirms the magnetic origin of the additional transverse relaxation channel (second exponential in formula (1)) emerging at $T = 47$ K and indicates that it is not associated with the interaction between identical nuclear spins: ${}^{63}T_{2L}^{-1}/{}^{65}T_{2L}^{-1} = 0.89 \approx ({}^{63}\gamma/{}^{65}\gamma)^2$.

We could not establish reliably the type of the additional relaxation channel emerging at $T = 35$ K in view of insufficient long-term stabilization of temperature, which did not permit us to “hold on” at the sharp transverse relaxation peak during signal accumulation to an admissible accuracy. According to Krämer and Mehring [7], the additional transverse relaxation in underdoped YBCO7 at 35 K is caused by electric field gradient fluctuations at Cu(2) nuclei, which is quite explainable if we assume that the phase of spontaneous currents remains virtually unchanged upon a transition through the interface along line *2* in Fig. 1, but below 35 K, an inhomogeneous superconducting phase with a spatially modulated charge (*U* phase in the terminology adopted in [11]) is formed. The presence of the phase of spontaneous spin currents, which is possible according to estimates [16], cannot be ruled out either. The phase transition to an inhomogeneous (incommensurate) state is supported by the variation in the form of the time dependence of the spin echo signal recovery observed by us (Fig. 3b): at a temperature below 30–40 K, parameter N in formula (2) becomes smaller than unity; i.e., the signal recovery curve deviates from an exponential. In this connection, it is appropriate to recall Figs. 4 and 5 from [19], in which a qualitatively different temperature behavior (as compared to that at $T > 35$ K) of the Gaussian rate of the spin–spin relaxation of Cu(2) is detected in YBa$_2$Cu$_3$O$_{6.98}$ and LaBa$_2$Cu$_3$O$_{6.93}$ at $T < 30$ K, which also indicates a phase transition at $T \approx 30$ K.

The strong dependence of the position of the second peak in T_2^{-1} on the oxygen deficiency in the optimal doping region (see table) fits well into the pattern of a strong dependence of the temperature corresponding to the disappearance of the phase of spontaneous currents on the doping level. The slope of the interface between SC and the mixed (SC + *id*-CDW) phases to the left in Fig. 1 indicates a tendency to the expulsion of the phase of spontaneous currents from the superconducting state. This tendency was predicted in [11] on the basis of the solution of integral equations.

Position of peaks on the transverse relaxation rate of Cu(2) below T_c

Substance	T_c, K	Peak 1, K	Peak 2, K	Reference
$YBa_2Cu_3O_{6.98}$	92	35	52	[5]
$YBa_2Cu_3O_{7-y}$	90	35		[7]
$YBa_2Cu_3O_{7-y}$	93	35		[3]
$YBa_2Cu_3O_{6.95}$	≈91	35	50	[9]
$YBa_2Cu_3O_{6.925}$	≈91	35		
$YBa_2Cu_3O_{7-y}$	91.6	35	–	Our results
	91.2	35	47	

In conclusion, let us give one more argument in favor of the inhomogeneous superconducting phase. The chain structures of YBCO7 display a behavior typical of systems with CDW even at $T > T_c$ (see, for example, [20]). Hybridization of chain and plane bands "facilitates" the formation of the inhomogeneous superconducting phase in the plane also. In this connection, it also becomes clear why the compound $La_{2-x}Sr_xCuO_4$ displays no anomalies in the transverse relaxation rate of copper nuclei in the region $T \sim 30$ K [3].

This work was supported by the Russian Federal Program "Superconductivity," project no. 98014-1.

REFERENCES

1. O. N. Bakharev, R. Sh. Zhdanov, A. V. Egorov, *et al.*, Pis'ma Zh. Éksp. Teor. Fiz. **47**, 383 (1988) [JETP Lett. **47**, 458 (1988)].
2. A. V. Bondar', S. M. Ryabchenko, Yu. V. Fedotov, *et al.*, Pis'ma Zh. Éksp. Teor. Fiz. **50**, 133 (1989) [JETP Lett. **50**, 146 (1989)].
3. K. Kumagai, Y. Nakamichi, Y. Nakamura, *et al.*, J. Phys. Soc. Jpn. **59**, 2336 (1990).
4. M. Tei, H. Takai, K. Mizoguchi, *et al.*, Z. Naturforsch. A **45**, 429 (1990); M. Tei, H. Takai, K. Mizoguchi, *et al.*, Solid State Commun. **74**, 1117 (1990).
5. Y. Itoh, H. Yasuoka, and Y. Ueda, J. Phys. Soc. Jpn. **59**, 3463 (1990).
6. F. J. Ohkawa, J. Phys. Soc. Jpn. **61**, 639 (1992).
7. S. Krämer and M. Mehring, Phys. Rev. Lett. **83**, 396 (1999); Phys. Rev. Lett. **84**, 1637 (2000).
8. B. Grevin, Y. Berthier, and G. Collin, Phys. Rev. Lett. **84**, 1636 (2000).
9. M. Tei, K. Mizoguchi, and K. Kume, in *The Physics and Chemistry of Oxide Superconductors*, Ed. by Y. Iye and H. Yasuoka (Springer-Verlag, Berlin, 1992); Springer Proc. Phys. **60**, 369 (1992).
10. J. L. Tallon and J. W. Loram, cond-mat/0005063.
11. M. V. Eremin and I. A. Larionov, Pis'ma Zh. Éksp. Teor. Fiz. **68**, 583 (1998) [JETP Lett. **68**, 611 (1998)].
12. E. Cappelluti and R. Zeycher, Phys. Rev. B **59**, 6475 (1999).
13. S. Chakravarty, R. B. Laughlin, D. K. Morr, *et al.*, Phys. Rev. B **63**, 094503 (2001).
14. T. Ekino, Y. Sezaki, and H. Fujii, Phys. Rev. B **60**, 6916 (1999); T. Ekino, S. Hashimoto, and H. Fujii, J. Phys. Chem. Solids **62**, 149 (2001).
15. S. Tewari, H.-Y. Kee, Ch. Nayak, *et al.*, cond-mat/0101027.
16. M. Eremin and A. Rigamonti, cond-mat/0103282.
17. C. H. Pennington, D. J. Durand, C. P. Slichter, *et al.*, Phys. Rev. B **39**, 274 (1989); C. H. Pennington and C. P. Slichter, Phys. Rev. Lett. **66**, 381 (1991).
18. A. Abragam, *The Principles of Nuclear Magnetism* (Clarendon Press, Oxford, 1962; Inostrannaya Literatura, Moscow, 1963), p. 125.
19. Y. Itoh, K. Yoshimura, T. Ohomura, *et al.*, J. Phys. Soc. Jpn. **63**, 1455 (1994).
20. B. Grevin, Y. Berthier, and G. Collin, Phys. Rev. Lett. **85**, 1310 (2000).

Translated by N. Wadhwa

JETP Letters, Vol. 73, No. 10, 2001, pp. 544–548. Translated from Pis'ma v Zhurnal Éksperimental'noĭ i Teoreticheskoĭ Fiziki, Vol. 73, No. 10, 2001, pp. 613–617.
Original Russian Text Copyright © 2001 by Zubarev.

Formation of Conic Cusps at the Surface of Liquid Metal in Electric Field

N. M. Zubarev
Institute of Electrophysics, Ural Division, Russian Academy of Sciences, Yekaterinburg, 620016 Russia
e-mail: nick@ami.uran.ru

Received March 14, 2001; in final form, April 16, 2001

The formation dynamics is studied for a singular profile of a surface of an ideal conducting fluid in an electric field. Self-similar solutions of electrohydrodynamic equations describing the fundamental process of formation of surface conic cusps with angles close to the Taylor cone angle 98.6° are obtained. The behavior of physical quantities (field strength, fluid velocity, surface curvature) near the singularity is established. *© 2001 MAIK “Nauka/Interperiodica”.*

PACS numbers: 47.65.+a; 47.20.Ma

It is known [1, 2] that a flat boundary of liquid metal becomes unstable in a strong electric field. The development of instability results in conic cusp singularities, from which the strengthened field initiates emission processes [3–6]. The description of these processes is a key problem of the electrohydrodynamics of conducting fluids with free surfaces; interest in this problem is largely caused by the practical use of liquid-metal sources of charged particles. The progress in this field is associated with Taylor's work [7], where it was demonstrated that the surface electrostatic pressure P_E for a cone with angle 98.6° depends on the distance from its axis as r^{-1} and, hence, can be counterbalanced by the surface pressure $P_S \sim r^{-1}$. Since the force balance is violated at the cone apex, Taylor's solution cannot be treated as the exact solution of the problem of equilibrium configuration of a charged surface of conducting fluid and only represents the possible asymptotic form at $r \longrightarrow \infty$. At the same time, it turned out that Taylor's solution nicely describes the experimentally observed surface shape before the instant of singularity formation. It was pointed out in [3–6] that the angle of incipient conic formations is close to the Taylor cone angle.

What is the reason for such a coincidence? One may assume that the mechanism for the formation of conic cusps with an angle of 98.6° during a finite time is not directly associated with the static Taylor model. A high reproducibility of experimental results and a weak dependence of fluid behavior at the final instability stages on the geometry of the system suggest that the behavior of fluid near the singularity has a self-similar character.

Let us check the validity of this hypothesis. Consider the potential motion of an ideal fluid occupying the region bounded by free surface $z = \eta(x, y, t)$. We will assume that the vector of an external electric field is directed along the z axis and equals E. The velocity potential Φ of fluid and the electric-field potential φ satisfy the Laplace equations

$$\nabla^2\Phi = 0, \quad \nabla^2\varphi = 0$$

with the following boundary conditions:

$$\begin{gathered}
\Phi_t + \frac{|\nabla\Phi|^2}{2} = \frac{|\nabla\varphi|^2}{8\pi\rho} + \frac{\alpha}{\rho}\nabla_\perp\frac{\nabla_\perp\eta}{\sqrt{1+(\nabla_\perp\eta)^2}}, \\
z = \eta(x, y, t), \\
\eta_t = \Phi_z - \nabla_\perp\eta\nabla_\perp\Phi, \quad z = \eta(x, y, t), \\
\varphi = 0, \quad z = \eta(x, y, t), \\
|\nabla\Phi| \longrightarrow 0, \quad z \longrightarrow -\infty, \\
\varphi \longrightarrow -Ez, \quad z \longrightarrow \infty,
\end{gathered} \tag{1}$$

where α is the surface tension coefficient and ρ is the density of a medium.

We are interested in the dynamics of formation of a singular profile for a conducting fluid. It is natural to assume that the electric field near the cusp appreciably exceeds the external field; i.e., $|\nabla\varphi| \gg E$. In this case, the interface evolution is fully determined by the intrinsic field, which decreases with distance from the singularity. One can thus use the condition

$$|\nabla\varphi| \longrightarrow 0, \quad z \longrightarrow \infty \tag{2}$$

instead of the field uniformity condition (1). This agrees with the assumption about the universal behavior of a fluid in the formation of a singular surface profile, because it allows the fluid motion near the singular point to be analyzed without regard for the particular geometry of the problem. The applicability of condition (2) will be discussed below in more detail after establishing some regularities for the dynamics of a conducting fluid near the singularity. Note that the possibility of secondary Taylor cones nucleating at the already formed cones counts in favor of the universal mechanism of formation of conic cusps [4]. It is clear from this example that fluid "forgets" the boundary conditions at infinity at the stage of collapse.

Let us consider the most important case of the axially symmetric perturbation of the surface. Taking into account that, after substitutions

$$\varphi \longrightarrow \varphi 4\pi\alpha E^{-1}, \quad \Phi \longrightarrow \Phi 2\pi^{\frac{1}{2}}\rho^{-\frac{1}{2}}\alpha E^{-1},$$

$$\eta \longrightarrow \eta 4\pi\alpha E^{-2}, \quad r \longrightarrow r 4\pi\alpha E^{-2},$$

$$z \longrightarrow z 4\pi\alpha E^{-2}, \quad t \longrightarrow t 8\pi^{\frac{3}{2}}\rho^{\frac{1}{2}}\alpha E^{-3},$$

where $r = \sqrt{x^2 + y^2}$, the equations of motion become dimensionless and do not contain any physical characteristics, one obtains

$$\Phi_{rr} + r^{-1}\Phi_r + \Phi_{zz} = 0, \quad z < \eta(r, t), \tag{3}$$

$$\varphi_{rr} + r^{-1}\varphi_r + \varphi_{zz} = 0, \quad z > \eta(r, t), \tag{4}$$

$$\Phi_t + \frac{\Phi_r^2 + \Phi_z^2}{2} = \frac{\varphi_r^2 + \varphi_z^2}{2} + \frac{1}{\sqrt{1 + \eta_r^2}}\left(\frac{\eta_{rr}}{1 + \eta_r^2} + \frac{\eta_r}{r}\right), \quad z = \eta(r, t), \tag{5}$$

$$\eta_t = \Phi_z - \eta_r\Phi_r, \quad z = \eta(r, t), \tag{6}$$

$$\varphi = 0, \quad z = \eta(r, t), \tag{7}$$

$$\Phi_r^2 + \Phi_z^2 \longrightarrow 0, \quad \varphi_r^2 + \varphi_z^2 \longrightarrow 0, \quad r^2 + z^2 \longrightarrow \infty, \tag{8}$$

$$\Phi_r = 0, \quad \varphi_r = 0, \quad \eta_r = 0, \quad r = 0. \tag{9}$$

These equations allow the only self-similar substitution

$$\Phi(x, y, z, t) = \tilde{\Phi}(\tilde{r}, \tilde{z})\tau^{1/3}, \tag{10}$$

$$\varphi(x, y, z, t) = \tilde{\varphi}(\tilde{r}, \tilde{z})\tau^{1/3}, \tag{11}$$

$$\eta(x, y, t) = \tilde{\eta}(\tilde{r})\tau^{2/3}, \tag{12}$$

$$r = \tilde{r}\tau^{2/3}, \tag{13}$$

$$z = \tilde{z}\tau^{2/3}, \tag{14}$$

where $\tau = t_c - t$ and t_c is the collapse time. This substitution occurs due to the fact that Eqs. (3)–(9) are invariant about dilatations

$$\Phi \longrightarrow \Phi c, \quad \varphi \longrightarrow \varphi c, \quad \eta \longrightarrow \eta c^2,$$

$$r \longrightarrow rc^2, \quad z \longrightarrow zc^2, \quad t \longrightarrow tc^3;$$

i.e., it occurs, in fact, from dimensional considerations (c is an arbitrary constant). Note that the initial electrohydrodynamic equations with condition (1) do not permit one to introduce any self-similar variables.

Substituting Eqs. (10)–(14) in Eqs. (3)–(9), one finds that the functions $\tilde{\Phi}$, $\tilde{\varphi}$, and $\tilde{\eta}$ obey the following set of partial differential equations:

$$\tilde{\Phi}_{\tilde{r}\tilde{r}} + \tilde{r}^{-1}\tilde{\Phi}_{\tilde{r}} + \tilde{\Phi}_{\tilde{z}\tilde{z}} = 0, \quad \tilde{z} < \tilde{\eta}(\tilde{r}), \tag{15}$$

$$\tilde{\varphi}_{\tilde{r}\tilde{r}} + \tilde{r}^{-1}\tilde{\varphi}_{\tilde{r}} + \tilde{\varphi}_{\tilde{z}\tilde{z}} = 0, \quad \tilde{z} > \tilde{\eta}(\tilde{r}), \tag{16}$$

$$\frac{2\tilde{\Phi}_{\tilde{r}}\tilde{r} + 2\tilde{\Phi}_{\tilde{z}}\tilde{\eta} - \tilde{\Phi}}{3} + \frac{\tilde{\Phi}_{\tilde{r}}^2 + \tilde{\Phi}_{\tilde{z}}^2}{2} = \frac{\tilde{\varphi}_{\tilde{r}}^2 + \tilde{\varphi}_{\tilde{z}}^2}{2} + \frac{1}{\sqrt{1 + \tilde{\eta}_{\tilde{r}}^2}}\left(\frac{\tilde{\eta}_{\tilde{r}\tilde{r}}}{1 + \tilde{\eta}_{\tilde{r}}^2} + \frac{\tilde{\eta}_{\tilde{r}}}{\tilde{r}}\right), \quad \tilde{z} = \tilde{\eta}(\tilde{r}), \tag{17}$$

$$2\tilde{\eta}_{\tilde{r}}\tilde{r} - 2\tilde{\eta} = 3\tilde{\Phi}_{\tilde{z}} - 3\tilde{\eta}_{\tilde{r}}\tilde{\Phi}_{\tilde{r}}, \quad \tilde{z} = \tilde{\eta}(\tilde{r}), \tag{18}$$

$$\tilde{\varphi} = 0, \quad \tilde{z} = \tilde{\eta}(\tilde{r}), \tag{19}$$

$$\tilde{\Phi}_{\tilde{r}}^2 + \tilde{\Phi}_{\tilde{z}}^2 \longrightarrow 0, \quad \tilde{\varphi}_{\tilde{r}}^2 + \tilde{\varphi}_{\tilde{z}}^2 \longrightarrow 0, \quad \tilde{r}^2 + \tilde{z}^2 \longrightarrow \infty, \tag{20}$$

$$\tilde{\Phi}_{\tilde{r}} = 0, \quad \tilde{\varphi}_{\tilde{r}} = 0, \quad \tilde{r} = 0. \tag{21}$$

For self-similar solutions (10)–(14), the surface profile forms first at the periphery and then extends to the center $r = z = 0$ (the scale decreases as $\tau^{2/3}$). This implies that the formation of conic cusps at $t = t_c$ is described by those solutions to the set of Eqs. (15)–(21) which provide conic asymptotic shape of the surface. In such a situation, the presence of asymptotic solutions for which $\tilde{\eta} \sim \tilde{r}$ at $\tilde{r} \longrightarrow \infty$ is the necessary condition for the validity of our assumption about the self-similar nature of conic formations.

Analysis of Eqs. (15)–(21) in the limit $R = \sqrt{\tilde{r}^2 + \tilde{z}^2} \longrightarrow \infty$ showed that they have an asymptotic solution of the form

$$\tilde{\varphi}(\tilde{r}, \tilde{z}) = p^{-1}[2R(s_0 - s)]^{1/2}P_{1/2}(\cos\theta), \tag{22}$$

$$\tilde{\Phi}(\tilde{r}, \tilde{z}) = sR^{-1}, \tag{23}$$

$$\tilde{\eta}(\tilde{r}) = -s_0\tilde{r},$$

$$\begin{gathered} P_{1/2}(\cos\theta_0) = 0, \\ p = [dP_{1/2}(\cos\theta)/d\theta]_{\theta = \theta_0}, \end{gathered} \tag{24}$$

$$s_0 = -\cot\theta_0,$$

where $\theta = \arctan(\tilde{r}/\tilde{z})$ is the polar distance in spherical coordinates, $P_{1/2}$ is the Legendre polynomial of order 1/2, and s is a constant satisfying inequality $0 < s < s_0$. This solution describes a conic surface with an angle of $2\pi - 2\theta_0$ that is equal to approximately 98.6°, i.e., to the Taylor cone angle. According to Eq. (23), the fluid motion is spherically symmetric, and fluid moves to the sink point $R = 0$ along the tangent to the surface (24). Since the self-similar solution assumes its asymptotic form at $\tau \longrightarrow 0$, a conic cusp with Taylor angle forms at time t_c, and Eqs. (22)–(24) are the exact analytic solution of the problem. The electric field at the cusp increases as $\tau^{-1/3}$, the cusp growth velocity increases as $\tau^{-1/3}$, and the cusp curvature increases as $\tau^{-2/3}$; i.e., these quantities become infinite during a finite time. At an appreciable distance from the singularity, the field strength does not change, and the velocity of fluid linearly decreases with time and becomes zero at $t = t_c$. The latter fact allows one to explain qualitatively the mechanism of transition to the stationary regime occurring for liquid-metal sources after the initiation of field ion evaporation from the cusp (stationary emitter models were developed in [8, 9]).

This analysis is only valid on the condition that the asymptotic solutions to the set of partial differential Eqs. (15)–(21) have the form of Eqs. (22)–(24). To prove this statement, one should construct the asymptotic expansion for the solutions at $R \longrightarrow \infty$ with leading terms given by Eqs. (22)–(24). Let us seek this expansion in the form

$$\tilde{\varphi}(\tilde{r}, \tilde{z}) = \sum_{n=0}^{\infty} a_n \frac{\partial^{3n}}{\partial \tilde{z}^{3n}}[R^{1/2} P_{1/2}(\cos\theta)], \tag{25}$$

$$\tilde{\Phi}(\tilde{r}, \tilde{z}) = \sum_{n=0}^{\infty} b_n \frac{\partial^{3n}}{\partial \tilde{z}^{3n}}[R^{-1}], \tag{26}$$

$$\tilde{\eta}(\tilde{r}) = \sum_{n=0}^{\infty} c_n \tilde{r}^{1-3n}, \tag{27}$$

where it is taken into account that the derivative of a harmonic function of any order with respect to $\tilde{z}$ is also a harmonic function. The zero-order coefficients are determined by Eqs. (22)–(24),

$$a_0 = p^{-1}[2(s_0 - s)]^{1/2}, \quad b_0 = s, \quad c_0 = s_0.$$

It turns out that, to the first order, the surface is conic:

$$a_1 = 0, \quad b_1 = -\frac{s^2(1+s_0^2)^{3/2}}{18 s_0(3 - 2s_0^2)}, \quad c_1 = 0.$$

The correction to Eq. (24) for the surface shape appears in the next order. One finds from kinematic boundary condition (18) that

$$c_2 = -\frac{s^2(4s_0^2 - 1)}{8s_0^2(1+s_0^2)^2(3-2s_0^2)}.$$

The coefficients a_2 and b_2 can be determined from Eq. (19) and, correspondingly, Eq. (17), where one should use the linear order of perturbation theory for small deviation of the surface from the cone. In turn, the coefficient c_3 is found from Eq. (18), where one should take into account the quadratic nonlinearity, etc. Thus, the expansion coefficients are uniquely determined by the zero-order coefficients, i.e., by the parameter s of the problem, confirming the existence of solutions with the desired asymptotic form for the equations of motion. Note that, if one sets $s = 0$ and, hence, $\Phi = 0$, then Eqs. (15)–(21) coincide with the Taylor equations in the problem of equilibrium configuration of a charged liquid-metal surface. However, one fails to construct asymptotic expansion (25)–(27) in this case.

Further, the solutions given by expansions (25)–(27) adequately describe the experimental data if the condition $\tilde{\eta} < -s_0\tilde{r}$ is satisfied, i.e., if the fluid surface is positioned above the asymptotic cone (see figure). Otherwise, the surface velocity would be directed in opposition to the z axis. Let us check how this condition is fulfilled in the limit of large r. It follows from the expansion obtained above for the surface shape that it deviates from the conic shape in the direction specified by the sign of the c_2 coefficient. In our case, $c_2 < 0$ ($c_2 > 0$ for cone angles smaller than 78.5° and larger than 126.9°), so that the amplitude of surface perturbation should increase. Indeed, the evolution of the fluid boundary away from the singularity is determined by the leading terms of the expansion in small τ value,

$$\eta(r, t) = -s_0 r - |c_2|\tau^4 r^{-5},$$

from whence it follows that, when forming a conic cusp, the fluid moves upwards, as is expected from physical considerations.

Let us now consider the surface geometry for small $\tilde{r}$, where expansion (27) diverges. For the function $\tilde{\eta}$ to satisfy condition (21), the surface near the cone apex must be "rounded off" (figure). Let us estimate the distance $|\tilde{\eta}(0)|$ from the cone apex to the fluid surface. Multiplying kinematic boundary condition (18) by $2\pi\tilde{r}/3$ and integrating it over $\tilde{r}$, one obtains after simple mathematics

$$2V = \int_S \partial_n \tilde{\Phi}\, dS,$$

where S stands for the fluid surface $\tilde{z} = \tilde{\eta}(\tilde{r})$, V is the volume of a region bounded from above by the conic surface $\tilde{z} = -s_0\tilde{r}$ and from below by the S surface, and ∂_n denotes the derivative along the normal to S. The integral on the right-hand side of this expression is equal to the fluid velocity flux through the surface. Since the function $\tilde{\Phi}$ is harmonic, the vector-field flux $\nabla\tilde{\Phi}$ through any closed surface is zero. This fact allows the flux through the surface S to be determined using the asymptotic form of velocity potential at $R \longrightarrow \infty$. Taking into account that the fluid flows into a solid angle $2\pi(1 + \cos\theta_0)$ at infinity, one has from Eq. (23)

$$\int_S \partial_n\tilde{\Phi}dS = 2\pi s(1 + \cos\theta_0)$$

and, hence, $V = \pi s(1 + \cos\theta_0)$. Notice that the volume of a region bounded by the conic surface $\tilde{z} = -s_0\tilde{r}$ and the plane $\tilde{z} = -h$ (a circular right cone of height h) is equal to V at

$$h = h(s) = [3ss_0^2(1 + \cos\theta_0)]^{1/3}.$$

Clearly, if the volume V is fixed and the conditions $\tilde{\eta}(\tilde{r}) + s_0\tilde{r} < 0$ and $\tilde{\eta}_{\tilde{r}}(\tilde{r}) \le 0$ are fulfilled for any $\tilde{r}$, the quantity $|\tilde{\eta}(0)|$ cannot exceed the cone height. That is, the inequality

$$|\tilde{\eta}(0)| \le h(s)$$

connecting the characteristic spatial scale at small R with the asymptotic parameter s is satisfied. Since the most probable value of $h(s)$ corresponds to the maximum allowable value s_0 of the s constant, the following estimate is also valid:

$$|\tilde{\eta}(0)| \le h(s_0) = s_0(3 + 3\cos\theta_0)^{1/3},$$

which does not involves the free parameter s.

Let us return to the question of the applicability of approximation (3)–(9) to the initial equations of motion. As was pointed out above, condition (2) can be used instead of Eq. (1) only if the external electric field is weaker than the intrinsic cusp field. This implies that the inequality $\varphi_r^2 + \varphi_z^2 \gg 1$ must be fulfilled. After the transition to the self-similar variables, it is recast as

$$\tilde{\varphi}_{\tilde{r}}^2 + \tilde{\varphi}_{\tilde{z}}^2 \gg \tau^{2/3}.$$

It is clear that for small τ (i.e., immediately before the collapse) this condition is fulfilled near the singularity in a natural way. Because one can write $|\nabla\varphi| \sim (r^2 + z^2)^{-1/4}$ at small τ, one has $|\nabla\varphi| \gg 1$ in a rather close vicinity of the singularity. In this case, R_0 and τ_0 values exist for which model (3)–(9) with $0 \le r^2 + z^2 < R_0^2$ and $0 \le \tau < \tau_0$ adequately describes the strongly nonlinear stages of electrohydrodynamic instability development for the free surface of a conducting fluid in an external electric field. At $r^2 + z^2 > R_0^2$, the role of nonlinear processes is rather insignificant; the condition for field uniformity at infinity (1) should be used together with the corresponding conditions in the limit $r \longrightarrow \infty$ and, in particular, with the condition for spatial localization of surface perturbation: $\eta \longrightarrow 0$ at $r \longrightarrow \infty$. In this region, the evolution of fluid surface is described by perturbation theory for small surface slope; this procedure was implemented, e.g., in [10, 11].

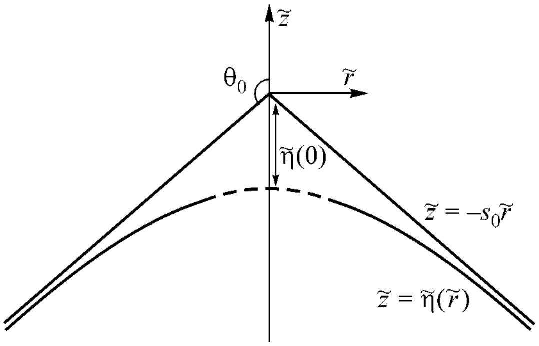

Schematic drawing of a surface of conducting fluid $\tilde{z} = \tilde{\eta}(\tilde{r})$ corresponding to the self-similar solutions of the equations of motion.

In conclusion, let us discuss the possibility to form stronger singularities—cuspidal points. It is known [12] that the field mainly increases as r^{-1} upon approaching the apex of a thin point and, hence, the electrostatic pressure P_E increases as r^{-2}. Since the surface pressure changes as $P_S \sim r^{-1}$, $P_E \gg P_S$ near the singularity, and the capillary effects can be ignored. It was shown in [10] that in the absence of surface tension weak root singularities $\eta \sim r^{3/2}$ form, for which the curvature is infinite, while the surface itself remains smooth. Therefore, when assuming that the cuspidal points may appear, one arrives at a contradiction. This gives grounds to assume that conic singularities are precisely those which are the generic singular solutions of the electrohydrodynamic equations, so that the behavior of a charged liquid-metal surface with cusps is described by self-similar solutions (10)–(21).

Note also that the results of this work can be extended to dielectric fluids, in which the conic cusps with angles depending on the dielectric constant can form in an electric field [13]. In addition, the approach developed in this work can be applied to the description of the evolution of dimples sharpening in a finite time at a liquid helium surface (see, e.g., experimental work [14]). In my preceding work [15] devoted to the construction of exact analytic solutions to the equations of motion for liquid helium in the presence of weak capillary effects, I proved that cuspidal points $\eta \sim |x|^{2/3}$ appear at the surface in planar geometry. The question of the singularity type for axial symmetry has not been considered so far.

REFERENCES

1. L. Tonks, Phys. Rev. **48**, 562 (1935).
2. Ya. I. Frenkel', Zh. Éksp. Teor. Fiz. **6**, 347 (1936).
3. A. V. Batrakov, S. A. Popov, and D. I. Proskurovskiĭ, Pis'ma Zh. Tekh. Fiz. **19** (19), 66 (1993) [Tech. Phys. Lett. **19**, 627 (1993)].
4. W. Driesel, Ch. Dietzsch, H. Niedrig, and B. Praprotnic, Ultramicroscopy **57**, 45 (1995).
5. W. Driesel, Ch. Dietzsch, and R. Mühle, J. Vac. Sci. Technol. B **14**, 3367 (1996).
6. A. V. Batrakov, Candidate's Dissertation in Mathematical Physics (Inst. Sil'notochn. Élektron. Sib. Otd. Ross. Akad. Nauk, Tomsk, 1997).
7. G. Taylor, Proc. R. Soc. London, Ser. A **280**, 383 (1964).
8. D. R. Kingham and L. W. Swanson, Appl. Phys. A **A34**, 123 (1984).
9. R. G. Forbes and N. N. Ljepojevic, Surf. Sci. **246**, 113 (1991).
10. N. M. Zubarev, Zh. Éksp. Teor. Fiz. **114**, 2043 (1998) [JETP **87**, 1110 (1998)].
11. N. M. Zubarev and O. V. Zubareva, Zh. Tekh. Fiz. **71** (7), 21 (2001) [Tech. Phys. **46**, 806 (2001)].
12. L. D. Landau and E. M. Lifshitz, *Course of Theoretical Physics*, Vol. 8: *Electrodynamics of Continuous Media* (Nauka, Moscow, 1982; Pergamon, New York, 1984).
13. A. Ramos and A. Castellanos, Phys. Lett. A **184**, 268 (1994).
14. A. P. Volodin, M. S. Khaĭkin, and V. S. Édel'man, Pis'ma Zh. Éksp. Teor. Fiz. **26**, 707 (1977) [JETP Lett. **26**, 543 (1977)].
15. N. M. Zubarev, Pis'ma Zh. Éksp. Teor. Fiz. **71**, 534 (2000) [JETP Lett. **71**, 367 (2000)].

Translated by V. Sakun

JETP Letters, Vol. 73, No. 10, 2001, pp. 549–551. Translated from Pis'ma v Zhurnal Éksperimental'noĭ i Teoreticheskoĭ Fiziki, Vol. 73, No. 10, 2001, pp. 618–620.
Original Russian Text Copyright © 2001 by Lykov.

Generation of Coherent Electromagnetic Radiation by Superconducting Films at Liquid-Nitrogen Temperatures

A. N. Lykov
Lebedev Physical Institute, Russian Academy of Sciences, Moscow, 117924 Russia
e-mail: lykov@sci.lpi.msk.su

Received March 16, 2001; in final form, April 16, 2001

Generation of coherent electromagnetic radiation by $GdBa_2Cu_3O_{7-x}$ superconducting films is observed in the frequency range 1–10 MHz at the temperature of boiling liquid nitrogen. The generation is caused by the feedback synchronization of the jumps of Abrikosov vortices produced by a low-frequency external magnetic field. This offers new possibilities for the application of high-T_c superconductors in superconducting electronics. *© 2001 MAIK "Nauka/Interperiodica".*

PACS numbers: 74.76.Bz; 74.60.Ge; 85.25.-j

One of the most interesting problems of today's superconductivity is the development of a generator of electromagnetic radiation. The possibility of such a generation was first revealed by Josephson [1]. However, the attempts to use Josephson junctions as generators of radiation encounter two difficulties: the low radiation power obtained from a Josephson junction and its small output impedance, which can hardly be matched with an external electromagnetic system. Although some success was achieved with the use of arrays of Josephson junctions [2], as well as Josephson junctions in the flux flow regime [3], the aforementioned difficulties still remain to be overcome. The discovery of high-T_c superconductors offered a fundamental possibility for the development of superconducting devices operating at liquid-nitrogen temperatures, which has attracted additional interest to this direction of research.

A new approach to designing superconducting generators of electromagnetic radiation was proposed in [4]. The approach is based on the use of a resonant circuit that provides the synchronization of the jumps of Abrikosov vortices caused by a low-frequency external magnetic field. The generation of a coherent electromagnetic radiation by Nb superconducting films was observed in the frequency range 0.15–200 MHz. This generation resulted from the effect of two electromagnetic fields applied to the field normally to its surface: the first field, which was produced by a transport current flowing through a coil, varied relatively slowly in time and caused the motion of the Abrikosov vortices in the film; the second, high-frequency, field synchronized the jumps of the vortices from one inhomogeneity to another. The high-frequency field was obtained by using the film radiation itself with the help of a feedback. This paper reports on the observation of a similar generation of electromagnetic radiation by high-T_c superconducting films at liquid-nitrogen temperatures.

The measurements were performed on $GdBa_2Cu_3O_{7-x}$ films prepared by V.I. Dedyu by the channel-spark technique [5]. This technique resembles the laser ablation method of film deposition. The $GdBa_2Cu_3O_{7-x}$ films were chosen among other 1-2-3 cuprate high-T_c superconductors, because they were more uniform in oxygen content and exhibited a higher stability and reproducibility. The substrates were $NdGaO_3$ single-crystal polished plates with the (110) orientation. The critical temperature of the films was within 91–92.6 K, and the superconducting transition width was ~0.5 K.

The measuring circuit is shown in Fig. 1. The film was placed in an ac magnetic field varying according to the law $H_\perp = H_{\perp 0}\sin(2\pi f_{\rm exc}t)$, where t is time. The field amplitude $H_{\perp 0}$ reached 100 Oe, and the frequency $f_{\rm exc}$ was within 17 Hz to 1 kHz. Such a magnetic field gives rise to Abrikosov vortices in the film. The interaction between the vortices and the film inhomogeneities prevents the vortex system from passing to the equilibrium state. The departure of the vortex system from equilibrium manifests itself in the hysteresis of the magnetization curve. The probability P for the vortices or the flux bundles to leave a pinning center by jumping to an adjacent center or by escaping from the film obeys the relation

$$P \sim \Omega\exp(-U/k_{\rm B}T),$$

where T is temperature, $k_{\rm B}$ is the Boltzmann constant, U is the potential well depth of the pinning center, and Ω is the characteristic frequency of the vortex attempts to leave this pinning center. Such a disordered vortex motion gives rise to an electromagnetic noise generation by the superconducting film.

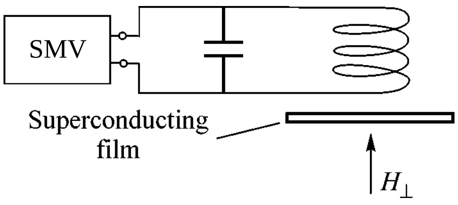

Fig. 1. Measuring circuit (SMV is a selective microvoltmeter).

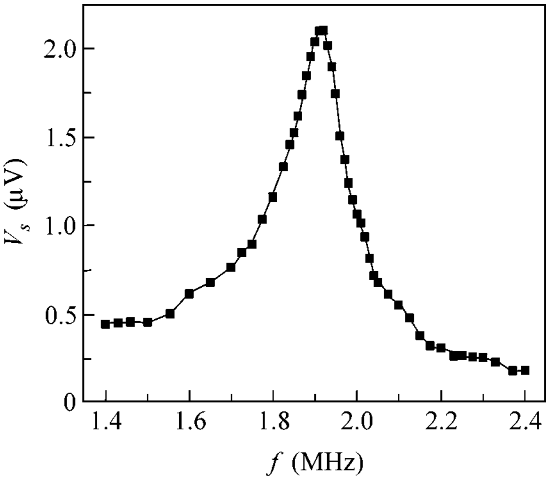

Fig. 2. Example of the frequency dependence of the signal amplitude generated by a $GdBa_2Cu_3O_{7-x}$ film; $H_{\perp 0}$ = 82 Oe and f_{exc} = 915 Hz. The measurements were performed in liquid nitrogen (T = 77.4 K).

The inductance of the resonant circuit is placed near the film, which provides the electromagnetic coupling of the film with the circuit (Fig. 1). The energy of the interaction between the Abrikosov vortices and the pinning centers depends on many parameters and, specifically, on the external magnetic field. Therefore, the electromagnetic oscillations that randomly occur in the circuit periodically help some vortices to overcome the potential barriers and to jump to adjacent pinning centers. This leads to the generation of an electromagnetic pulse, which in its turn causes an increase in the electromagnetic oscillation energy in the circuit. If the loss in the circuit is less than the energy introduced in it through this mechanism, the oscillation amplitude in the circuit increases. As a result, one obtains a feedback and a synchronization of the vortex jumps in the film. The radiation spectrum was measured by a V6-1 frequency-selective microvoltmeter, which had the operating frequency range within 0.15–35 MHz with a bandwidth of 10 kHz. The signal measured by the microvoltmeter was supplied to it from the resonant circuit through a coaxial line.

The generation of coherent electromagnetic radiation from $GdBa_2Cu_3O_{7-x}$ films was observed in the frequency range 1–10 MHz at the temperature corresponding to the boiling point of liquid nitrogen. An example of the generation spectrum is shown in Fig. 2. As in the cited publication [4], the generation frequency is determined by the parameters of the resonant circuit: $f = 1/2\pi(LC)^{0.5}$. By varying the inductance and the capacitance of the circuit, it is possible to vary the frequency of the generated electromagnetic radiation. The presence of the superconducting film does not affect the Q-factor of the resonant circuit and only causes a small (~5%) decrease in the inductance, as compared to the circuit without the film. This indicates that, in our case, the energy dissipation in the circuit far exceeds the dissipation in the film. In the absence of the resonant circuit, the vortex motion in the film is random in character, and only a weak noise radiation can be detected in this case. It was found that the power of this radiation decreases with increasing recording frequency, which leads to a decrease in the power of the generated radiation with increasing generation frequency f. This result is explained by the fact that the noise radiation and the coherent radiation are of the same origin, since both of them are caused by the vortex motion in the film. The maximal generation frequency observed for $GdBa_2Cu_3O_{7-x}$ films in our experiments was much lower than the maximal frequency obtained in similar experiments with Nb films [4]. This can be explained by the strong effect (especially strong at liquid-nitrogen temperatures) of the flux creep on the vortex behavior in high-T_c superconductors, which leads, in particular, to a decrease in the hysteresis formed in the magnetization curve because of the pinning of Abrikosov vortices. At the temperature called the vortex-glass–vortex-liquid phase transition point, this hysteresis, which serves as the source of the radiation energy, totally disappears [6]. As the temperature rises, the departure of the vortex system from the equilibrium state decreases, because the probability P of the vortex jump to an adjacent pinning center grows with increasing energy of thermal fluctuations. This causes a decrease in the electromagnetic oscillations in the circuit and reduces the effect of the feedback on the vortex motion in the film. As a result, the energy of the electromagnetic radiation generated by a high-T_c superconducting film decreases. Since the amplitude of the generated radiation, as well as the amplitude of electromagnetic noise, increases with decreasing frequency, the radiation from high-T_c superconducting films occurs in a smaller frequency range, as compared to the radiation from Nb films.

Figure 3 shows an example of the dependence of the squared amplitude of the generated signal V_s^2 on the magnetic field amplitude $H_{\perp 0}$. The corresponding generation frequency is f = 2.45 MHz, and the frequency of the exciting magnetic field is f_{exc} = 810 Hz. As one can see from this figure, the squared amplitude of the generated signal, i.e., the quantity proportional to the generated power, increases with increasing $H_{\perp 0}$. It was also

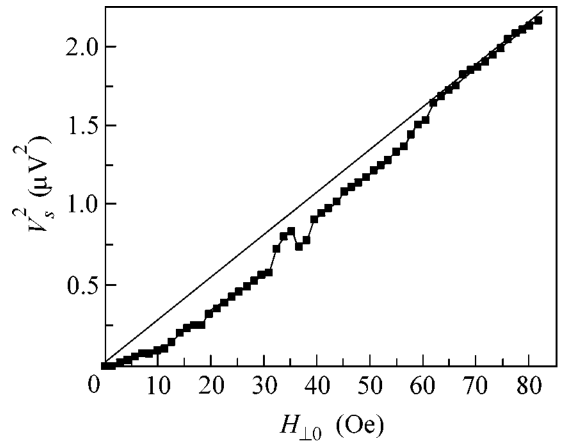

Fig. 3. Dependence of V_s^2 on the amplitude of the exciting magnetic field $H_{\perp 0}$ at $T = 77.4$ K. The generation frequency in this case is 2.45 MHz and $f_{\rm exc} = 810$ Hz.

found that the radiation power grows with increasing frequency $f_{\rm exc}$. This is related to the fact that the radiation power is proportional to the number of Abrikosov vortices involved in the process and to the magnetization cycles per unit time. A small deviation from the linear law for small $H_{\perp 0}$ is caused by the Meissner effect. The radiation power and the maximal radiation frequency decrease with increasing temperature, and near the critical temperature of the film, the generation disappears. A temperature rise is accompanied by a decrease in the pinning forces, which prevent the vortices from occupying the minimal-energy positions in the film; as a result, the hysteresis of the magnetization curve decreases.

Thus, this study proves that high-T_c superconducting films can generate high-frequency electromagnetic radiation. The principle of operation of superconducting generators of this kind is based on the synchronization of the jumps of Abrikosov vortices, which are produced by a low-frequency external magnetic field, with the help of a resonant circuit. In this respect, the behavior of high-T_c superconducting films is close to the behavior of Nb films [4]. An important result of this study is that the generation of coherent electromagnetic radiation by superconducting structures can be observed not only at liquid-helium temperatures, but also at the boiling point of liquid nitrogen. This offers new possibilities for using high-T_c superconductors in superconducting electronics. An important advantage of the described method of generation is the possibility to obtain a high radiation power, which can be achieved by increasing the area of the film part involved in the process, as well as by increasing the amplitude $H_{\perp 0}$ and the frequency $f_{\rm exc}$ of the electromagnetic field exciting the vortex system in the film. The revealed phenomenon also offers new possibilities for studying nonstationary and nonequilibrium processes in the vortex system of a superconductor; for example, it can be used for investigating the physical nature of the frequency Ω of the vortex attempts to leave the pinning centers. The use of resonant circuits with high Q-factors can provide additional information on the dissipation in superconductors in the mixed state.

This work was supported by the Scientific and Engineering Council on Physics of Condensed Media (project no. 30396), the Russian Foundation for Basic Research (project no. 00-02-16076), and the Russian-Ukrainian project “Etalon.”

The author is grateful to V.I. Dedyu for supplying the $GdBa_2Cu_3O_{7-x}$ films.

REFERENCES

1. B. D. Josephson, Phys. Lett. **1**, 251 (1962).
2. A. K. Jain, K. K. Likharev, J. E. Lukens, *et al.*, Phys. Rep. **109**, 309 (1984).
3. V. P. Koshelets, S. V. Shitov, A. V. Shchukin, *et al.*, IEEE Trans. Appl. Supercond. **7**, 2905 (1997).
4. A. N. Lykov, Phys. Lett. A **281**, 48 (2001).
5. V. G. Kantser, D. V. Gitsu, V. I. Dedyu, *et al.*, Izv. Akad. Nauk Resp. Mold., Ser. Fiz.-Tekh. Mat. Nauk, No. 2, 6 (1992).
6. R. H. Koch, V. Foglietti, W. J. Gallager, *et al.*, Phys. Rev. Lett. **63**, 1511 (1989).

Translated by E. Golyamina

JETP Letters, Vol. 73, No. 10, 2001, pp. 552–556. Translated from Pis'ma v Zhurnal Éksperimental'noĭ i Teoreticheskoĭ Fiziki, Vol. 73, No. 10, 2001, pp. 621–625.
Original Russian Text Copyright © 2001 by Glazov, Mukhamad'yarov, Brazhkin, Lyapin, Gromnitskaya, Stal'gorova, Popova.

Anisotropy of the Elastic Properties and the Microhardness of Disordered Superhard Carbon Obtained from C_{60} Fullerite under High Pressures

A. G. Glazov, V. V. Mukhamad'yarov, V. V. Brazhkin, A. G. Lyapin, E. L. Gromnitskaya, O. V. Stal'gorova, and S. V. Popova

Institute for High Pressure Physics, Russian Academy of Sciences, Troitsk, Moscow region, 142190 Russia

Received April 17, 2001

An anisotropy of the propagation velocities of longitudinal and transverse ultrasonic waves, as well as of the microhardness, is observed for disordered graphite-like samples obtained from C_{60} fullerite by heating to different temperatures between 1000 and 1300°C under a pressure of 7.5 GPa. The anisotropy of the elastic properties and the microhardness is attributed to the additional pressure component that occurs in the quasi-hydrostatic experimental conditions. The elastic characteristics of the samples are determined with allowance for the uniaxial orientational anisotropy. A model description relating the observed properties of superhard sp^2 carbon to its possible structural features and to the mechanism of its formation is proposed. *© 2001 MAIK "Nauka/Interperiodica".*

PACS numbers: 61.48.+c; 62.20.Dc; 62.50.+p

1. The C_{60} fullerite is an object of great interest for investigations, because the carbon phases obtained from it combine low densities with high mechanical and elastic characteristics [1–16]. Under the effect of temperature and pressure, the C_{60} fullerite can transform to molecular polymer phases or to disordered or nanocrystalline modifications, depending on the experimental conditions [1–19]. By varying the synthesis conditions, it is possible to control such important structural characteristics of carbon materials as the density, the proportion of atoms in the sp^2 and sp^3 states, the effective dimension of the covalent structure bonding (1D, 2D, or 3D), the degree of polymerization in the structures based on C_{60} molecules, and the degree of homogeneity in the nanocomposite phases [7–11, 16–18]. This paper shows that the orientational anisotropy of elastic properties can also be an experimentally controlled parameter of materials produced from C_{60}.

An instrument for controlling the anisotropy should apparently be the presence of a uniaxial pressure component. The pressure anisotropy naturally occurs in quasi-hydrostatic conditions that occur in toroid-type chambers with a single loading axis. For three-dimensional C_{60} polymers obtained in such chambers, the presence of a structural anisotropy was observed [20]. One of the direct methods for revealing the anisotropy is the ultrasonic technique. The study of the anisotropy of elastic properties is also topical from another point of view. Until now, in the studies of the elastic properties of materials obtained from C_{60}, the bulk B and shear G moduli were calculated by using the isotropic medium approximation [12–16]. Such calculations provided values of the Poisson ratio that were anomalously high for covalent structures [12–15] and values of the bulk modulus that were nonphysically high [12–14]. However, the possible orientational anisotropy and inhomogeneity (see the example in [15]) of materials were not taken into account in these calculations.

This paper describes the study of the orientational anisotropy of the elastic properties and microhardness of superhard samples with a disordered graphite-like (i.e., mainly sp^2) structure. Such samples can be synthesized at relatively low pressures up to 9 GPa and at temperatures about 1000°C. The interest taken in precisely these phases is caused by two factors. First, these phases are likely to have (as graphite) a 2D covalent structure with a short-range order, i.e., a considerable anisotropy of the atomic packing on the atomic scale. Second, the disordered sp^2 phases have a density that usually is lower than the graphite density (1.8–2.2 g/cm^3), whereas their hardness is comparable with or higher than that of corundum Al_2O_3 (20–40 GPa) [4, 10, 16].

Experiments showed that the elastic properties of these phases are really characterized by a considerable anisotropy. Moreover, it was found that the velocities of both longitudinal and transverse ultrasonic waves propagating along the axis, which was used as the loading axis in the sample synthesis, were systematically lower than the corresponding velocities in the perpendicular direction. A model description of this phenomenon provides important information on the mechanism of the formation of the sp^2 carbon phase from C_{60}.

0021-3640/01/7310-0552$21.00 © 2001 MAIK "Nauka/Interperiodica"

2. The disordered samples were synthesized from a fullerite powder with a C_{60} content no less than 99.9% under the pressure $P = 7.5$ GPa at temperatures from 1000 to 1300°C. The high pressure was obtained in a toroid-type chamber. The temperature was measured by chromel–alumel thermocouples. To study the possible effect of the substance surrounding the fullerite on the anisotropy of the synthesis conditions, two types of containers were used: a graphite container, which simultaneously served as a heater, and a NaCl container with an external Ta heater. The synthesized material was obtained in the form of cylinders, which were used to prepare samples in the form of parallelepipeds with the characteristic dimensions 1.5 × 1.5 × 1.2 mm. The phase composition of the samples was determined by the X-ray diffraction method (CuK_α), and the density of the samples was determined by the picnometric method. The ultrasonic measurements consisted in measuring the time of the longitudinal and transverse ultrasonic wave propagation through the sample at a frequency of 10 MHz. The microhardness was measured by the Vickers indentation method by a PMT-3 hardness tester with a load of 2 N.

3. The experimental results are presented in the figure and in Table 1. The values obtained for the density and the microhardness, $\rho = 1.9–2.4$ g/cm^3 and $H_V = 21–32$ GPa, are in good agreement with the data reported for disordered phases in earlier publications [4, 10, 16]. The velocities of longitudinal and transverse ultrasonic waves also agree with the velocity values obtained earlier for similar phases [15, 16]. The X-ray diffraction curves obtained for the synthesized samples (see similar curves in [4, 16]) indicate that the phases under study are strongly disordered and have a graphite-like (sp^2) structure. The estimate of the X-ray coherent scattering length from the first diffraction peak width (the details of such a calculation can be found in [8]), which virtually corresponds to the mean size of the graphite-like clusters or nanocrystallites, yields a value of about 16–20 Å.

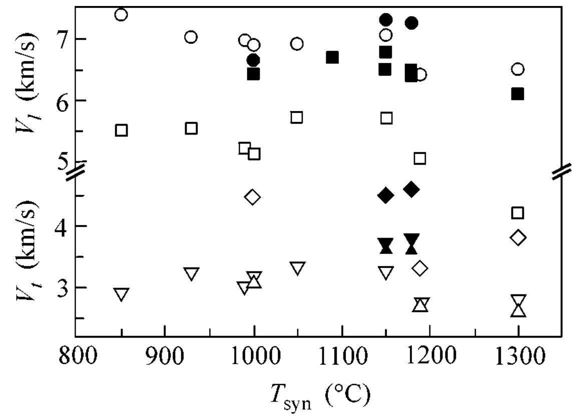

Dependence of the velocities of longitudinal and transverse ultrasonic waves with different propagation directions and polarizations on the synthesis temperature for the samples obtained in graphite (open symbols) and NaCl (closed symbols) containers: (○, ●) V_{lx}; (□, ■) V_{lz}; (▽, ▼) V_{tz}; (△, ▲) V_{tx}^z; and (◇, ◆) V_{tx}^y.

A fundamentally new result is the strong anisotropy observed for the velocities of transverse and, especially, longitudinal ultrasonic waves propagating parallel and perpendicularly to the z axis, which corresponds to the loading axis of the sample synthesis. The anisotropy of the velocities reaches 20–30%. For microhardness, the values obtained with the indentation parallel to the z axis (H_z) and perpendicular to it (H_x) are also different, the microhardness anisotropy being within ~15–20%.

From the point of view of the synthesis conditions, the material of the samples should exhibit an anisotropy in a single selected direction z, whereas all directions lying in the xy plane must be equivalent. The elastic constant tensor of such a material is similar to the corresponding tensor of a crystal with a hexagonal symmetry [21]; i.e., it is characterized by five independent constants: c_{11}, c_{12}, c_{33}, c_{13}, and c_{44} (for the remaining non-

Table 1. Experimental values of the density, the velocities of longitudinal (l) and transverse (t) ultrasonic waves (the subscript corresponds to the propagation axis, and the superscript corresponds to the polarization direction), and the microhardness (the subscript indicates the indentation axis) for the samples synthesized from C_{60} at different synthesis temperatures T_{syn} under a pressure of 7.5 GPa

No.	T_{syn} (°C)	ρ (g/cm^3)	V_{lz} (km/s)	V_{lx} (km/s)	V_{tz} (km/s)	V_{tx}^z (km/s)	V_{tx}^y (km/s)	H_z (GPa)	H_x (GPa)
1	1000	2.2	5.14	6.9	3.2	3.05	4.48	–	–
2	1000	2.21	6.44	6.55				27	32
3	1150	2.3	6.78	7.3	3.7	3.6	4.5	–	–
4	1180	2.4	6.5	7.25	3.8	3.6	4.6	21	27
5	1190	2.05	5.05	6.42	2.75	2.7	3.3		
6	1300	1.99	4.2	6.5	2.8	2.6	3.8	–	–
±Δ	100	0.1	0.15	0.15	0.15	0.15	0.15	3	3

zero elastic constants, the following equalities are valid: $c_{22} = c_{11}$, $c_{23} = c_{13}$, $c_{55} = c_{44}$, and $c_{66} = \frac{1}{2}(c_{11} - c_{12})$. In the experiment, we measured five ultrasonic velocities (Table 1): two longitudinal wave velocities along the x and z axes (V_{lx} and V_{lz}) and three transverse wave velocities—one along the z axis and two along the x axis with the y and z polarization directions (V_{tz}, V_{tx}^y, and V_{tx}^z). The relations between these velocities and the components of the elastic constant tensor are well known [22]:

$$\rho V_{lx}^2 = c_{11}, \quad \rho V_{lz}^2 = c_{33}, \tag{1a}$$

$$\rho V_{tx}^{y2} = \frac{1}{2}(c_{11} - c_{12}), \tag{1b}$$

$$\rho V_{tx}^{z2} = \rho V_{tz}^2 = c_{44}. \tag{1c}$$

Equation (1c) provides a natural possibility to test the validity of our description of the elastic properties in terms of the tensor of a medium with a single anisotropy axis. From the figure, one can see that the values of the velocities V_{tz} and V_{tx}^z really coincide within the measurement accuracy, the scatter in the values of these velocities being much greater from one sample to another. The results obtained by calculating the components of the elastic constant tensor are presented in Table 2. The only quantity that remains undetermined is c_{13}, because its determination requires the measurement of the propagation velocities at an angle to the x and z axes, which is difficult because of the geometric limitations imposed on the dimensions of the synthesized samples. In an isotropic medium, we have $c_{13} = c_{12}$, and the degree of anisotropy along the z axis can be estimated from the ratio c_{33}/c_{11}; i.e., we obtain the estimate $c_{13} \approx c_{12}(c_{33}/c_{11})$ (see Table 2). The bulk modulus B can be determined by averaging according to the Voigt–Reuss–Hill approach [23, 24].

In the framework of the chosen approximation, we estimate the values of the Poisson ratio, which depend on the measurement orientation, from the components of the inverse elastic constant tensor (where the subscript corresponds to the loading axis and the superscript corresponds to the axis along which the variation of the transverse dimension is measured):

$$\sigma_z = c_{13}/(c_{11} + c_{12}), \tag{2a}$$

$$\sigma_x^y = \frac{c_{12}c_{33} - c_{13}^2}{c_{11}c_{33} - c_{13}^2}, \tag{2b}$$

$$\sigma_x^z = \frac{(c_{11} - c_{12})c_{13}}{c_{11}c_{33} - c_{13}^2}. \tag{2c}$$

The calculated values of the Poisson ratio are also presented in Table 2.

4. The presence of anisotropy should naturally be attributed to the uniaxial pressure anisotropy that occurs in the quasi-hydrostatic conditions of the experiment. In the case of the synthesis with the use of NaCl containers, which provide a higher degree of hydrostatics (graphite is a soft material only at low pressures), the difference in the elastic characteristics corresponding to different directions is much smaller (see figure). An unexpected result was that the ultrasonic velocities along the x axis proved to be higher than the corresponding velocities along the z axis. The additional positive pressure component is directed along the z axis, and this fact determines, e.g., the higher degree of polymerization along the z axis in 3D polymers [20]. From the data on the Brillouin scattering, it is also known that, in amorphous (mainly sp^3) samples synthesized from C_{60} under pressures of about 13 GPa, the velocity of acoustic waves is higher in the case of their propagation along the z axis [25].

The X-ray diffraction data suggest that the sp^2 phases under consideration have a nanocluster structure in which the clusters can have the form of graphite-like crystallites with a parallel atomic packing or an amorphous conglomerate of partially ordered nanoregions, as in, e.g., CN_x films [26]. The orientation of the clusters should exhibit a wide scatter, which does not preclude the possibility of further correlations in the cluster orientations, such as the correlations observed earlier by electron diffraction and related to the initial fullerite structure [27]. The velocities of ultrasonic

Table 2. Components of the elastic constant tensor (according to the calculations by Eqs. (1)), the estimate for c_{13} (see text), the bulk modulus, and the Poisson ratios in different directions for the samples from Table 1 (the sample numbers are retained)

No.	c_{11} (GPa)	c_{33} (GPa)	c_{44} (GPa)	c_{12} (GPa)	c_{13} (GPa)	B (GPa)	σ_z	σ_x^y	σ_x^z
1	104.7	58.1	22.5	16.4	9.1	37.4	0.08	0.15	0.13
2	94.8	91.7	–	–	–	–	–	–	–
3	122.6	105.7	31.5	29.4	25.4	56.8	0.17	0.20	0.19
4	126.2	101.4	34.7	24.6	19.8	53.5	0.13	0.17	0.16
5	84.5	52.3	15.5	39.8	24.7	44.4	0.20	0.38	0.29
6	84.1	35.1	15.6	26.6	11.1	33.4	0.10	0.28	0.23

waves propagating along the graphite planes are known to be higher than the propagation velocities in the perpendicular directions (for transverse waves, the polarization must also be parallel to these planes in the case of fast waves). It is natural to attribute the anisotropy of the elastic properties observed in the experiment to the anisotropy of the spatial orientation of the structure-forming clusters, namely, to the presence of the preferred orientation of graphite-like planes that is normal to the z axis. The deviation from the spherically symmetric distribution of the orientation of graphite-like clusters leads to the formation of a sort of texture in the disordered samples.

Let us consider a possible mechanism for the formation of an anisotropic cluster system under pressure in the process of the disruption of the fullerite structure. It is well known that graphite is much more compressible along the (001) direction; i.e., in the presence of an additional positive pressure component along the chamber axis (the z axis), the orientation of clusters with (001) $\parallel z$ proves to be preferred, because, in this case, the density of the cluster system is higher and the PV contribution to the Gibbs thermodynamic potential is smaller. Although, in the conditions under consideration ($P = 7.5$ GPa and $T \sim 1000°\mathrm{C}$), the system is far from thermodynamic equilibrium (in this case, the stable phase is diamond), the energy relations can be significant in comparing different scenarios of the graphite-like cluster formation from the structure based on C_{60} molecules, because such a process must occur in a diffusion way.

We note that the ultrasonic velocities weakly depend on the temperature of the sample synthesis (see figure). However, the scatter in the experimental values far exceeds the measurement error and is presumably related to the variations in the texture. In the temperature interval 1200–1300°C, the ultrasonic velocities exhibit a certain decrease, which can be attributed to the recrystallization processes in the conglomerate of nanoclusters.

The observed anisotropy of elastic properties is significant for analyzing the experimental data. If the elastic moduli are calculated in the framework of the isotropic medium model, considerable errors may occur in the measurements along a single axis. For example, for sample no. 6 (see Table 1), the isotropic medium approximation, when applied separately to the data obtained for different directions, provides the values of the bulk modulus $B \approx 15$ and 55 GPa for the z axis and the x axis; i.e., one obtains values that differ by a factor of more than three. The aforementioned values of the Poisson ratios that are anomalously high for covalent structures [12–15] are presumably related to the application of such an incorrect approach. In our case, the isotropic medium approximation applied to the measurements along a single axis for sample nos. 1–3 yields the values $\sigma \sim 0.25$–0.32, which far exceed the values of the Poisson ratios obtained with allowance for the anisotropy and, presumably, being more adequate for carbon covalent structures.

5. Thus, in analyzing the elastic properties of the phases synthesized from C_{60} under pressure in quasi-hydrostatic conditions, it is necessary to take into account the anisotropy, e.g., by using Eqs. (1) and (2). The study of the anisotropy of polymerized phases is of special interest, because it can provide information on the mechanisms of their formation. The possibility to create an anisotropy (a texture) in superhard samples can be of practical interest, e.g., for increasing the hardness in certain directions.

We are grateful to A.P. Kochkin and E.V. Tat'yanin for useful discussions. The work was supported by the Russian Foundation for Basic Research (project nos. 99-02-17408, 00-15-99308, and 01-02-16557).

REFERENCES

1. V. V. Brazhkin, A. G. Lyapin, Yu. V. Antonov, *et al.*, Pis'ma Zh. Éksp. Teor. Fiz. **62**, 328 (1995) [JETP Lett. **62**, 350 (1995)].
2. V. V. Brazhkin, A. G. Lyapin, and S. V. Popova, Pis'ma Zh. Éksp. Teor. Fiz. **64**, 755 (1996) [JETP Lett. **64**, 802 (1996)].
3. V. V. Brazhkin and A. G. Lyapin, Usp. Fiz. Nauk **166**, 893 (1996) [Phys. Usp. **39**, 837 (1996)].
4. M. E. Kozlov, M. Hirabayashi, K. Nozaki, *et al.*, Appl. Phys. Lett. **66**, 1199 (1995).
5. V. D. Blank, S. G. Buga, N. R. Serebryanaya, *et al.*, Phys. Lett. A **205**, 208 (1995).
6. V. D. Blank, S. G. Buga, N. R. Serebryanaya, *et al.*, Phys. Lett. A **220**, 149 (1996).
7. V. V. Brazhkin, A. G. Lyapin, S. V. Popova, *et al.*, Phys. Rev. B **56**, 11465 (1997).
8. V. V. Brazhkin, A. G. Lyapin, S. V. Popova, *et al.*, J. Appl. Phys. **84**, 219 (1998).
9. B. V. Brazhkin, A. G. Lyapin, C. G. Lyapin, *et al.*, Usp. Fiz. Nauk **167**, 1019 (1997) [Phys. Usp. **40**, 969 (1997)].
10. A. G. Lyapin, V. V. Brazhkin, S. G. Lyapin, *et al.*, Phys. Status Solidi B **211**, 401 (1999).
11. B. V. Brazhkin, A. G. Lyapin, R. N. Voloshin, *et al.*, Pis'ma Zh. Éksp. Teor. Fiz. **69**, 822 (1999) [JETP Lett. **69**, 869 (1999)].
12. V. D. Blank, V. M. Levin, V. M. Prokhorov, *et al.*, Zh. Éksp. Teor. Fiz. **114**, 1365 (1998) [JETP **87**, 741 (1998)].
13. V. M. Levin, V. D. Blank, V. M. Prokhorov, *et al.*, J. Phys. Chem. Solids **61**, 1017 (2000).
14. V. D. Blank, V. M. Prokhorov, S. G. Buga, *et al.*, Physica B (Amsterdam) **265**, 220 (1999).
15. S. Berezina, V. Blank, V. Levin, and V. Prokhorov, Ultrasonics **38**, 327 (2000).
16. A. G. Lyapin, V. V. Brazhkin, E. L. Gromnitskaya, *et al.*, Appl. Phys. Lett. **76**, 712 (2000).
17. L. Marques, J.-L. Hodeau, M. Núñez-Regueiro, *et al.*, Phys. Rev. B **54**, R12633 (1996).
18. V. A. Davydov, L. S. Kashevarova, A. V. Rakhmanina, *et al.*, Phys. Rev. B **58**, 14786 (1998).

19. H. Hirai, K. Kondo, N. Yoshizava, and M. Shiraishi, Appl. Phys. Lett. **64**, 1797 (1994).
20. L. Marques, M. Mezouar, J. L. Hodeau, *et al.*, Science **283**, 1720 (1999).
21. G. Grimvall, in *Thermodynamical Properties of Materials* (Elsevier, Amsterdam, 1999), p. 329.
22. R. Truell, C. Elbaum, and B. B. Chick, *Ultrasonic Methods in Solid State Physics* (Academic, New York, 1969; Mir, Moscow, 1972).
23. I. N. Frantsevich, F. F. Voronov, and S. A. Bakuta, *Elastic Constants and Elastic Modules of Metals and Non-metals* (Naukova Dumka, Kiev, 1982).
24. M. W. Guinan and D. J. Steinberg, J. Phys. Chem. Solids **35**, 1501 (1974).
25. M. N. Manghnani, S. Tkachev, P.V. Zinin, *et al.*, submitted to Phys. Rev. Lett. (2001).
26. M. Sjöström, S. Stafström, M. Boman, *et al.*, Phys. Rev. Lett. **75**, 1336 (1995).
27. V. D. Blank, Ye. V. Tatyanin, and B. A. Kulnitskiy, Phys. Lett. A **225**, 121 (1997).

Translated by E. Golyamina

JETP Letters, Vol. 73, No. 10, 2001, pp. 557–561. Translated from Pis'ma v Zhurnal Éksperimental'noĭ i Teoreticheskoĭ Fiziki, Vol. 73, No. 10, 2001, pp. 626–630.
Original Russian Text Copyright © 2001 by Ermolov, Indenbom, Rossolenko, Bdikin, Uspenskaya, Stepakov, Glebovskiĭ.

Superconducting MgB_2 Films Obtained by Magnetron Sputtering

S. N. Ermolov*, M. V. Indenbom, A. N. Rossolenko, I. K. Bdikin, L. S. Uspenskaya,
N. S. Stepakov, and V. G. Glebovskiĭ
Institute for Solid-State Physics, Russian Academy of Sciences, Chernogolovka, Moscow region, 142432 Russia,
** e-mail: ermolov@issp.ac.ru*

Received April 17, 2001

Superconducting MgB_2 films with a superconducting transition temperature of 24 K were obtained by magnetron sputtering. The high homogeneity of the films was demonstrated by the magneto-optical imaging of the magnetic flux penetration. © *2001 MAIK "Nauka/Interperiodica".*

PACS numbers: 74.76.Bz; 74.60.Gc; 81.15.Cd

1. Discovering superconductivity in magnesium diboride with a critical temperature of 39 K [1], which was announced at the beginning of January, triggered a real outburst of studied on magnesium diboride properties. Special hopes are associated with the fact that critical currents in this novel high-T_c superconductor are not so sensitive to the disorientation of crystal grains as in oxide superconductors [2, 3]. In this respect, the magnetic and transport properties of polycrystalline MgB_2 more closely resemble the properties of Nb–Ti and Nb_3Sn intermetallic compounds, which have become the base for the best low-temperature superconducting cables. Because of its anisotropic structure, single crystals of MgB_2 must be obtained for fundamental studies of the nature of superconductivity in this material. However, the sublimating temperatures of volatile magnesium and refractory boron differ significantly, and a vapor pressure of 1.3×10^{-2} Pa is attained for Mg and B at 327 and 1797°C, respectively. Therefore, this task seems to be virtually impossible. This problem can be solved partially with the use of oriented MgB_2 films, which may simultaneously become a basis for microelectronic applications of the new superconductor.

The same "incompatibility" of magnesium and boron and, in addition, the very high oxidizing ability of magnesium are also the main obstacles on the way to obtaining quality MgB_2 films. Against the background of an already rather large amount of studies carried out with bulk samples, there are only a few communications on the successful deposition of films [4–15]. A pulsed laser deposition technique was used in almost all these studies, and electron beam evaporation was used only in some cases. Only for films that were annealed in magnesium vapor after their deposition was it possible to bring the critical temperature closer to the critical temperature of bulk MgB_2. In this case, it was sufficient to obtain a pure boron film and to transform it to the MgB_2 film only in the process of the subsequent *ex situ* annealing, much as thin MgB_2 wires have been obtained recently [3]. However, because the crystal lattice expands significantly in the process of transformation, films with good structure cannot be obtained by this method. The direct deposition of stoichiometric films with only minor finishing in the process of *in situ* annealing is much more delicate. Samples that can be obtained in this way so far have a critical temperature of only about 24 K, but their surface is considerably smoother (see a comparison of various preparation methods and an analysis of growth mechanisms of MgB_2 films in [13]).

It should be noted here that pulsed laser deposition has significant disadvantages. The film deposition rate is very limited. Because of this, the requirements on the quality of the initial vacuum must be considerably more stringent in order to prevent the oxidation of magnesium, and films of large thickness cannot be obtained. Magnesium droplets appear on the surface of films, which may locally disturb the superconductivity of films. Plasma sputtering techniques are free from these disadvantages and more efficient technologically. Films with a large area and considerably better uniformity can be sputtered with the use of these techniques. Such films comply with the standards of microelectronics. In this work, we report the first, as far as we know, successful deposition of MgB_2 films by magnetron sputtering.

2. Composite Mg–MgB_2 targets. In order to compensate for the losses of magnesium due to its oxidation in plasma, we used composite targets containing MgB_2 and metallic magnesium in approximately equal amounts, as was proposed in studies carried out using pulsed laser deposition at the University of Twente [5, 9]. The stoichiometric ceramic base of the target was prepared by thoroughly mixing powders of pure Mg and B in a ratio corresponding to the MgB_2 compound. The mixture was compacted into pellets 32 mm

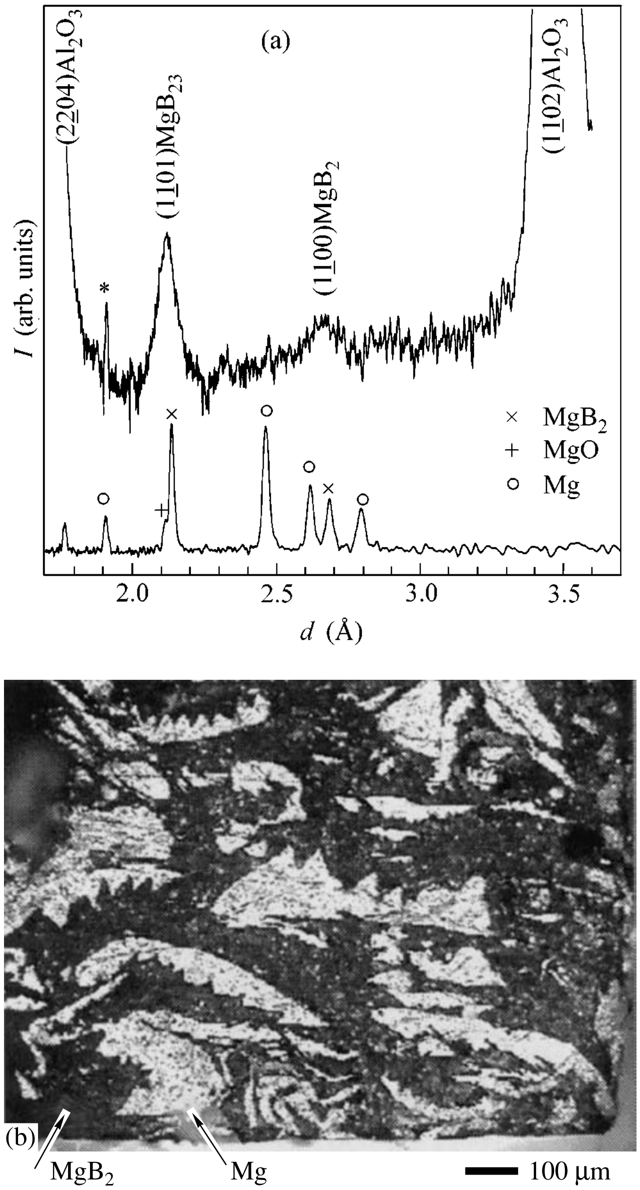

Fig. 1. (a) X-ray diffractograms of θ–2θ scanning for a magnetron Mg–MgB$_2$ target (lower curve, CuK_α radiation) and for a MgB$_2$/(1$\underline{1}$02)Al$_2$O$_3$ film (upper curve, CrK_α radiation); (b) fragment of a cross-cut of the magnetron target.

in diameter using a conventional laboratory press. Next, these pellets were placed in an alundum crucible along with a plate of pure magnesium having the same weight. The crucible was placed in a vacuum chamber containing an induction heating device. After preliminary evacuation down to a pressure of 10^{-3} Pa, the chamber was filled with pure argon up to a pressure of several atmospheres. The synthesis was carried out for 30 min at a temperature of ~900°C. As a result, composite pellets were obtained with fanciful lamellas of pure magnesium (light areas in the metallographic section of a target cross-cut; see Fig. 1b) and fine-grained MgB$_2$ (dark areas) distributed uniformly. The target structure was extremely dense, and all the cavities, which usually form in the synthesis of ceramic MgB$_2$, were filled with magnesium. Such a dense structure is very important for obtaining good heat transfer and preventing the targets from cracking in the process of vigorous sputtering.

The X-ray diffraction spectrum of the target material (the lower curve in Fig. 1a) contains intense peaks of MgB$_2$ and Mg and reveals insignificant traces of MgO (copper K_α radiation was used, $\lambda_{K_\alpha} = 1.54$ Å). The unit cell parameters of the MgB$_2$ phase were found to be $a = 3.092$ Å and $c = 3.521$ Å, which is in agreement with published data. The temperature dependence of the electrical resistance (×40) measured by the four-probe method in a thin plate that was cut from the target using a diamond disk is presented in Fig. 2. The resistance decreases with temperature almost linearly with a sharp superconducting transition at $T_c(R = 0) \sim 37$ K. The ratio of resistances $R_{300\,\mathrm{K}}/R_{40\,\mathrm{K}} \sim 10$ indicates that the material is of high purity. Good superconducting properties of the MgB$_2$ phase areas are confirmed by magnetooptical observations of magnetic field penetration in these plates.

The finished Mg–MgB$_2$ targets were tin-plated by an ultrasonic soldering iron and were soldered with indium to copper water-cooled holders. The target structure obtained provided their operation in the extreme modes of magnetron sputtering without any traces of destruction. We successfully used the same targets for obtaining MgB$_2$ films by pulsed laser deposition with results similar to those obtained by other groups and mentioned above.

3. Obtaining and characterizing MgB$_2$ films. The uniqueness of our magnetron sputtering system developed specially for laboratory purposes is in the possibility of using miniature targets 32 mm in diameter, which we managed to prepare. As a rule, the existing industrial systems of magnetron sputtering are designed for operation with targets of a large diameter of 76 mm and larger. The manufacturing of such targets is a significantly more complicated problem and is not reasonable at the research stage. The possibility of operation with small targets in our system was provided by the inclusion of strong constant SmCo$_5$ magnets into the magnetron construction. The system was created on the basis of a vacuum VUP-5 station completed with a turbo-molecular VMN-500 pump with a nitrogen cryopanel. The limiting vacuum that is attained in the working volume measures 5×10^{-5} Pa.

A Mg–MgB$_2$ pellet was sputtered in a high-purity argon atmosphere (99.998%) at a pressure of 3 Pa. The constant voltage across the target was ~ 410 V, and the discharge current was 350 mA. This corresponded to a high power density of ~ 120 W/cm^2 at the active part of the target. The film sputtering rate in this case was ~0.04 μm/min. It should be noted that the plasma cloud created at such a large specific power served as additional protection against magnesium oxidation. Standard substrates of single crystal sapphire with a $(1\bar{1}02)$ orientation of the surface were used. According to first communications, in spite of the large difference between the unit cell parameters of sapphire ($R3c$, a = 4.76 Å, c = 12.99 Å) and MgB_2 ($P6mmm$, a = 3.09 Å, and c = 3.52 Å), MgB_2 films grown on single crystal sapphire are among the best ones. The substrates were glued to the heater table using conducting silver glue to provide good thermal contact with the table. The table temperature was controlled using a thermocouple.

The best films were obtained when the substrate temperature in the process of sputtering was 200°C and was raised to 600°C for several seconds at the final stage only. During this final *in situ* annealing, the plasma discharge was not switched off. The reverse cooling of the film down to 200°C was performed in 3.5 min.

The X-ray diffraction spectra of such a film in the θ–2θ scanning geometry were measured on an automated X-ray device DRON-2.0 with a graphite monochromator (the upper curve in Fig. 1a). Chromium radiation (λ_{K_α} = 2.285 Å) was used. This radiation is more effective for the thin films under study because of the small absorptivities of the elements entering into the composition of these films (Mg and B). Strongly broadened diffraction reflexes of $(1\bar{1}00)$ and $(1\bar{1}01)$ MgB_2 films are clearly seen against the background of intense $(1\bar{1}02)$ and $(2\bar{2}04)$ diffraction peaks from the Al_2O_3 substrate. The narrow peak marked with a star either corresponds to residues of pure magnesium or represents a peak of $(2\bar{2}04)$ Al_2O_3 at the K_β line, which is not completely cut by the monochromator. The strong broadening of MgB_2 peaks indicates that the film is fine-grained. These peaks are located at the same places as the corresponding peaks of crystalline MgB_2 shown in the lower spectrum. That is, the crystal lattice parameters of the film do not strongly differ from their bulk values and can be estimated at a = 3.07 Å and c = 3.49 Å. The average grain size can be estimated from the broadening of the peak of the $(1\bar{1}01)$ film at $D = d^2/(B - B_0)$ = 110 Å, where d = 2.12 Å is the corresponding interplanar spacing, B = 0.06 Å is the peak half-width, and B_0 = 0.02 Å is the correction for the instrumental broadening of lines. This estimate is close to similar estimates for the grain size confirmed by direct observations using electron microscopy [6].

The electrical resistance of films was measured by the conventional four-probe method at a transport current of 10 μA. The contacts were made by ultrasonic tinning with indium. Attempts at using conventional silver paste gave no satisfactory results, apparently, because of the occurrence of an oxide layer on the film surface. The temperature dependence of the resistivity $\rho(T)$ of the film described above is given by curve (×3) in Fig. 2. The resistivity remains virtually constant over the entire temperature range down to the beginning of the superconducting transition at 23.7 K. The value obtained exceeds ρ for crystalline MgB_2 at 40 K by a factor of more than 100 (see curve (×40) in Fig. 2 for the target and the data in [16]) and corresponds to ρ of films with a small oxygen content obtained in [6]. For completeness sake, Fig. 2 also shows $\rho(T)$ for a film that was not subject to the final *in situ* annealing (the upper curve marked with (×1)) with the beginning of the superconducting transition at only 3.6 K and with a considerably greater value of ρ corresponding to the film with an increased oxygen content obtained in [6]. The independence of the resistance from temperature indicates that the mean free path of electrons in the films obtained is small, which is very important for increasing H_{c2} and extending the range of high-field superconductivity [6].

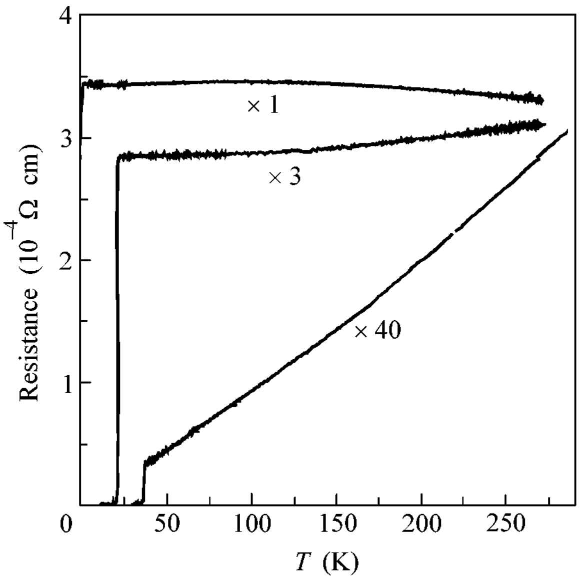

Fig. 2. Temperature dependence of the electrical resistance: (×1) a MgB_2 film deposited on a sapphire $(1\bar{1}02)$ substrate at a temperature of 100°C, (×3) a similar film subject to a short-term annealing *in situ* at 600°C at the end of deposition, and (×40) the material of a composite Mg–MgB_2 target. Marks at curves indicate the coefficient by which the resistance is multiplied to present the curves in the same plot.

The uniformity and critical currents of a film subject to *in situ* annealing were studied by measuring the penetration of a perpendicular magnetic field in the film using a magneto-optical technique [17, 18]. Such investigations are necessary for determining the macroscopic character of the distribution of superconducting currents in the sample and were first used for the analysis of MgB_2 films in [6]. The picture observed (Fig. 3a) is typical of the second-kind superconductors and fully repeats the magnetic field penetration in thin films of high-T_c superconductors thoroughly studied

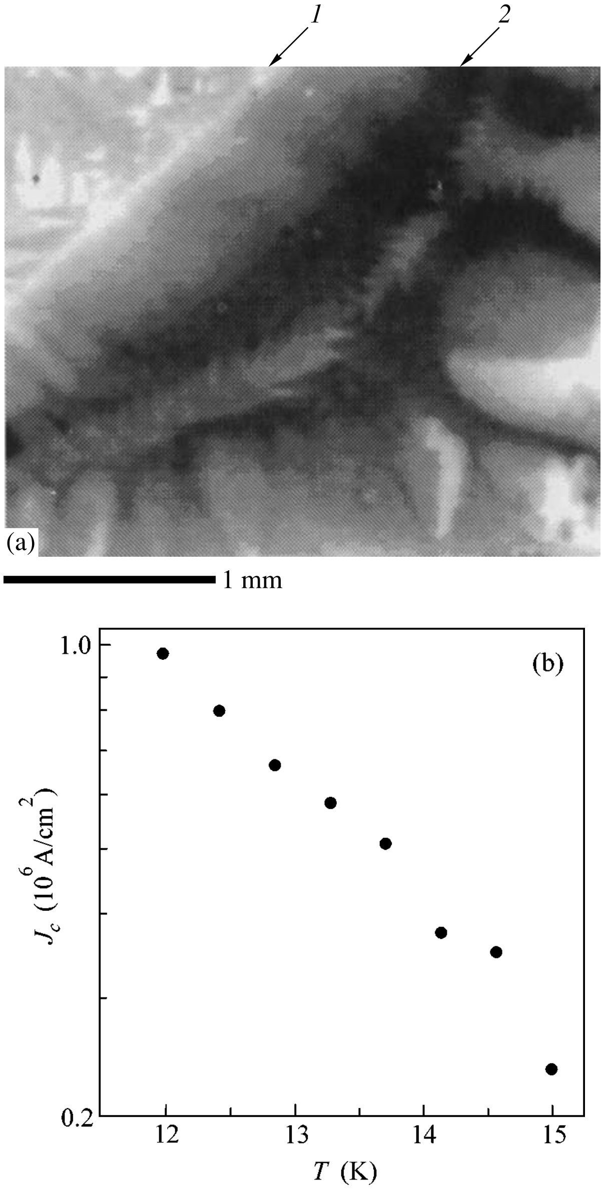

Fig. 3. (a) Observation of perpendicular magnetic field penetration in an annealed MgB_2 film, H = 60 Oe and T = 12 K (arrow *1* indicates the edge of the sample, and arrow *2* indicates the front of magnetic field penetration); (b) temperature dependence of the critical current in this film determined from by a series of such observations.

recently [19, 20]. Attention should be given to the field penetration from the upper (in the figure) edge of the sample, which is revealed as a light strip because of the concentration of the magnetic field. The penetrating flux is seen as a light area with the gradient of brightness from the edge toward the dark Meissner region at the center of the sample (greater brightness corresponds to a higher value of the perpendicular field in the sample). The teeth of the planar domains in the indicator film observed in this region should not be confused with nonuniformities of the magnetic field in the superconductor. The critical current density j_c determined by the field of penetration to 0.9 of the sample width $Hp \simeq j_c h$, where the film thickness h = 1 μm, equals 10^6 A/cm^2 at a temperature of 12 K and rapidly decreases by a factor of more than 5 to 15 K (Fig. 3b). Note the exceptionally flat front of the magnetic flux in Fig. 3a, which points to the high uniformity of the superconducting parameters and the microstructure of our film. This result is in contrast to the recent communication of similar observations of magnetic field penetration in a MgB_2 film obtained by pulsed laser deposition [21]. The nonuniformities of the magnetic flux distribution observed in this work, which exhibit characteristic parabolic “walrus moustache” at defects, are typical for films with droplets, which are inherent in laser deposition (see, for example, observations for $YBa_2Cu_3O_7$ films [20]).

4. Thus, we managed to obtain quality MgB_2 films on single crystal sapphire substrates using a unique laboratory system of magnetron sputtering and new composite Mg–MgB_2 targets. In their superconducting characteristics, the films corresponded to the best MgB_2 films obtained *in situ* using pulsed laser deposition. The fact that the relatively low critical temperature of our films was the same as in other *in situ* films (about 24 K) suggests the occurrence of a unique mechanism that limits the critical temperature in all such films regardless of the preparation method. It is possible that the small grain size found in this case is an essential factor here. This size, as evident from the constancy of $\rho(T)$ above T_c, is smaller than the mean free path of electrons. The main advantage of our films is their high uniformity, which is inherent in the plasma deposition technique. This uniformity is confirmed by the observation of magnetic field penetration in these films by the magneto-optical technique.

The authors are grateful to V.V Kolyshev for carrying out the synthesis of targets, to V.N. Shilov for technical help in film deposition, to I.I. Zver’kova and G.E. Abrosimova for help in X-ray studies, and to V.A. Oboznov for participation in resistive measurements. The authors are also grateful to Prof. V.V. Ryazanov for help in the organization of this work and discussion of its results.

This work was supported by the State Program of the Russian Federation “Topical Directions in Condensed Matter Physics,” direction “High-T_c Superconductivity.”

REFERENCES

1. J. Nagamatsu, N. Nakagawa, T. Muranaka, *et al.*, Nature **410**, 63 (2001).
2. D. C. Larbalestier, M. O. Rikel, L. D. Cooley, *et al.*, Nature **410**, 186 (2001); cond-mat/0102216.
3. P. C. Canfield, D. K. Finnemore, S. L. Bud’ko, *et al.*, Phys. Rev. Lett. **86**, 2423 (2001); cond-mat/0102289.

4. W. N. Kang, H.-J. Kim, E.-M. Choi, *et al.*, cond-mat/0103179 (2001); Science (2001) (in press); cond-mat/0104266.
5. A. Brinkman, D. Mijatovic, G. Rijnders, *et al.*, cond-mat/0103198; Physica C (Amsterdam) **353**, 1 (2001).
6. C. B. Eom, M. K. Lee, J. H. Choi, *et al.*, cond-mat/0103425; submitted to Nature.
7. H. M. Christen, H. Y. Zhai, C. Cantoni, *et al.*, cond-mat/0103478; submitted to Physica C.
8. S. R. Shindle, S. B. Ogale, R. L. Greene, *et al.*, cond-mat/0103542.
9. D. H. A. Blank, H. Hilgenkamp, A. Brinkman, *et al.*, cond-mat/0103543.
10. M. Paranthaman, C. Cantoni, H. Y. Zhai, *et al.*, cond-mat/0103569; submitted to Appl. Phys. Lett.
11. G. Grassano, W. Ramadan, V. Ferrando, *et al.*, cond-mat/0103572.
12. H. Y. Zhai, H. M. Christen, L. Zhang, *et al.*, cond-mat/0103588; submitted to Appl. Phys. Lett.
13. H. Y. Zhai, H. M. Christen, L. Zhang, *et al.*, cond-mat/0103618; submitted to Nature.
14. S. H. Moon, J. H. Yun, H. N. Lee, *et al.*, cond-mat/0104230.
15. A. V. Pronin, A. Pimenov, A. Loidl, and S. I. Krasnosvobodtsev, cond-mat/0104291.
16. V. A. Gasparov, N. S. Sidorov, I. I. Zver'kova, and M. P. Kulakov, Pis'ma Zh. Éksp. Teor. Fiz. **73**, 601 (2001) [JETP Lett. **73** (2001)]; cond-mat/0104323.
17. L. A. Dorosinskii, M. V. Indenbom, V. I. Nikitenko, *et al.*, Physica C (Amsterdam) **203**, 149 (1992).
18. M. R. Koblischka and R. J. Wijngaarden, Supercond. Sci. Technol. **8**, 199 (1995).
19. E. H. Brandt, M. V. Indenbom, and A. Forkl, Europhys. Lett. **22**, 735 (1993).
20. Th. Schuster, M. V. Indenbom, M. R. Koblischka, *et al.*, Phys. Rev. B **49**, 3443 (1994).
21. T. H. Johansen, M. Baziljevich, D. V. Shantsev, *et al.*, cond-mat/0104113; submitted to Nature.

Translated by A. Bagatur'yants

JETP Letters, Vol. 73, No. 10, 2001, pp. 562–565. From Pis’ma v Zhurnal Éksperimental’noĭ i Teoreticheskoĭ Fiziki, Vol. 73, No. 10, 2001, pp. 631–634.
Original English Text Copyright © 2001 by Osipov, Kochetov.

Dirac Fermions on Graphite Cones[1]

V. A. Osipov and E. A. Kochetov

Joint Institute for Nuclear Research, Bogoliubov Laboratory of Theoretical Physics, Dubna,
Moscow region, 141980 Russia
e-mail: osipov@thsun1.jinr.ru
e-mail: kochetov@thsun1.jinr.ru

Received April 17, 2001

The electronic structure of graphitic cones is investigated within the self-consistent field-theory model. The local and total density of states near the apex are found for cones of different opening angles. For extended electronic states, the total density of states is found to vanish at the Fermi level at any opening angles more than 60°. In turn, for power-law localized states, normalized zero-energy modes are shown to emerge. © *2001 MAIK “Nauka/Interperiodica”.*

PACS numbers: 73.20.At; 73.61.Wp

The recently achieved atomic resolution of scanning tunneling microscopy provides further progress in experimental study of graphitic nanoparticles giving important information about electronic states of sample surfaces. Of special interest are graphitic cones where peculiar electronic states (due to topological defects in their apexes) were theoretically predicted [1, 2]. In particular, an analysis within the effective-mass theory shows that specific superstructures induced by pentagon defects can appear with the wave functions decaying as $r^{-1/5}$ [1]. An important conclusion made in [1] is that these superstructures are not the interference pattern of extended Bloch waves. On the other hand, the continuum model suggested in [2] predicts apical enhancement of density of states at the Fermi energy (E_F) in the vicinity of the apex for cones with 120° disclinations. The states contributing to the nonzero density of states at E_F are found to be the extended states. This result looks rather unexpected (as is known, only the cone with 60° opening angle is distinctive from the geometrical point of view), thus provoking our interest to reconsider the problem within a recently formulated self-consistent gauge model of disclinations on fluctuating elastic surfaces [3]. This model was also adapted for description of electronic states of a fullerene molecule in [4], where the normalized zero-energy states (at E_F) were found. Notice that specific electronic states at the Fermi level due to disclinations are similar to the fermion zero modes in topologically nontrivial manifolds which have been of current interest both in field theory and condensed matter physics (see, e.g., [5–7]).

Before proceeding, it is necessary to make two important remarks. First, conical morphologies have been observed not only for graphite but also for other layered materials like boron nitride and aluminosilicates. It is intriguing that a departure from a flat surface can be solely determined by the topological defect located at the apex of a cone. In other words, a cone structure is formed when a pentagon is introduced into a graphite sheet. To gain a better understanding, one can imagine a cut-and-glue procedure in which the pentagon in the hexagonal network is constructed by cutting out a 60° sector from a graphene (a single layer of graphite) sheet. In this context, pentagonal defects in cones can be considered as apical disclinations and the opening angle is directly connected to the Frank index of a disclination (see below).

Second, the field-theory models for Dirac fermions on hexatic surfaces were formulated earlier to describe electronic structure of variously shaped carbon materials: fullerenes [4, 8], nanotubes [9], and cones [2]. The basic element for all these models is the self-consistent effective-mass theory for a description of electron dynamics in the vicinity of impurity in graphite intercalation compounds [10]. The most important fact found in [10] is that the electronic spectrum of a single graphite plane linearized around the corners of the hexagonal Brillouin zone coincides with that of the Dirac equation in (2 + 1) dimensions. In our approach, both electrons and disclinations are considered in the curved two-dimensional background. Thus, we formulate the Dirac equation on a cone with the flux due to pentagonal apical disclination represented by an abelian gauge field.

To start, let us briefly discuss a relevant geometrical background. In the polar coordinates $(r, \varphi) \in R^2$, a cone

---

[1] This article was submitted by the authors in English.

can be regarded as an embedding

$$(r, \varphi) \longrightarrow (ar\cos\varphi, ar\sin\varphi, cr),$$
$$0 < r < 1, \quad 0 \le \varphi < 2\pi,$$

with a and c being the cone parameters. From this, the components of the induced metric can be easily read off:

$$g_{rr} = a^2 + c^2, \quad g_{\varphi\varphi} = a^2 r^2, \quad g_{r\varphi} = g_{\varphi r} = 0. \qquad (1)$$

The opening angle of a cone, θ, is determined by $\sin(\theta/2) = a/\sqrt{a^2 + c^2}$. Since the cone itself appears when one or more sectors are removed from a graphene, all the possible disclination angles, ω, are divisible by 60°. Thus, the Frank index, ν ($\nu = \omega/2\pi$), of the apical disclination can be specified by $\nu = 1 - \sin(\theta/2)$. At $\nu = 0$, one gets a flat graphene sheet ($\theta = 180°$). For $\nu = 1/6$ (60° disclination), $\nu = 1/3$ (120° disclination), and $\nu = 1/2$ (180° disclination), one obtains $\theta = 112.9°$, 83.6°, 60°, respectively. For convenience, we introduce a parameter $\chi = 1 + c^2/a^2$, so that $\sin(\theta/2) = 1/\sqrt{\chi} = 1 - \nu$.

The basic field equation for the $U(1)$ gauge field in a curved background reads

$$D_\mu F^{\mu k} = 0, \quad F^{\mu k} = \partial^\mu W^k - \partial^k W^\mu, \qquad (2)$$

where covariant derivative $D_\mu := \partial_\mu + \Gamma_\mu$ includes the Levi-Civita (torsion-free, metric compatible) connection

$$\Gamma^k_{\mu\lambda} := (\Gamma_\mu)^k_\lambda = \frac{1}{2} g^{kl}\left(\frac{\partial g_{l\lambda}}{\partial x^\mu} + \frac{\partial g_{\mu l}}{\partial x^\lambda} - \frac{\partial g_{\mu\lambda}}{\partial x^l}\right),$$

$g_{\mu k}$ being the metric tensor on a Riemannian surface Σ with local coordinates (x^1, x^2). For a single disclination on an arbitrary elastic surface, a singular solution to Eqs. (2) is found to be [3]

$$W^k = -\nu\varepsilon^{k\lambda} D_\lambda G(x^1, x^2), \qquad (3)$$

where

$$D_\mu D^\mu G(x^1, x^2) = 2\pi\delta^2(x^1, x^2)/\sqrt{g}, \qquad (4)$$

with $\varepsilon_{\mu k} = \sqrt{g}\,\epsilon_{\mu k}$ being the fully antisymmetric tensor on Σ, $\epsilon_{12} = -\epsilon_{21} = 1$. It should be mentioned that Eqs. (2) and (4) self-consistently describe a defect located on an arbitrary surface [3].

From Eqs. (3) and (4), the following solution can be obtained:

$$W^r = 0, \quad W^\varphi = -\nu\varepsilon^{\varphi r}\partial_r G, \quad G = \sqrt{\chi}\log r. \qquad (5)$$

As a result, $W^\varphi = (\nu/r)\sqrt{\chi/g}$ and $W_\varphi = \nu$.

To incorporate fermions, we need a set of orthonormal frames $\{e_\alpha\}$ which yield the same metric, g, each of which is related to the other by the local $SO(2)$ rotation,

$$e_\alpha \longrightarrow e'_\alpha = \Lambda^\beta_\alpha e_\beta, \quad \Lambda^\beta_\alpha \in SO(2).$$

It then follows that $g_{\mu\nu} = e^\alpha_\mu e^\beta_\nu \delta_{\alpha\beta}$, where e^μ_α is the zweibein, with the orthonormal frame indices being $\alpha, \beta = \{1, 2\}$ and the coordinate indices being $\mu, \nu = \{r, \varphi\}$. Explicitly, one may choose the only nonzero components to be $e^1_r = \sqrt{a^2 + c^2}$ and $e^2_\varphi = ar$. Notice that e^μ_α is the inverse of e^α_μ.

The Dirac equation on a cone takes the form (E_F is chosen to be zero)

$$H\psi := i\gamma^\alpha e^\mu_\alpha(\nabla_\mu + iW_\mu)\psi = E\psi, \qquad (6)$$

where $\nabla_\mu = \partial_\mu + \Omega_\mu$, with

$$\Omega_\mu = -\frac{1}{8}\Gamma^{\alpha\ \beta}_{\ \mu}[\gamma_\alpha, \gamma_\beta]$$

being the spin connection term, which, as is known, does not contribute to the Dirac equation if dim Σ = 2 [11].

In 2D, the Dirac matrices can be chosen to be the Pauli matrices: $\gamma^1 = -\sigma^2$, $\gamma^2 = \sigma^1$. For massless fermions, σ^3 serves as a conjugation matrix, and the energy eigenmodes are symmetric about $E = 0$ ($\sigma^3\psi_E = \psi_{-E}$). Generator of the local Lorentz transformations Λ takes the form $-i\partial_\varphi$, whereas the generator of the Dirac spinor transformations $\rho(\Lambda)$ is

$$\Sigma_{12} = \frac{i}{4}[\gamma_1, \gamma_2] = \frac{1}{2}\sigma^3.$$

Total angular momentum of a 2D Dirac system is, therefore,

$$L_z = -i\partial_\varphi + \frac{1}{2}\sigma^3,$$

which commutes with the Hamiltonian (6). Consequently, the eigenfunctions are classified with respect to the eigenvalues of $J_z = j + 1/2$, $j = 0, \pm1, \pm2, \ldots$, and are to be taken in the form

$$\psi = \begin{pmatrix} u(r)e^{i\varphi j} \\ v(r)e^{i\varphi(j+1)} \end{pmatrix}. \qquad (7)$$

In this case, Eq. (6) reduces to the pair

$$\begin{aligned} \partial_r u - \frac{\sqrt{\chi}(j+\nu)}{r}u &= \tilde{E}v, \\ -\partial_r v - \frac{\sqrt{\chi}(j+1+\nu)}{r}v &= \tilde{E}u, \end{aligned} \qquad (8)$$

where $\tilde{E} = \sqrt{\chi}aE$. The most distinctive feature of Eq. (8) in comparison with the alternative model given in [2] is the appearance of the factor χ which characterizes geometry of a cone [cf. Eq. (5) from that paper]. This plays a decisive role in the following consideration and finally leads to the remarkably different results. A general solution to Eq. (8) is found to be

$$\begin{pmatrix} u \\ v \end{pmatrix} = Ar^{\xi}\begin{pmatrix} J_{\eta}(\tilde{E}r) \\ \pm J_{\bar{\eta}}(\tilde{E}r) \end{pmatrix} \qquad (9)$$

with $\xi = (1 - \sqrt{\chi})/2$, $\eta = \pm(\sqrt{\chi}(j + \nu + 1/2) - 1/2)$, and $\bar{\eta} = \pm(\sqrt{\chi}(j + \nu + 1/2) + 1/2)$. A is a normalization factor. Thus, there are two independent solutions with $\eta(\bar{\eta}) > 0$ and $\eta(\bar{\eta}) < 0$. Notice also that signs ± in Eq. (9) correspond to states with $E > 0$ and $E < 0$, respectively. Due to the above-mentioned symmetry properties, one can consider either case, for instance, $E > 0$.

The important restrictions come from the normalization condition

$$\int(|u|^2 + |v|^2)\sqrt{g}dx^1dx^2 = 1, \qquad (10)$$

which in view of Eq. (9) takes the form

$$2\pi\sqrt{\chi}a^2A^2\int_0^1 r^{2\xi+1}(J_{\eta}^2(\tilde{E}r) + J_{\bar{\eta}}^2(\tilde{E}r))dr = 1. \qquad (11)$$

The normalization factor can be deduced from the asymptotic formula for Bessel functions at large arguments. Indeed, in our case, $\bar{\eta} - \eta = 1$, so that $J_{\eta}^2 + J_{\bar{\eta}}^2 \longrightarrow 2/\pi\tilde{E}r$ for $\tilde{E}r \gg 1$. Substituting this into Eq. (11) yields $A^2 = (2\xi + 1)E/4a$. Additionally, a restriction in the form $2\xi > -1$ (i.e., $\nu < 1/2$) serves to avoid divergence in Eq. (11). This means that solution (9) is appropriate only for cones with opening angles more than 60°. At the same time, Eq. (11) must be nonsingular at small r. This imposes a restriction on possible values of j. Namely, for $\eta, \bar{\eta} > 0$, one gets $j > -1$ (i.e., $j = 0, 1, 2, \ldots$), while for $\eta, \bar{\eta} < 0$ one has $j < -2\nu$ ($j = -1, -2, \ldots$). As is seen, possible values of j are not overlapped at any ν.

We are interested in the electron states near the apex of a cone. As it follows directly from Eq. (9), for small r the wave functions behave as

$$\begin{aligned} \begin{pmatrix} u \\ v \end{pmatrix} &\sim \begin{pmatrix} E^{1/2+\eta}r^{\xi+\eta} \\ E^{1/2+\bar{\eta}}r^{\xi+\bar{\eta}} \end{pmatrix}, \quad \eta, \bar{\eta} > 0, \\ \begin{pmatrix} u \\ v \end{pmatrix} &\sim \begin{pmatrix} E^{1/2-\eta}r^{\xi-\eta} \\ E^{1/2-\bar{\eta}}r^{\xi-\bar{\eta}} \end{pmatrix}, \quad \eta, \bar{\eta} < 0. \end{aligned} \qquad (12)$$

To the leading order, one obtains

$$\Psi \sim E^{(1-2\nu)/2(1-\nu)}r^{-\nu/(1-\nu)}.$$

In particular, for $\nu = 0$, 1/6, 1/3, we get $\Psi \sim \sqrt{E}$, $\Psi \sim E^{2/5}r^{-1/5}$, and $\Psi \sim E^{1/4}r^{-1/2}$, respectively.

Since the local density of states diverges as $r \longrightarrow 0$, it is more relevant to consider the total density of states on a patch $0 < r \le \delta$ for small δ. To this end, one has to integrate the electron density over a small disk and to divide the result by $\Delta k = \pi/a$, which is the spacing of k values. The result is

$$D(E, \delta) \propto \begin{cases} E^{(1+2\nu)/(1-\nu)}\delta^{2/(1-\nu)}, & \eta, \bar{\eta} > 0 \\ E^{(1-2\nu)/(1-\nu)}\delta^{2(1-2\nu)/(1-\nu)}, & \eta, \bar{\eta} < 0. \end{cases} \qquad (13)$$

It should be stressed that according to Eq. (13) a specific behavior of $D(E, \delta)$ takes place only for $\nu = 1/2$ where $D \sim E^0\delta^0$. Thus, this prediction of our model agrees well with the earlier remark that it is the 60° opening angle (180° sector is removed from the flat graphene sheet) which is distinctive from the geometrical point of view. What is also important, in accordance with Eq. (13), there are no extended states with the nonzero density of states at E_F (recall that the case $\nu = 1/2$ is beyond the scope of our consideration). This conclusion markedly disagrees with the results obtained in [2]. As we show below, only power-law localized zero-energy states can exist. In the leading order, one obtains from Eq. (13)

$$D(E, \delta) \propto \begin{cases} E\delta^2, & \nu = 0 \\ E^{4/5}\delta^{8/5}, & \nu = 1/6 \\ E^{1/2}\delta, & \nu = 1/3. \end{cases} \qquad (14)$$

It is interesting that the model [2] predicts the same δ dependence, while the E dependence is completely different.

To study the electron states at the Fermi energy, one has to return to Eq. (8) and set $E = 0$. The solution reads

$$u_0 = Ar^{\alpha}, \quad v_0 = Br^{-(\alpha + \sqrt{\chi})}. \qquad (15)$$

Here, A and B are the normalization factors. A simple analysis shows that either u_0 or v_0 are normalizable on a cone of finite size. Thus, one can construct self-conjugate solutions $\begin{pmatrix} u_0 \\ 0 \end{pmatrix}$ and $\begin{pmatrix} 0 \\ v_0 \end{pmatrix}$. The first solution is nonsingular, and, in the leading order, the electron density behaves as $|u_0|^2 \sim r^{\beta}/a^2$ with $\beta = 2\nu/(1 - \nu)$. The second solution is singular, $|v_0|^2 \sim r^{-\beta}/a^2$. As before, in this case one can consider the total density of states for comparison to experiments. For our purposes, we dwell on the analysis of the case $\nu = 1/6$. As is seen, for $\nu = 1/6$, one gets $v_0 \sim r^{-1/5}$ and, accordingly, $D \sim \delta^{8/5}$. This is in a good agreement with the results obtained in [1]. Thus, our study confirms the results of [1, 12] that the states contributing to the nonzero density of states at the Fermi energy are power-law localized. Notice also that in monolayer graphite ($\nu = 0$) of infinite length

($a \longrightarrow \infty$) there are no localized zero-energy electronic states on disclinations. It should be emphasized that this conclusion agrees with the results of numerical calculations [12] where the local density of states at the Fermi level was found to be zero for the case of five-membered rings (pentagons).

In conclusion, we have formulated a self-consistent field-theory model to describe electronic states on a graphitic cone. The topological nature of the apical defect is found to markedly modify the low-energy electronic structure. In particular, the total density of extended states has a rather specific dependence on both energy and a distance from the apex of a cone. In contrast to [2], we predict that there are no extended states with the nonzero density of states at the Fermi level for any disclinations with $\nu < 1/2$. At the same time, we found that powerlike localized states can exist at the Fermi level in accordance with [1, 12]. It would be interesting to verify our conclusions in scanning tunneling microscope experiments with graphitic cones.

This work was supported by the Science and Technology Department of Moscow region and the Russian Foundation for Basic Research, project no. 01-02-97021.

REFERENCES

1. K. Kobayashi, Phys. Rev. B **61**, 8496 (2000).
2. P. E. Lammert and V. H. Crespi, Phys. Rev. Lett. **85**, 5190 (2000).
3. E. A. Kochetov and V. A. Osipov, J. Phys. A **32**, 1961 (1999).
4. V. A. Osipov and E. A. Kochetov, Pis’ma Zh. Éksp. Teor. Fiz. **72**, 285 (2000) [JETP Lett. **72**, 199 (2000)].
5. R. Jackiw, Phys. Rev. D **29**, 2375 (1984).
6. G. E. Volovik, Pis’ma Zh. Éksp. Teor. Fiz. **63**, 729 (1996) [JETP Lett. **63**, 763 (1996)].
7. G. E. Volovik, Pis’ma Zh. Éksp. Teor. Fiz. **70**, 601 (1999) [JETP Lett. **70**, 609 (1999)].
8. J. González, F. Guinea, and M. A. H. Vozmediano, Phys. Rev. Lett. **69**, 172 (1992).
9. C. L. Kane and E. J. Mele, Phys. Rev. Lett. **78**, 1932 (1997).
10. D. P. Di Vincenzo and E. J. Mele, Phys. Rev. B **29**, 1685 (1984).
11. M. Nakahara, *Geometry, Topology, and Physics* (A. Hilger, Bristol, 1990).
12. R. Tamura and M. Tsukada, Phys. Rev. B **49**, 7697 (1994); **52**, 6015 (1995).

JETP Letters, Vol. 73, No. 10, 2001, pp. 566–569. Translated from Pis'ma v Zhurnal Éksperimental'noĭ i Teoreticheskoĭ Fiziki, Vol. 73, No. 10, 2001, pp. 635–639.
Original Russian Text Copyright © 2001 by Batyev.

A Model of Wigner Liquid

É. G. Batyev
Institute of Semiconductor Physics, Siberian Division, Russian Academy of Sciences,
pr. Akademika Lavrent'eva 13, Novosibirsk, 630090 Russia
e-mail: batyev@isp.nsc.ru

Received March 6, 2001; in final form, April 19, 2001

A two-dimensional low-density system of charge carriers with strong Coulomb interaction, which can lead to the appearance of a short-wavelength soft mode (precursor of crystallization) is examined. This system provides elementary excitations of two types: Fermi excitations and Bose excitations with a gap in the spectrum. The latter excitations are similar to rotons in superfluid helium. A model involving the Fermi liquid and the soft mode is proposed, and interaction of different excitations with each other is described phenomenologically as in the Landau theory of Fermi liquid. By solving the derived equations, it was found that, as the temperature increases, the effective mass of Fermi excitations decreases and the gap in the Bose excitation spectrum increases. *© 2001 MAIK "Nauka/Interperiodica".*

PACS numbers: 71.27.+a; 71.10.Ay

An unusual behavior of conductivity in two-dimensional systems as a function of the temperature and density of charge carriers was experimentally found by Kravchenko *et al.* [1]. Later, similar results were obtained in other experiments (see, e.g., [2–7] and review [8]). Various mechanisms were proposed to explain these dependences (see, e.g., [8–10]). One of the recent attempts was made in [11], where the correlation effects received primary attention. The essence is that correlations in the positions of carriers in a system with Coulomb interaction become substantial at sufficiently low densities and, finally, lead to the formation of a Wigner crystal. A liquid preceding this crystal is sometimes called a Wigner liquid. The so-called soft mode corresponding to low-energy Bose particles can arise in this liquid. In the previous simplest formulation [11], I analyzed how these excitations can affect the conductivity of the system. What is the role of the interaction of these particles with each other and with Fermi excitations? This interaction cannot be described by, e.g., perturbation theory. In this work, I attempt to take it into account phenomenologically as in the Landau Fermi liquid theory.

The basic assumption is that the system has a soft mode at a nonzero momentum value. This is possible at various structural transitions, e.g., when the period of a crystal is doubled. The simplest example is an antiferromagnet in a strong magnetic field [12] near the instability point of a completely polarized state. This can also occur when a system is crystallized through the phase transition, which is close to a second-order phase transition [13]. The system under consideration was compared with ^{3}He in [11] in order to clarify what can be expected for the case we analyzed (various possibilities for ^{3}He were discussed in [13, 14]).

Spivak [15] suggested and used the closer analogy of the two-dimensional electron system with ^{3}He, but the soft mode was not introduced in an explicit form. This is a different approach, and results of [15] relate to other characteristics than my results.

I propose a model involving the Fermi liquid and the soft mode, which is assumed to be spin-independent as in [13], although another variant (as in [14]) is also possible. But as the density decreases, mutual localization of electrons due to the Coulomb interaction increases (as in a Wigner crystal) and, therefore, overlap integrals and exchange interaction decrease, so that the spin effects should become of secondary importance. This is the reason for the above-proposed assumption.

Model. In the Landau Fermi liquid theory, as the distribution function varies by $\delta n_{\mathbf{p}}$, the energy of the system changes by

$$\delta E_L = \sum_{\mathbf{p}} \epsilon_{\mathbf{p}} \delta n_{\mathbf{p}} + \frac{1}{2V} \sum_{\mathbf{p},\mathbf{p}'} \delta n_{\mathbf{p}} f(\mathbf{p}, \mathbf{p}') \delta n_{\mathbf{p}'}, \qquad (1)$$

where $\epsilon_{\mathbf{p}}$ is the energy of a quasiparticle with the momentum $\mathbf{p}$; V is the volume (area) of the system; $f(\mathbf{p}, \mathbf{p}')$ is the interaction function of Fermi quasiparticles, which below will be called fermions; and the summation with respect to the spin indices along with the summation with respect to momenta is implied hereafter. This representation also applies to a homogeneous system of charged particles, whereas corresponding Coulomb contributions should be taken into account for an inhomogeneous system.

Then, the soft-mode effects should be taken into account. The energy of the corresponding Bose particles is represented in the operator form

$$H_0 = \sum_{\mathbf{q}} \Omega_{\mathbf{q}} b^+_{\mathbf{q}} b_{\mathbf{q}}, \quad \Omega^2_{\mathbf{q}} = \Omega^2_0 + v^2_0 (q - q_0)^2, \qquad (2)$$

where $\Omega_{\mathbf{q}}$ is the boson energy at absolute zero and $b^+_{\mathbf{q}}(b_{\mathbf{q}})$ is the operator of creation (annihilation) of a boson with the momentum $\mathbf{q}$.

The interaction of bosons with fermions is written as

$$H_0 = \frac{1}{V}\sum_{\mathbf{p},\mathbf{q}} \delta n_{\mathbf{q}} U(\mathbf{p}, \mathbf{q}) B_{\mathbf{q}} B_{-\mathbf{q}}, \quad B_{\mathbf{q}} = \frac{b_{\mathbf{q}} + b^+_{-\mathbf{q}}}{\sqrt{\Omega_{\mathbf{q}}}}, \qquad (3)$$

where $B_{\mathbf{q}}$ is, to an insignificant factor, the coordinate of the corresponding oscillator. Here, it is reasonable to represent this interaction energy in terms of the oscillator coordinate rather than in terms of the oscillator excitation degree (the number of bosons).

Hamiltonian (3) causes, in particular, the temperature dependence of the fermion spectrum $\delta\epsilon_{\mathbf{p}}$:

$$\delta\epsilon_{\mathbf{p}} = \frac{1}{V}\sum_{\mathbf{q}} U(\mathbf{p}, \mathbf{q}) \langle B_{\mathbf{q}} B_{-\mathbf{q}} \rangle, \qquad (4)$$

where $\langle \ldots \rangle$ means averaging over the state of the system, e.g., over the equilibrium state at nonzero temperature. Within the same accuracy, the correction δf to the interaction function of fermions is written as

$$\delta f(\mathbf{p}, \mathbf{p}') = \frac{1}{V}\sum_{\mathbf{q}} g(\mathbf{p}, \mathbf{p}'; \mathbf{q}) \langle B_{\mathbf{q}} B_{-\mathbf{q}} \rangle. \qquad (5)$$

The energy of interaction between bosons is represented in the following form that is completely similar to Eq. (1) but, as well as Eq. (3), involves the oscillator coordinates:

$$\langle H_2 \rangle = \frac{1}{2V}\sum_{\mathbf{q},\mathbf{q}'} \langle B_{\mathbf{q}} B_{-\mathbf{q}} \rangle \lambda(\mathbf{q}, \mathbf{q}') \langle B_{\mathbf{q}'} B_{-\mathbf{q}'} \rangle.$$

In the operator form, which is convenient for determining the boson spectrum, this interaction is represented as

$$\begin{aligned} H_2 &= \frac{1}{V}\sum_{\mathbf{q},\mathbf{q}'} B_{\mathbf{q}} B_{-\mathbf{q}} \lambda(\mathbf{q}, \mathbf{q}') \langle B_{\mathbf{q}'} B_{-\mathbf{q}'} \rangle \\ &- \frac{1}{2V}\sum_{\mathbf{q},\mathbf{q}'} \langle B_{\mathbf{q}} B_{-\mathbf{q}} \rangle \lambda(\mathbf{q}, \mathbf{q}') \langle B_{\mathbf{q}'} B_{-\mathbf{q}'} \rangle. \end{aligned} \qquad (6)$$

The above approach has an obvious disadvantage: it is not evident from it both types of excitations are related to the same system of carriers. This would be manifested as follows: if the system moves with the velocity $\mathbf{u}$, the boson spectrum changes as

$$\Omega_{\mathbf{q}} \longrightarrow \Omega_{\mathbf{q}} + \mathbf{qu}.$$

Let us introduce additional interaction between two types of quasiparticles so as to insure the required result at absolute zero:

$$H_3 = \frac{1}{V}\sum_{\mathbf{p},\mathbf{q}} \delta n_{\mathbf{p}} \frac{(\mathbf{pq})}{mn} b^+_{\mathbf{q}} b_{\mathbf{q}}, \quad n = \frac{p^2_{\mathrm{F}}}{2\pi}, \qquad (7)$$

where n and m are the density and mass of the carriers, respectively. Joint application of Eqs. (2) and (7) gives the correct result. However, this is insufficient in the general case. Indeed, Eq. (7) indicates that the boson spectrum depends only on the fermion momentum, but it is reasonable to expect that this spectrum depends on the total momentum of the system. To insure this dependence, it is necessary to introduce the corresponding additional term

$$\begin{aligned} H_4 &= \frac{1}{V}\sum_{\mathbf{q},\mathbf{q}'} \langle b^+_{\mathbf{q}'} b_{\mathbf{q}'} \rangle \frac{(\mathbf{q}'\mathbf{q})}{mn} b^+_{\mathbf{q}} b_{\mathbf{q}} \\ &- \frac{1}{2V}\sum_{\mathbf{q}',\mathbf{q}} \langle b^+_{\mathbf{q}'} b_{\mathbf{q}'} \rangle \frac{(\mathbf{q}'\mathbf{q})}{mn} \langle b^+_{\mathbf{q}} b_{\mathbf{q}} \rangle, \end{aligned} \qquad (8)$$

where, as well as in Eq. (6), the operator representation is used. We emphasize that Eqs. (7) and (8) along with Eq. (1) provide the momentum dependence of the energy of the system in the form that would be expected in the general case: it is sufficient to consider nonequilibrium initial distribution functions of fermions and bosons in the absence of the dissipation of the momentum of the system admitting the possibility of establishing thermal equilibrium within the system.

Let us consider the parameters determining initial boson spectrum (2). The momentum q_0 can be estimated as follows: for given density of the carriers, one should consider, e.g., a triangular lattice and determine the reciprocal lattice vector whose magnitude corresponds to q_0. We turn now to the Ω_0 value. Let us introduce the characteristic time for fermions $t_{\mathrm{F}} \sim 1/\epsilon_{\mathrm{F}}(0)$, where $\epsilon_{\mathrm{F}}(0) \sim v_{\mathrm{F}}(0)$ is the Fermi energy at zero temperature, $v_{\mathrm{F}}(0)$ is the Fermi velocity at zero temperature, and p_{F} is the Fermi momentum. The time t_{F} is about the time of flight of an average distance between carriers. For $t \ll t_{\mathrm{F}}$, the system more likely behaves as an amorphous solid with crystalline short-range order rather than as a liquid. For $t > t_{\mathrm{F}}$, the system behaves as a liquid (similar problems were discussed, e.g. in [15]). Therefore, if the soft mode exists in a liquid phase, its characteristic frequency should be sufficiently small, $\Omega_0 < \epsilon_{\mathrm{F}}(0)$, because the system cannot behave as a liquid at high frequencies. This value is small compared to the interaction, but even stronger inequality can be assumed, and, in this case, the soft mode is manifested on the Fermi scale. The v_0 value is likely to be $v_0 \sim v_{\mathrm{F}}(0)$. In summary, we have

$$q_0 \approx \nu 2 p_{\mathrm{F}}, \quad \nu = (\pi/\sqrt{3})^{1/2}; \qquad (9)$$
$$v_0 \sim v_{\mathrm{F}}(0); \quad \Omega_0 \ll \epsilon_{\mathrm{F}}(0).$$

Equations (1)–(8) specify the model. In this study, only equilibrium properties will be considered and, therefore, Eqs. (7) and (8) will not be used.

Properties. For nonzero temperatures or with changing density of carriers, the boson spectrum is renormalized due to interactions (3) and (6). This spectrum is found by solving the problem with the Hamiltonian

$$H_0 + H_1 + H_2 \longrightarrow H$$
$$= \sum_{\mathbf{q}} \left(\Omega_{\mathbf{q}} b_{\mathbf{q}}^{+} b_{\mathbf{q}} + \frac{\Delta_{\mathbf{q}}^2}{4\Omega_{\mathbf{q}}} (b_{\mathbf{q}} + b_{-\mathbf{q}}^{+})(b_{-\mathbf{q}} + b_{\mathbf{q}}^{+}) \right), \qquad (10)$$

$$\Delta_{\mathbf{q}}^2 = \frac{4}{V} \sum_{\mathbf{p}} U(\mathbf{p}, \mathbf{q}) \delta n_{\mathbf{p}} + \frac{4}{V} \sum_{\mathbf{k}} \lambda(\mathbf{q}, \mathbf{k}) \langle B_{\mathbf{k}} B_{-\mathbf{k}} \rangle. \qquad (11)$$

In Eq. (10), an immaterial constant term is omitted, and, in Eq. (11), we ignore a term that is related to Eq. (5) and is *a priori* small at low temperatures because it involves the square of a change in the fermion distribution function.

Hamiltonian (10) is diagonalized by means of the Bogoliubov (u, v) transformation

$$b_{\mathbf{q}} = u_{\mathbf{q}} \beta_{\mathbf{q}} + v_{\mathbf{q}} \beta_{-\mathbf{q}}^{+}, \quad u_{\mathbf{q}}^2 - v_{\mathbf{q}}^2 = 1, \qquad (12)$$

where $\beta_{\mathbf{q}}^{+}$ and $\beta_{\mathbf{q}}$ are the operators of a quasiparticle (renormalized boson). Simple calculation yields

$$H = \sum_{\mathbf{q}} \omega_{\mathbf{q}} \beta_{\mathbf{q}}^{+} \beta_{\mathbf{q}} + \frac{1}{2} \sum_{\mathbf{q}} (\omega_{\mathbf{q}} - \Omega_{\mathbf{q}}), \qquad (13)$$
$$\omega_{\mathbf{q}}^2 = \Omega_{\mathbf{q}}^2 + \Delta_{\mathbf{q}}^2.$$

The (u, v)-transformation coefficients are determined by the expressions

$$u_{\mathbf{q}}^2 = \frac{1}{2} \left(\frac{\Omega_{\mathbf{q}}^2 + \Delta_{\mathbf{q}}^2/2}{\omega_{\mathbf{q}} \Omega_{\mathbf{q}}} + 1 \right), \quad u_{\mathbf{q}} v_{\mathbf{q}} = \frac{-\Delta_{\mathbf{q}}^2}{4 \omega_{\mathbf{q}} \Omega_{\mathbf{q}}}. \qquad (14)$$

It is easy to see that Eqs. (7) and (8) are represented in terms of the quasiparticle operators through similar expressions, i.e., by replacing $b_{\mathbf{q}}^{+} b_{\mathbf{q}} \longrightarrow \beta_{\mathbf{q}}^{+} \beta_{\mathbf{q}}$.

We first analyze Eq. (11) for zero temperature. In this case, simple consideration provides a relation between various model parameters. Below, we will use the following expansion in small deviations of the angle-averaged interaction [see Eqs. (3), (11)]:

$$\overline{U(\mathbf{p}, \mathbf{q})} \approx U_0 + U_1 \frac{q - q_0}{q_0} + U_2 \frac{p - p_{\mathrm{F}}}{p_{\mathrm{F}}}. \qquad (15)$$

When the carrier density δn changes, the boson spectrum should change too:

$$\Delta_{\mathbf{q}}^2 = 4 \delta n \overline{U(\mathbf{p}, \mathbf{q})}_{p = p_{\mathrm{F}}} \approx 4 \delta n \left(U_0 + U_1 \frac{q - q_0}{q_0} \right) \qquad (16)$$
$$\equiv \frac{\delta n}{n} [\Omega_1^2 - 2 v_0^2 q_1 (q - q_0)].$$

This expression demonstrates that, as the carrier density increases, the gap in the spectrum and the momentum at the minimum ($q_1 > 0$) increase, as might be expected:

$$\Omega_0^2 \longrightarrow \Omega_0^2 + \frac{\delta n}{n} \Omega_1^2, \quad q_0 \longrightarrow q_0 + \frac{\delta n}{n} q_1.$$

According to Eq. (9), we have $q_1 = \nu p_{\mathrm{F}}$. It is obvious that Ω_1 should be $\sim\Omega_0$. This means that the zeroth harmonic of the quantity U is small if strong inequality (9) is valid for Ω_0. However, the derivatives U_1 and U_2 in the momenta of the zeroth harmonic are not small and take the value

$$U_2 \approx -U_1 = \frac{\nu^2 p_{\mathrm{F}}^2 v_0^2}{n}. \qquad (17)$$

The latter equality is obvious from Eq. (16) and the remarks below it, and the former one is valid because, otherwise, in view of above-mentioned smallness of U_0 and proportionality of q_0 to p_{F}, the small quantity U_0 would considerably change under a relatively small change in the density but this can occur only under a comparable change in the density.

Let us consider the temperature corrections. The boson spectrum changes according to Eq. (11). The average appearing in this equation is calculated by using quasiparticle operators [see Eqs. (12), (14)] and retaining only the temperature-dependent contribution, which vanishes at $T \longrightarrow 0$. We are interested in the values $q \approx k \approx q_0$. Therefore, the result is expressed in terms not of the function $\lambda(\mathbf{q}, \mathbf{k})$ but of its angle-averaged value $\bar{\lambda}$ at the indicated momentum values, and Eq. (11) takes the form

$$\Delta_{\mathbf{q}}^2 = \frac{2}{V} \sum_{\mathbf{p}} \overline{U(\mathbf{p}, \mathbf{q})} \left(\operatorname{sgn} \xi_p - \tanh \frac{\xi_p}{2T} \right)$$
$$+ \frac{4\bar{\lambda}}{V} \sum_{\mathbf{k}} \left[\frac{2N_{\mathbf{k}} + 1}{\omega_{\mathbf{k}}} - \frac{1}{\Omega_{\mathbf{k}}} \right],$$
$$N_{\mathbf{k}} = [\exp(\omega_{\mathbf{k}}/T) - 1]^{-1}.$$

Here, the fermion energy $\xi_p = v_{\mathrm{F}}(p - p_{\mathrm{F}})$, where v_{F} is the Fermi velocity, is measured from the Fermi energy. The fermion spectrum changes too, and Eq. (4) along with Eq. (15) provides the following relation between the effective mass m^* and the effective mass m_0^* at zero temperature:

$$\frac{1}{m_0^*} = \frac{1}{m^*} - \frac{U_2}{p_{\mathrm{F}}^2 V}\sum_{\mathbf{q}}\left(\frac{2N_{\mathbf{q}}+1}{\omega_{\mathbf{q}}} - \frac{1}{\Omega_{\mathbf{q}}}\right).$$

Following the Fermi liquid theory, one can also use the fermion interaction function with additional term (5) and obtain a relation between functions entering into Eqs. (4) and (5).

Going over from summation to integration with respect to energies of corresponding quasiparticles and taking Eq. (15) into account, from the above expressions we obtain

$$\Delta^2 = \left(\frac{m^*}{m_0^*}\right)^2 \alpha T^2 + \omega_1^2 F(\omega_0), \quad \frac{m_0^*}{m^*} = 1 + \gamma F(\omega_0),$$

$$F(\omega_0) \equiv 2\int_{\omega_0}^{\infty} \frac{d\omega}{\sqrt{\omega^2 - \omega_0^2}} \frac{1}{\exp(\omega/T) - 1} - \ln(\omega_0/\Omega_0). \tag{18}$$

Here, since the quantity $\Delta_{\mathbf{q}}$ is independent of the momentum, its argument is omitted and we introduce the notation

$$\alpha = \frac{16U_2(m_0^*)^2}{\pi p_{\mathrm{F}}^2} I, \quad I = \int_0^{\infty} dx x(1 - \tanh(x)) \approx 0.411,$$

$$\gamma = \frac{U_2 m_0^* q_0}{\pi p_{\mathrm{F}}^2 v_0}, \quad \omega_0 = \sqrt{\Omega_0^2 + \Delta^2}, \quad \omega_1^2 = 4q_0\bar{\lambda}/(\pi v_0),$$

where ω_1 is the energy-dimension quantity and it is assumed that $\bar{\lambda} > 0$ as usual for the fourth-order anharmonicity. Taking Eq. (17) into account, one can find the following relation between dimensionless constants γ and α:

$$\frac{\alpha}{\gamma^2} = \frac{2I}{\nu^4}, \quad \gamma = 4\nu^3 v_0/v_{\mathrm{F}}(0). \tag{19}$$

Besides the model formulation, we focused on deriving Eqs. (18), which determine the temperature dependence of the elementary excitation spectra. It was found that the effective fermion mass decreases and the gap in the boson spectrum increases with increasing temperature. This is obvious in the simple limiting case. Let $\omega_0/T \ll 1$, which is possible when $T \gg \Omega_0$ and ω_1 is small enough. In this case, the function $F(\omega_0)$ is approximately calculated and Eqs. (18) yield

$$m^*/m_0^* \approx \omega_0/\gamma\pi T, \quad \omega_0 \approx (\pi\omega_1^2 T)^{1/3}.$$

The problem of conductivity requires an individual analysis. But even now, the following conclusions are evident. Due to the temperature dependence of the spectra, first, fermion–impurity scattering, which depends on the effective mass, will be temperature-dependent and, second, the boson contribution to the resistivity will also change compared to that previously obtained in [11]. The proposed model is an attempt to understand how to take these effects into account.

I am grateful to A.V. Chaplik and M.V. Éntin for stimulating discussion. This work was supported in part by the Russian Foundation for Basic Research (project no. 00-15-96800) and by the Russian State Program "Physics of Solid-State Nanostructures."

REFERENCES

1. S. V. Kravchenko *et al.*, Phys. Rev. B **50**, 8039 (1994); **51**, 7038 (1995); Phys. Rev. Lett. **77**, 4938 (1996).
2. Y. Hanein, U. Meirav, D. Shahar, *et al.*, Phys. Rev. Lett. **80**, 1288 (1998).
3. S. J. Papadakis and M. Shayegan, Phys. Rev. B **57**, R15068 (1998).
4. Jongsoo Yoon, C. C. Li, D. C. Tsui, and M. Shayegan, Phys. Rev. Lett. **84**, 4421 (2000).
5. S. C. Dultz and H. W. Jiang, Phys. Rev. Lett. **84**, 4689 (2000).
6. V. Senz, T. Ihn, T. Heinzel, *et al.*, Phys. Rev. Lett. **85**, 4357 (2000).
7. L. Moldovan, S. Melinte, V. Bayot, *et al.*, Phys. Rev. Lett. **85**, 4369 (2000).
8. E. Abrahams, S. V. Kravchenko, and M. P. Sarachik, Rev. Mod. Phys. **73**, 251 (2001).
9. V. M. Pudalov, Pis'ma Zh. Éksp. Teor. Fiz. **66**, 168 (1997) [JETP Lett. **66**, 175 (1997)].
10. B. L. Altshuler and D. L. Maslov, Phys. Rev. Lett. **82**, 145 (1999).
11. É. G. Batyev, Pis'ma Zh. Éksp. Teor. Fiz. **72**, 727 (2000) [JETP Lett. **72**, 506 (2000)].
12. É. G. Batyev and L. S. Braginsky, Zh. Éksp. Teor. Fiz. **87**, 1361 (1984) [Sov. Phys. JETP **60**, 781 (1984)].
13. É. G. Batyev, Zh. Éksp. Teor. Fiz. **70**, 578 (1976) [Sov. Phys. JETP **43**, 300 (1976)].
14. A. M. Dyugaev, Zh. Éksp. Teor. Fiz. **70**, 2390 (1976) [Sov. Phys. JETP **43**, 1247 (1976)].
15. B. Spivak, cond-mat/0005328.

Translated by R. Tyapaev

JETP Letters, Vol. 73, No. 10, 2001, pp. 570–572. Translated from Pis'ma v Zhurnal Éksperimental'noĭ i Teoreticheskoĭ Fiziki, Vol. 73, No. 10, 2001, pp. 640–642.
Original Russian Text Copyright © 2001 by Kar'kin, Voronin, D'yachkova, Kadyrova, Tyutyunik, Zubkov, Zaĭnulin, Sadovskiĭ, Goshchitskiĭ.

Superconducting Properties of the Atomically Disordered MgB_2 Compound

A. E. Kar'kin[1,]*, V. I. Voronin[1], T. V. D'yachkova[2], N. I. Kadyrova[2], A. P. Tyutyunik[2], V. G. Zubkov[2], Yu. G. Zaĭnulin[2], M. V. Sadovskiĭ[3], and B. N. Goshchitskiĭ[1]

[1] *Institute of Metal Physics, Ural Division, Russian Academy of Sciences, ul. S. Kovalevskoĭ 18,*
Yekaterinburg, 620219 Russia
** e-mail: karkin@orar.zar.ru*
[2] *Institute of Solid-State Chemistry, Ural Division, Russian Academy of Sciences,*
ul. Pervomaĭskaya 91, Yekaterinburg, 620219 Russia
[3] *Institute of Electrophysics, Ural Division, Russian Academy of Sciences,*
ul. Komsomol'skaya 34, Yekaterinburg, 620216 Russia

Received April 23, 2001

The effect of disorder induced by neutron irradiation in a nuclear reactor (thermal neutron fluence 1×10^{19} cm^{-2}) on the superconducting transition temperature T_c and the upper critical field H_{c2} of polycrystalline MgB_2 samples was investigated. Despite the appreciable radiation-induced distortions (more than ten displacements per atom), the initial crystal structure (C32) was retained. The temperature T_c decreased from 38 to 5 K upon irradiation and was practically completely restored after the subsequent annealing at a temperature of 700°C. A weak change in the dH_{c2}/dT derivative upon irradiation is explained by the fact that the irradiated samples are described by the "pure" limit of the theory of disordered superconductors. The suppression of T_c upon disordering may be due to the isotropization of the originally anisotropic (or multicomponent) superconducting gap or to a decrease in the density of electronic states at the Fermi level. *© 2001 MAIK "Nauka/Interperiodica".*

PACS numbers: 74.25.-q; 74.72.-h

The discovery of superconductivity (SC) in binary MgB_2 compounds with $T_c \approx 40$ K [1] has raised the question of what the reason is for high T_c values and SC mechanism in such a simple system. Within the framework of electron–phonon superconductivity, the high T_c values are favored by high densities $N(E_F)$ of electronic states at the Fermi level and by soft phonon modes [2], although an exotic pairing mechanism may also take place in this particular case. The response of a system to a disorder induced by the irradiation with high-energy particles serves as a test for revealing the specific features of the SC state.

In metals (of the Nb type), the presence of several percent of impurity atoms or radiation-induced defects reduces T_c only slightly because of a small gap anisotropy. In the intermetallic compounds of the A15 type, a more substantial radiation-induced disorder may occur (suppression of long-range order and amorphization) because of considerable transformations in the electronic and phonon systems. In compounds with high $N(E_F)$ and T_c values (Nb_3Sn, V_3Si), the radiation-induced disordering lowers T_c (from 15–20 K to 1–3 K) because of a decrease in $N(E_F)$ [3]. In the compounds with low $N(E_F)$ and T_c (Mo_3Si and Mo_3Ge), the disordering increases T_c (from 1.5 to 7 K) because of an increase in $N(E_F)$ and softening of the phonon mode. This signifies that the individual features of electronic structure vanish upon the disordering, and the superconducting properties of the disordered compounds become similar to the properties of amorphous materials. At the same time, the effect of disorder on the SC of high-T_c superconductors radically differs from that observed in A15; the irradiation rapidly destroys SC ($T_c = 0$) [4].

In this work, we studied the superconducting properties of polycrystalline MgB_2 samples ($0.05 \times 1 \times 5$ mm) irradiated in the core of an IVV-2M nuclear reactor (thermal- and fast-neutron fluences $\Phi = 1 \times 10^{19}$ and 5×10^{18} cm^{-2}, respectively) or obtained after the subsequent isochronal annealing for 20 min at temperatures $T_{ann} = (200–700)$°C. MgB_2 powders were prepared by the method described in [5] and pressed under a pressure of 9 GPa at room temperature without the subsequent thermal treatments. According to X-ray powder diffraction analysis (CuK_α radiation), the samples contained traces (~3%) of MgO. This method of sample preparation gave a strained structure and was accompanied by the broadening of X-ray reflections and smearing of the superconducting transitions in the resistivity $\rho(T)$ and ac susceptibility $\chi(T)$ curves (Fig. 1), as well as by an increase in the resistivity $\rho(T)$ ($\rho \approx 0.4$ mΩ cm at $T = 300$ K). The latter fact implies that the intergrain boundaries make a considerable contribution to ρ(T), so that we will not analyze our data using the resistivity curves.

The structural distortions induced by the irradiation of B-containing materials by thermal neutrons are mainly due to the nuclear reaction at the ^{10}B isotope with emission of α particles and production of ^{7}Li. At $\Phi = 1 \times 10^{19}$ cm^{-2}, almost 1% of B atoms are splitted, which corresponds to a damaging dose of approximately more than 10 displacements per atom. Although there is a considerable absorption of thermal neutrons in the sample, one can expect that, due to multiple displacements of each atom, the radiation-induced defects are homogeneously distributed over the sample volume. In spite of the fact that the radiation-induced distortions of the material are very strong, the symmetry of the original structure (C32) is retained after the irradiation. The structural parameters refined by using the Rietveld analysis are given in the table. The irradiation resulted in the anisotropic expansion of the crystal lattice (the unit-cell volume increased by 1.4%), a faster increase in the c parameter, and a decrease in the occupancy N(Mg) of magnesium sites [N(B) = 1].

Figure 1 demonstrates the transformations of superconducting transition curves for the resistivity and susceptibility of the irradiated and annealed samples. The radiation reduces T_c down to ≈5 K, while the annealing at 700°C almost completely restores T_c. The transition width changes only slightly upon the irradiation, in compliance with the assumption about the homogeneous distribution of defects. The ρ(T) and χ(T) curves of the initial sample have a characteristic “two-step” shape, which is retained after the irradiation and the annealing below T_{ann} = 500°C (Fig. 1). It is likely that the low-temperature step is due to the presence of a strongly strained structure with lower T_c in the regions adjacent to the grain boundaries. For T_{ann} = (600–700)°C, this step smears, probably, due to the loss of Mg at the grain surfaces. The resistive transitions do not show any noticeable broadening in a magnetic field (Fig. 2). The temperature curves for the upper critical field H_{c2}, as determined from the half-transition temperatures (0.5 of the normal-state resistivity ρ_n), have almost identical slopes for the initial and irradiated samples (Fig. 3).

As was pointed out above, a considerable contribution to the resistivity of the samples studied comes from the intergrain boundaries; its true value for the MgB$_2$ grains is unknown. Experiments [6] with dense MgB$_2$ “wires” show that the mean free path l_{tr} in them is as high as 600 Å, whereas the coherence length ξ_0, as determined from the H_{c2} measurements, is on the order of 50 Å. For this reason, a weak change in the H_{c2}/dT derivative in our experiments can be explained by the fact that the irradiated samples remained in the region of a “pure” limit $l_{tr} > \xi_0$ (residual resistivity increased after the irradiation no more than eightfold). The theoretical calculation of dH_{c2}/dT in a simple model of a superconductor with anisotropic s pairing [7] indicates that the curve slope for the critical field changes only slightly in the whole region of transition from the

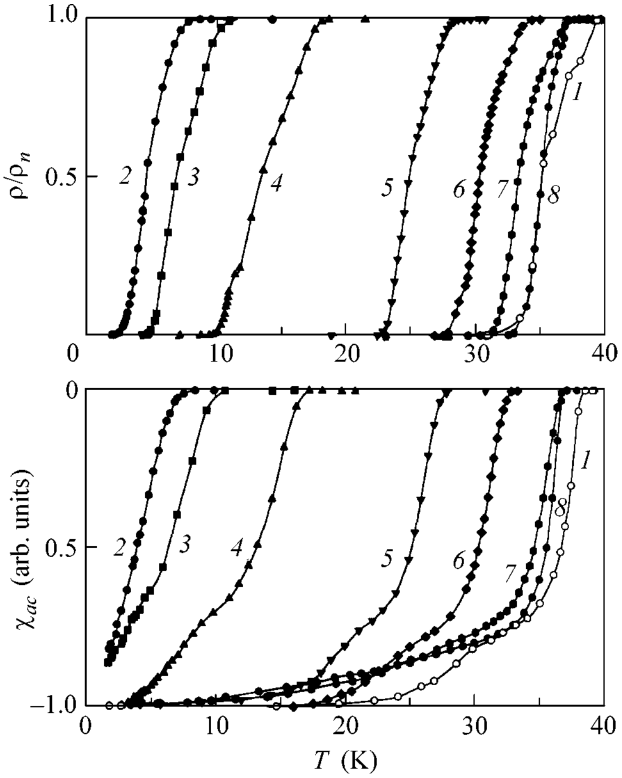

Fig. 1. Temperature dependences of the (up) reduced resistivity ρ/ρ$_n$ and (down) the ac susceptibility χ_{ac} of the (*1*) initial MgB$_2$ samples, (*2*) samples irradiated by the thermal-neutron fluence $\Phi = 1 \times 10^{19}$ cm^{-2}, and (*3–8*) samples annealed at T = 200, 300, 400, 500, 600, and 700°C, respectively. $\rho_n = \rho(T > T_c)$; $\chi_{ac} = -1$ corresponds to the complete screening of a sample by the superconducting currents.

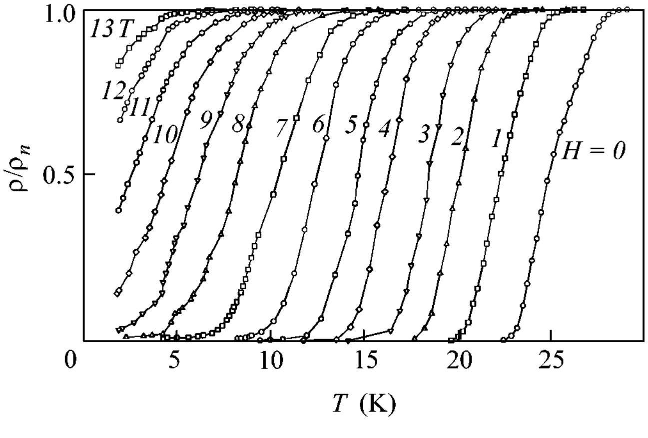

Fig. 2. Temperature dependences of ρ/ρ$_n$ for the MgB$_2$ samples irradiated and annealed at T = 400°C in magnetic fields denoted by numbers in units of T.

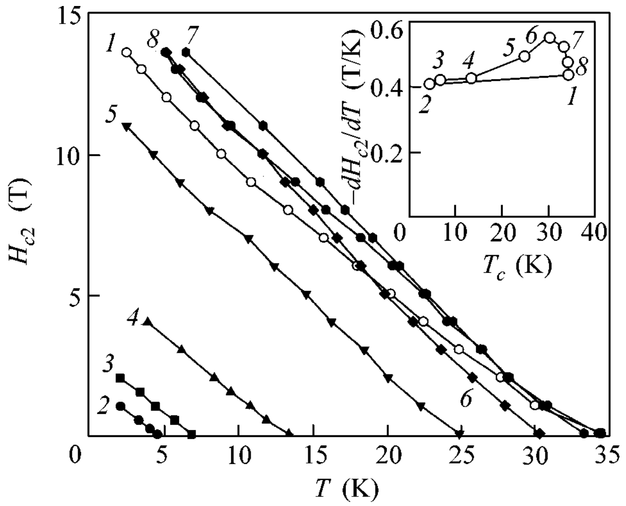

Fig. 3. Temperature dependences of the upper critical field H_{c2} for the initial, irradiated, and annealed MgB_2 samples. Inset: dependence of ($-dH_{c2}/dT$) on T_c. Notations are as in Fig. 1.

“pure” to the “dirty” limit. At the same time, the T_c temperature noticeably decreased in this region because of the isotropization of the energy gap. Note that the behavior of T_c observed in [7] is not universal and depends on the anisotropic model of the initial gap. In principle, T_c can strongly decrease depending on the parameters of the initial anisotropy.

The strong lowering of T_c, observed in this work, can be even more justifiably assigned to a decrease in the density $N(E_F)$ of electronic states at the Fermi level upon the disordering. In the dirty limit, $l_{tr} < \xi_0$, the slope of the H_{c2} curve starts to increase with a decrease in the mean free path [7]. This effect was practically unobserved in our experiment, which may be explained both by the fact that the dirty limit was not attained and by the fact that the corresponding increase is masked by the lowering of $N(E_F)$ upon the disordering. Independent indications that the anisotropic pairing or a closely related SC with different superconducting gaps at different Fermi surface sheets MgB_2 (multicomponent gap) is possible were provided by the measurements of specific heat [8] and the temperature dependence of penetration depth [9], as well as by the calculations in [10].

Lattice parameters a and c, unit-cell volume V, and occupancies N(Mg) of magnesium sites for the initial MgB_2 samples and the samples irradiated by neutron fluence $\Phi = 1 \times 10^{19}$ cm^{-2}

	Initial	Irradiated
a, Å	3.0878(2)	3.0953(3)
c, Å	3.5216(4)	3.5533(4)
V, Å^3	29.080(4)	29.482(5)
c/a	1.140	1.148
N(Mg)	0.96(4)	0.89(5)

This work was supported by state contracts of the Russian Federation [nos. 107-1(00)-P-D01 (contract no. 07/01), 107-19(00)-P-D01, and 108-31(00)-P-D01], the program of State Support of Leading Scientific Schools of the Russian Federation (project no. 00-15-96581), and the Russian Foundation for Basic Research (project no. 01-02-16877).

REFERENCES

1. J. Akimitsu, in *Symposium on Transition Metal Oxides, Sendai, 2001.*
2. W. L. McMillan, Phys. Rev. **167**, 331 (1968).
3. A. E. Karkin, A. V. Mirmelstein, V. E. Arkhipov, and B. N. Goshchitskii, Phys. Status Solidi A **61**, K117 (1980).
4. B. A. Aleksashin, I. F. Berger, S. V. Verkhovskii, *et al.*, Physica C (Amsterdam) **153–155**, 339 (1988).
5. A. Gerashenko, K. Mikhalev, V. Verkhovskii, *et al.*, cond-mat/0102421.
6. P. C. Canfield, D. K. Finnemore, S. L. Bud’ko, *et al.*, Phys. Rev. Lett. **86**, 1877 (2001); cond-mat/0102289.
7. A. I. Posazhennikova and M. V. Sadovskiĭ, Pis’ma Zh. Éksp. Teor. Fiz. **63**, 347 (1996) [JETP Lett. **63**, 358 (1996)].
8. Y. Wang, T. Plackowski, and A. Junod, cond-mat/010381.
9. C. Panagopoulos, B. D. Reinford, T. Xiang, *et al.*, cond-mat/0103060.
10. A. Y. Liu, I. I. Mazin, and J. Kortus, cond-mat/0103570.

Translated by V. Sakun

JETP Letters, Vol. 73, No. 10, 2001, pp. 573–578. Translated from Pis'ma v Zhurnal Éksperimental'noĭ i Teoreticheskoĭ Fiziki, Vol. 73, No. 10, 2001, pp. 643–648.
Original Russian Text Copyright © 2001 by Shul'man, Kotel'nikov, Varvanin, Mirgorodskaya.

Tunneling Spectroscopy of the Electron Exchange-Correlation Interaction in a Schottky Barrier in a Quantizing Magnetic Field: *n*-GaAs/Me Junctions

A. Ya. Shul'man[1,2,3], I. N. Kotel'nikov[1,2,3], N. A. Varvanin[1], and E. N. Mirgorodskaya[1]
[1] *Institute of Radio Engineering and Electronics, Russian Academy of Sciences, Moscow, 101999 Russia*
[2] *Grenoble High Magnetic Field Laboratory, CNRS, 38042 Grenoble Cedex 9, France*
[3] *International Laboratory of High Magnetic Fields and Low Temperatures, 53421 Wroclaw, Poland*
Received April 9, 2001

The magnetic-field-induced variation in the width of an anomalous resistance peak in the region of a zero-bias anomaly in *n*-GaAS/Me tunnel junctions was studied in the range of magnetic field strengths of up to 23 T at the temperatures $T = 4.2$ and 1.5 K. The experimental curves depend neither on the method of a semiconductor substrate surface preparation (doped single crystal cut or epitaxially grown doped semiconductor film) nor on the type of dopant (Te, Si) and metal (Me = Au, Al). A comparison to a theoretical dependence of the exchange potential on the magnetic field strength for electrons on the lowest Landau level confirms that the anomalous resistance peak width can serve as a measure of the exchange-correlation potential jump on the surface of the degenerate electron gas. The results provide an explanation for the dependence of the zero-bias anomaly on the magnetic field and offer a possibility for directly measuring the electron exchange-correlation interaction in a Schottky barrier by means of tunneling spectroscopy. © *2001 MAIK "Nauka/Interperiodica".*

PACS numbers: 73.30.+y; 71.10.Ca; 71.15.Mb

INTRODUCTION

The electron properties of various systems—from metals to many-electron molecules [1, 2]—are frequently calculated using the Hohenberg–Kohn–Sham density functional method for description of a spatially inhomogeneous nonideal electron gas. An important feature of this method is representation of the short-range electron interaction in terms of the exchange-correlation interaction potential v_{xc}. Difficulties encountered in the description of many-electron systems in cases when the electron–electron interaction is not weak inspire the development of particular theoretical models and v_{xc} approximations, the validity of which requires experimental verification. An object of this type is the plasma of free charge carriers in semiconductors, the parameters of which may vary in a broad range. As for the bulk properties, the exchange-correlation interaction leads to quantitative corrections rather than qualitative effects, being considerably masked by some other factors such as fluctuations of the impurity potential. The known bulk effects of the exchange-correlation interaction include the narrowing of the semiconductor bandgap with increasing free carrier concentration and the formation of electron–hole droplets [3].

In the transition region at the boundary of the degenerate electron gas, the electron density drops from the bulk level to zero. In this region, both the electron density profile $n(x)$ and the potential variation are determined by the electron exchange-correlation interaction. An analysis of the transition region in a Schottky barrier within the framework of the density functional method showed that, in a local approximation, $n(x)$ does not continuously fall to zero at the depleted layer boundary but exhibits a sharp drop upon reaching a certain universal critical value n_{cr} [4]. This discontinuity in $n(x)$ leads to a jump in the effective potential barrier shape in the vicinity of the Fermi level, which is manifested by a zero-bias anomaly (ZBA) in the calculated current–voltage characteristics of the semiconductor–metal tunnel junctions. The theoretical ZBA width on the bias axis is related to the exchange-correlation potential value at the critical electron density as $v_{xc}^{cr} = v_{xc}(n_{cr}) \approx -0.3\text{Ry}^*$. It was demonstrated that this estimate agrees with the available experimental data [4]. Consequences of this ZBA interpretation were experimentally verified for the *n*-GaAs/Au tunnel junctions [5].

The results of measurements in the presence of a quantizing magnetic field B parallel to the direction of current in the tunnel showed that this external field significantly affects both the tunnel resistance and the ZBA behavior [6]. An analysis of these data for the *n*-GaAs/Au tunnel junctions allowed a background potential in the region of ZBA to be determined and the separated resistance peak to be described in terms of the Lorentz distribution [7].

In this paper, we present the results of investigation of the Lorentzian width as a function of B for the *n*-GaAs/Au and *n*-GaAs/Al junctions for $B \leq 23$ T at the temperatures $T = 4.2$ and 1.5 K. The obtained experimental curve does not depend on the metal and is interpreted, based on the comparison with theoretical calculations, as a manifestation of the $v_{xc}^{cr}(B)$ variation under the Landau quantization conditions. Thus, we have demonstrated that a change in the ZBA peak width reflects the effect of a quantizing magnetic field on the electron exchange-correlation interaction at the degenerate electron gas surface and obtained direct experimental data on this effect. Application of tunneling spectroscopy to investigation of the shape of a nonideal electron gas surface presents additional interest in the context of a recently formulated concept of an Airy gas [8] related to the need in developing a special surface variant of the density functional method.

THEORY

Calculation of the critical electron density and the effective potential jump at the surface. According to the Kohn–Sham approach, the system of interacting electrons in an external potential field is replaced by a gas of noninteracting electrons occurring in the effective potential $\Phi_{\text{eff}}(x) = \Phi(x) + v_{xc}$, where $\Phi(x) = -ev$ is the potential energy of an electron in a self-consistent Coulomb potential v; $v_{xc}(x) = v_{xc}[n(x)]$ in the local density approximation. It can be shown that, if the electron gas in a volume is slightly nonideal, so that $r_s = (3/4\pi n a_*^3)^{1/3} < 1$ (where a_* is the Bohr radius for electrons in the semiconductor), the Schottky barrier always satisfies the quasi-classical conditions under which the barrier shape is determined by two relationships. The first is a relationship between the local electron density and the effective potential, which is obtained from the Kohn–Sham equations for one-particle wavefunctions in the quasi-classical approximation upon averaging the electron density on a scale greater than the Fermi wavelength. The second is the Poisson equation for the Coulomb potential created by ionized donors with the density N_D and by the electron distribution

$$n(x) = n[\Phi_{\text{eff}}(x)], \tag{1}$$

$$\frac{d^2\Phi}{dx^2} = \frac{4\pi e^2}{\kappa}(N_D - n(\Phi(x))), \tag{2}$$

where κ is the dielectric constant of the lattice.

In the absence of a magnetic field, this system was studied in [4] with neglect of the nonparabolic shape of the conduction band. The function $n(\Phi)$ in the right-hand part of Eq. (2) was determined by solving the equation

$$n(x) = N_D[(\mu_F - \Phi(x) - v_{xc}(n(x)))/\mu_0]^{3/2}, \tag{3}$$

where $\mu_0 = \hbar k_F^2/2m$, $k_F = (3\pi^2 N_D)^{1/3}$, and μ_F is the Fermi energy of electrons in the semiconductor bulk determined by the same equation with $n(x) = N_D$ and $\Phi = 0$. An analysis of the solution to Eq. (3) with an allowance for the exchange-correlation interaction showed that, on the passage from semiconductor bulk to surface with Φ increasing from zero, the electron density decreases from the bulk value to a certain finite level. As the Φ value grows further, the solution loses physical sense. A condition for this finite minimum electron density $n_{cr} = n(\Phi_{cr})$, which can be obtained from the relationship $dn/d\Phi|_{\Phi \to \Phi_{cr}} \longrightarrow -\infty$, indicates that the further increase in Φ (and the corresponding decrease in n according to the solution obtained) makes the spatially homogeneous electron distribution unstable with respect to shortwave density perturbations. This conclusion can be readily derived from Eq. (2) by writing the corresponding dispersion equation for small perturbations and taking into account a change in the sign of $dn/d\Phi$ on the infinity transition. The break in the electron density on a finite level at the degenerate electron plasma boundary corresponds to a condition determining the radius of a many-electron atom in the Thomas–Fermi–Dirac approximation (cf. to Eq. (2.21) in [9] and to the remark on p. 79 in review [10]). Since Eq. (3) corresponds to the longwave approximation obtained by averaging over a scale on the order of $1/k_F$, the fact of $dn/d\Phi$ turning infinite should be considered as indicative of the appearance of a short-range order in the "electron fluid" (see a more detailed consideration in [11]).

It is more convenient to present a solution to Eq. (3) in the form of the inverse function $\Phi(n)$. Then, the critical density condition takes the form $d\Phi/dn|_{n_{cr}} = 0$. According to [4], a solution to this equation using the Wigner expression for the correlation energy yields a critical electron density corresponding to $r_s^{cr} = 5.42$ and $v_{xc}^{cr} = -0.3\text{Ry}^*$. Taken with the inverse sign, the latter value is a measure of the effective potential jump in the Schottky barrier. The jump is related to the v_{xc} vanishing on the passage from the region where $n \le n_{cr}$ to a depleted layer with $n(x) \equiv 0$. On leaving only the exchange energy in the above relationships, we obtain the following critical values of the density and potential: $r_s^{cr} = 6.03$ and $v_x^{cr} = -0.2\text{Ry}^*$. These values bound the possible potential jumps in the approximation considered. In the case of n-GaAs, where the effective Rydberg is $\text{Ry}^* = 6$ meV, the jump estimates fall between 1.2 and 1.8 meV.

Figure 1 shows the calculated variation of the effective potential Φ_{eff} in the Schottky barrier near the Fermi level μ_s of a semiconductor in comparison with the experimentally measured plot of the differential resistance $R_d = dV/dI$ versus V in the ZBA region. In order to more clearly reveal the similar and distinctive features, the curve of $\Phi_{\text{eff}}(x)$ is plotted in the $(\mu - \Phi_t, x_t - x_{cr})$ coordinates, where x_t is the coordinate of the turning point of electrons tunneling at an energy corresponding to the Fermi energy in the metal $\mu_m = \mu - eV$; here V is the bias voltage across the junction, which is positive ($V > 0$) for the electron tunneling from semiconductor into metal. Accordingly, $\Phi_t = \Phi_{\text{eff}}(x_t)$ and x_{cr} is the coordinate of the potential jump for $V = 0$. Note that a shift of the turning point in the bias range studied is on the order of thousandth fractions of the effective Bohr radius. This circumstance gives us hope that a difference in the shape of barriers calculated using various expressions for the correlation energy will be sufficient to select the most adequate model by comparison with the tunneling spectroscopy data.

There is an evident correlation between a change in the $R_d(V)$ slope and the electron turning point variation on the passage from negative to positive bias. The turning point behavior determines the rate of variation of the Schottky barrier width with increasing bias for the states accounting for the major contribution to resistance at small biases. The tunnel current–voltage characteristics calculated within the framework of this model provides both qualitative and quantitative agreement with experiment [4, 5] outside the peak region (Fig. 1). It must be emphasized that no sharp variation in the Coulomb potential in this region can be obtained without allowance for the exchange-correlation interaction; therefore, this interaction accounts for a change in $R_d(V)$ slope as well.

The resistance peak in the vicinity of $V = 0$ can be explained by additional (relative to the wavefunction decay under the barrier) contribution to the tunnel resistance due to the electron reflection from the quasi-classical potential discontinuity. The magnitude of this contribution on the V scale is related to the potential jump, which allows us to study the effect of various factors on the exchange-correlation interaction on the electron gas surface by the method of tunneling spectroscopy.

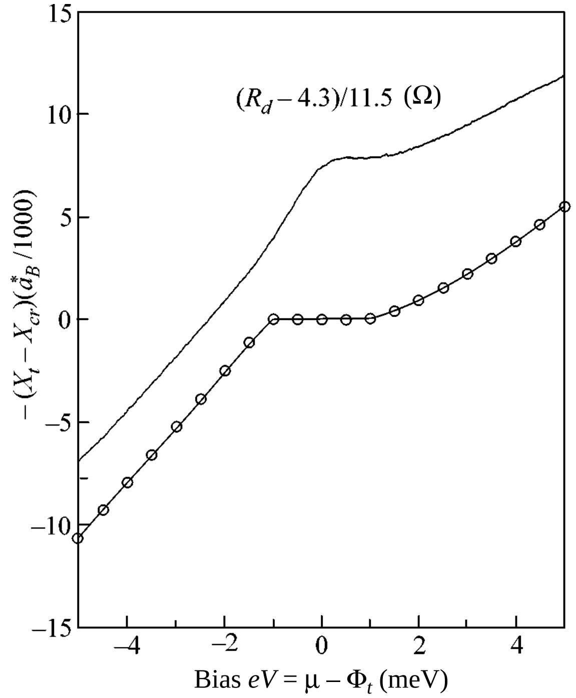

Fig. 1. Calculated effective potential barrier shape (bottom curve) in comparison with the experimental data on the differential resistance $R_d(V)$ (top curve) in the anomalous region (sample no. 1, $T = 1.5$ K, $B = 0$). For a clearer comparison of the barrier shape and the $R_d(V)$ curve, the $\Phi_{\text{eff}}(x)$ profile was converted into coordinate dependence of the turning point for electrons with the energy $\mu - eV$ according to Eq. (7). The upper curve is obtained from the measured $R_d(V)$ by a linear scale transformation indicated in the figure. Important features of the barrier are both the effective potential jump and a sharp change in the potential below and above the Fermi level; the latter difference also contributes to the anomalous behavior by determining a difference in slopes of the $R_d(V)$ curve below and above the point of $V = 0$.

In the presence of a quantizing magnetic field ($\hbar\omega_B \gg T$, where ω_B is the cyclotron frequency) normal to the semiconductor–metal interface, the main contribution to the tunnel current is due to the states at the lowest Landau level ($N = 0$). For the states with $N > 0$, the effective barrier increases in both width and height. Because of a small value of the effective Lande factor for electrons in GaAs ($g^* = -0.44$ [12]), we may neglect the spin splitting of this level in a part of the region of the magnetic fields and temperatures studied. For the maximum B values employed, the spin splitting becomes greater than T. However, the theory predicted equal values of the potential jump in both limiting cases. Upon conducting calculations for the lowest spin-nondegenerate level ($N = 0$, $\uparrow$) similar to those described above but employing the formulas for the electron exchange energy at $N = 0$ taken from [9], the condition $d\Phi/dn|_{n_{cr}} = 0$ yields an equation for the critical electron density,

$$n_{\uparrow cr}(B) = \frac{n_B}{2^{3/2}\pi}\left(\frac{L_B}{a_*}\right)F_{00}(2n_{\uparrow cr}/n_B), \tag{4}$$

and an expression for the corresponding exchange potential

$$v_{\uparrow x}^{cr}(B) = -\hbar\omega_B \frac{1}{2^{3/2}\pi}\frac{L_B}{a_*}F_{00}^1(2n_{\uparrow cr}(B)/n_B), \tag{5}$$

where $L_B^2 = \hbar c/eB$, $n_B = 1/\sqrt{2}\pi^2 L_B^3$, and

$$F_{00}(x) = \int_0^\infty \frac{dx\exp(-t)}{x^2 + t}; \quad F_{00}^1(x) = \int_0^x dt F_{00}(t).$$

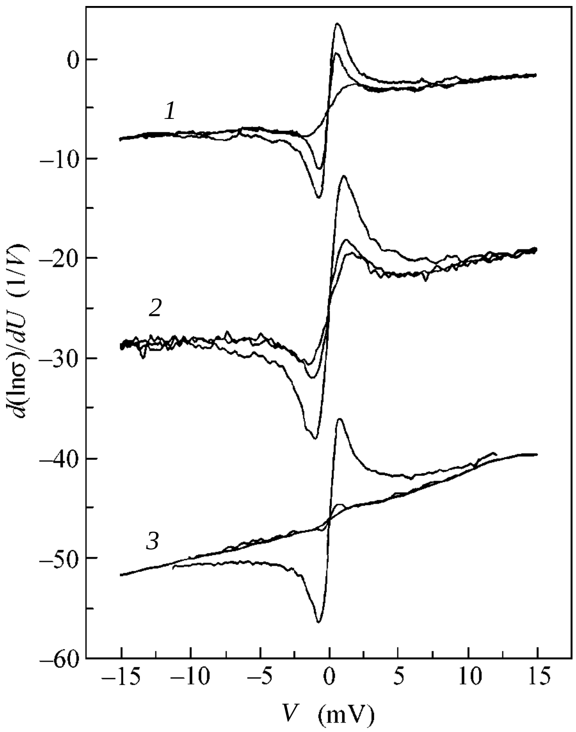

Fig. 2. Electron tunneling spectra of three junctions measured at two different temperature in the presence and absence of the applied magnetic field. The ZBA amplitude increases with the process parameters in the following order $\{T\,[\mathrm{K}]; B\,[\mathrm{T}]\}$: {4.2; 0}, {1.5; 0}, {1.5; 14}. Curve numbers correspond to the sample numbers in the table. Curves *2* and *3* are shifted arbitrarily along the ordinate axis.

In the case of spin degeneracy, the two sublevels are equally occupied and $n_{cr} = 2n_{\uparrow cr}$. A condition for which the measured anomalous peak width can be compared to formula (5) is that $\hbar\omega_B > v_{xc}^{cr}$ for $B = 0$.

EXPERIMENT

Measurement of the anomalous resistance peak in a quantizing magnetic field. In the absence of a magnetic field, the junctions exhibit certain variations in the degree of manifestation and shape of ZBA, as can be seen by comparing the curves in Fig. 2. However, the ZBA magnitude on the bias scale and its magnetic-field-induced variations in all cases were the same. This fact allows the magnetic field action to be considered as the effect of magnetic quantization on electrons in the Schottky barrier. Data on the characteristics of junctions studied in this respect are summarized in the table indicating significant stages in the technology, electrode material, and the impurity charge density (determined from the tunnel current–voltage curves as described in [13, 14]). For the samples nos. 1 and 2, prepared using substrates cut from a doped single-crystalline ingot, the data were also confirmed by the results of measurements of the bulk electron concentration using the Shubnikov–de Haas magnetoresistance oscillations.

The way of presentation of the tunneling spectra in terms of a logarithmic derivative of the differential conductivity $\sigma(V) = dI/dV$ is convenient for both measurement and interpretation purposes. The advantages of a logarithmic derivative from the standpoint of physical meaning are readily seen from the expression for the tunnel current and from the fact that we are studying the zero-bias region. Without going into detail, we can elucidate the main idea by writing a simplified schematic expression for the tunnel current (for detail, see [13, 14]):

$$I(V) \propto -e\int_0^\infty dE[f(E) - f(E+eV)]\tilde{D}(E, V), \qquad (6)$$

where E is the total electron energy in a semiconductor, $f(E)$ is the Fermi distribution function, $\tilde{D}(E, V)$ is the effective transparency of the Schottky barrier for electrons with the energy E averaged over the states with admissible momenta along the semiconductor–metal interface, e is the elementary charge, and V is the bias voltage (positive for the free carriers passing from semiconductor to metal). All energies are measured from the conduction band bottom of the semiconductor.

Parameters of semiconductor–metal junctions

Sample no.	Junction	Technology	Metal	N_e, 10^{18} cm^{-3}
1	s312	Single crystal + UHVD[1)]	Au	5.8
2	s311	Single crystal + UHVD[1)]	Au	5.8
3	s7d21	MBE + UHVD[2)]	Au	3.0
4	s7a11	MBE[3)]	Al	3.1
5	s8a11	MBE[3)]	Al	2.9

[1)] Substrates cut from a single-crystalline Te-doped GaAs obtained by zone melting. Metal (Au) film was deposited in ultrahigh vacuum (UHVD) after thermal annealing, with the sample surface cleanness monitored by Auger electron spectroscopy [13, 14].

[2)] Substrates prepared by molecular-beam epitaxy (MBE). Metal (Au) deposited as above.

[3)] Substrates prepared by MBE of 1.5-μm-thick Si-doped GaAs layers. Metal (Al) deposited in the same chamber immediately after termination of MBE process.

Substituting Eq. (6) into the definition of σ and setting $T = 0$, we obtain

$$\sigma(V) \equiv \frac{dI}{dV} \propto \tilde{D}(\mu - eV, V) + \operatorname{sgn}(V)\int_{\mu - eV}^{\mu} dE\frac{\partial \tilde{D}(E, V)}{\partial V}. \tag{7}$$

As is seen, the conductivity of the junction for $V = 0$ is proportional to the barrier transparency at the Fermi level. Since the contribution of the integral term can be ignored in a small vicinity of $V = 0$, the measurements of $\sigma(V)$ in this region give the values of the barrier transparency for electrons with the energy corresponding to the Fermi level in the metal. For $V > 0$, we can evaluate the transparency for the states below the Fermi level and vice versa for $V < 0$.

An important problem in the experimental study of ZBAs is to eliminate the ambiguity in determining the $\sigma(V)$ background relative to which the “anomalous behavior” is measured (for details, see, e.g., a discussion in [15]). In our case, this was achieved using the fact [6] that the logarithmic derivative of $\sigma(V)$ is independent of the magnetic field outside the bias regions where the many-body features in the tunneling spectra are manifested.

RESULTS AND DISCUSSION

The peak obtained upon the background subtraction is well described in terms of the Lorentz distribution [7] at $T = 4.2$ K. However, the peak shape at $T = 1.5$ K is indicative of the possible deviations from this law. In order to make the data independent of the model peak shape selection and in view of the absence of a theoretical description of the current–voltage characteristics inside the ZBA region, we determined the peak width as the full width at half maximum (WFHM) versus the magnetic field strength. The results of this treatment are presented in Fig. 3 together with the theoretical curves describing dependence of the exchange energy, calculated at a critical electron density by formula (5), on the magnetic field strength. For more convenient comparison, the theoretical values were multiplied by the factors indicated in the caption to Fig. 3. As is seen, the experimentally observed field-induced variation of the peak agrees with the theoretical dependence of the exchange energy on the magnetic field strength.

A difference in the absolute values is related to the thermal broadening. As is known, the temperature blurring of the Fermi distribution in Eq. (6) leads to broadening of the spectral lines of inelastic tunneling related to the molecular vibrations of impurities in the barriers. This broadening is estimated at about 5.5 T (see, e.g., [16, ch. 10]). The ratio of the peak widths measured at 4.2 and 1.5 K is smaller than the temperature ratio, which is indicative of a decrease in the temperature dependence. However, the observed twofold difference between the peak width measured at 1.5 K and the theoretical value is too large to be attributed to neglect of the correlation energy in the latter case: a contribution of the correlation energy to the surface properties of a degenerate electron gas usually does not exceed 30% (see, e.g., [17, section 2.4]).

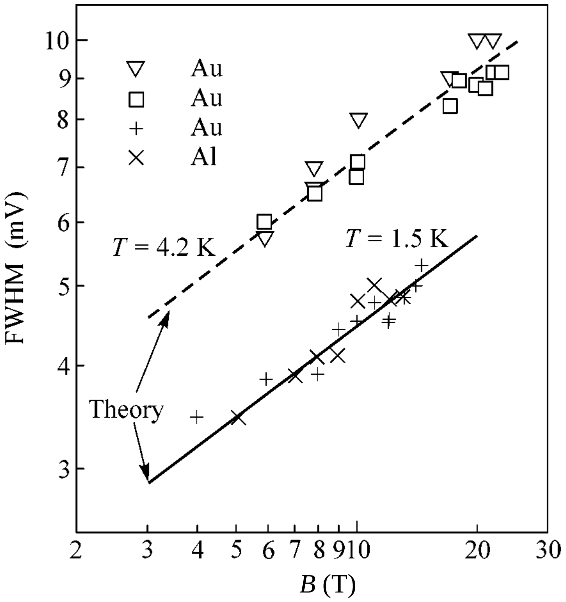

Fig. 3. Plots of the experimental anomalous resistance peak width versus magnetic field strength at two temperatures. Despite a difference in the absolute values, the course of variation is the same and agrees to within a constant factor with the theoretical calculation of the electron exchange energy at the boundary of the Fermi gas in a quantizing magnetic field at $T = 0$. For matching with the experimental points at $T = 1.5$ and 4.2 K, the theoretical values were multiplied by 2.2 and 3.5, respectively.

CONCLUSION

The results of our investigation allow tunneling spectroscopy in the region of zero-bias anomaly of semiconductor–metal junctions to be considered as a possible means of studying the electron interactions at the degenerate plasma surface.

It should be noted that ZBAs analogous to those at the semiconductor–metal junctions with the Schottky barrier are observed in some other tunnel structures with a free-carrier plasma region boundary formed at the intersection of a self-consistent potential barrier and the Fermi level. Such systems include tunnel *p*–*n* diodes (numerous examples can be found in [18]), tunnel junctions with Schottky barriers based on semiconductors of the *p* type [15], and tunnel structures formed in semiconductors by heterojunctions with extended spacers [19]. Recently, an analogous zero-bias anomaly was observed in the tunneling spectrum of a junction with the Schottky barrier formed by a two-dimensional electron gas in delta-doped GaAs [20].

The authors are grateful to I.M. Kotelyanskiĭ, V.G. Mokerov, Yu.V. Fedorov, A.V. Hook, A.L. Musatov, K. Izraélyants, V.P. Koshelets, and S.A. Kovtanyuk for their technical assistance and sample preparation. Special thanks to Prof. J.-C. Portal and Dr. D. Maude (Grenoble HMF Laboratory) and to Prof. V.I. Nizankovsky (International Laboratory of High Magnetic Fields and Low Temperatures, Wroclaw) are acknowledge for their fruitful cooperation and help in the experimental arrangements during visits to these research centers.

The work was supported by the Russian Foundation for Basic Research and by INTAS (grant no. 97-11475).

REFERENCES

1. *Theory of the Inhomogeneous Electron Gas*, Ed. by S. Lundquist and N. H. March (Plenum, New York, 1983; Mir, Moscow, 1987).
2. W. Kohn, Rev. Mod. Phys. **71**, 1253 (1999).
3. *Electron-Hole Droplets in Semiconductors*, Ed. by C. D. Jeffries and L. V. Keldysh (North-Holland, Amsterdam, 1983; Nauka, Moscow, 1988).
4. A. Ya. Shul’man and V. V. Zaĭtsev, Solid State Commun. **18**, 1623 (1976).
5. I. N. Kotel’nikov and A. Ya. Shul’man, in *Proceedings of the 19th International Conference on Physics of Semiconductors, 1988*, Vol. 1, p. 681.
6. I. N. Kotel’nikov, A. Ya. Shul’man, D. K. Maude, *et al.*, Pis’ma Zh. Éksp. Teor. Fiz. **60**, 849 (1994) [JETP Lett. **60**, 863 (1994)].
7. A. Ya. Shul’man and I. N. Kotel’nikov, in *Proceedings of the 12th International Conference on High Magnetic Fields in Physics of Semiconductors*, Ed. by G. Landwehr and W. Ossau (World Scientific, Singapore, 1997), Vol. 1, p. 461.
8. W. Kohn and A. E. Mattsson, Phys. Rev. Lett. **81**, 3487 (1998).
9. I. Fushiki, E. H. Gudmundsson, C. J. Pethick, *et al.*, Ann. Phys. (N.Y.) **216**, 29 (1992).
10. M. B. Partenskiĭ, Usp. Fiz. Nauk **128**, 69 (1979) [Sov. Phys. Usp. **22**, 330 (1979)].
11. I. N. Kotel’nikov and A. Ya. Shul’man, Pis’ma Zh. Éksp. Teor. Fiz. **15**, 529 (1972) [JETP Lett. **15**, 374 (1972)].
12. C. Weisbuch and C. Hermann, in *Optical Orientation*, Ed. by F. Meier and B. P. Zakharchenya (North-Holland, Amsterdam, 1984; Nauka, Leningrad, 1989).
13. I. N. Kotel’nikov, I. L. Beĭnikhes, and A. Ya. Shul’man, Fiz. Tverd. Tela (Leningrad) **27**, 401 (1985) [Sov. Phys. Solid State **27**, 246 (1985)].
14. E. M. Dizhur, A. Ya. Shul’man, I. N. Kotel’nikov, and A. N. Voronovsky, Phys. Status Solidi B **223** (1), 129 (2001).
15. T. Carruthers, Phys. Rev. B **10**, 3356 (1974).
16. E. L. Wolf, *Principles of Electron Tunneling Spectroscopy* (Oxford Univ. Press, Oxford, 1985; Naukova Dumka, Kiev, 1990).
17. W. Kohn and P. Vashishta, in *Theory of the Inhomogeneous Electron Gas*, Ed. by S. Lundquist and N. H. March (Plenum, New York, 1983; Mir, Moscow, 1987), Chap. 2.
18. R. A. Logan, in *Tunneling Phenomena in Solids*, Ed. by E. Burstein and S. Lundqvist (Plenum, New York, 1969; Mir, Moscow, 1973), Chap. 11.
19. Yu. V. Dubrovskiĭ, Yu. N. Khanin, T. G. Andersson, *et al.*, Zh. Éksp. Teor. Fiz. **109**, 868 (1996) [JETP **82**, 467 (1996)].
20. I. N. Kotel’nikov, V. A. Kokin, Yu. V. Fedorov, *et al.*, Pis’ma Zh. Éksp. Teor. Fiz. **71**, 564 (2000) [JETP Lett. **71**, 387 (2000)].

Translated by P. Pozdeev